# Ultrafast hot carrier relaxation and charge transfer in nanoparticle assemblies and nanoconjugates

Submitted in partial fulfillment of the requirements

of the degree of

Doctor of Philosophy

of the
Indian Institute of Technology Bombay, India
and
Monash University, Australia

by

**Bala Gopal Maddala**

Supervisors:

Prof. Anindya Datta (IIT Bombay)

Prof. Alison Funston (Monash University)

*The course of study for this award was developed jointly by*
*Monash University, Australia and the Indian Institute of Technology Bombay, India*
*and was given academic recognition by each of them.*
*The programme was administrated by The IITB-Monash Research Academy*

(Year 2021)

## Thesis approval sheet

This thesis entitled "Ultrafast hot carrier relaxation and charge transfer in nanoparticle assemblies and nanoconjugates" by Bala Gopal Maddala is approved for the degree of Doctor of Philosophy.

Examiners

---

---

Supervisor

---

Chairman

---

Date ……

Place …….

**Declaration of Honesty and Integrity**

I, Bala Gopal Maddala, declare that this written submission represents my ideas in my own words and where others' ideas or words have been included, I have adequately cited and referenced the original sources. I also declare that I have adhered to all principles of academic honesty and integrity and have not misrepresented or fabricated or falsified any idea/data/fact/source in my submission. I understand that any violation of the above will be cause for disciplinary action by the Institute and can also evoke penal action from the sources which have thus not been properly cited or from whom proper permission has not been taken when needed.

_____

Bala Gopal Maddala

(154034002)

Date: 17-03-2021

# Dedicated to My Family

# Acknowledgements

I would like to take this opportunity to thank all the people who are involved with me during my journey of PhD at IIT Bombay and Monash university. I thank the supreme source of energy for giving me this wonderful learning experience through many challenges.

Firstly, I thank my supervisors Prof. Anindya Datta and Prof. Alison Funston for their constant support and intellectual guidance through this journey. Many interactions with them has shaped up my growth as a researcher and individual. I thank my research progress committee members Prof. Arindam Chowdhury, Prof. Patrick Perlmutter, Prof. Boon Mian Tian and Prof. David Turner for their suggestions and comments.

I am very blessed to have Prof. Anindya Datta as my supervisor during these years. During this journey I have learned not only how to conduct scientific research but also about leadership and life from him. He has been a great support system for me, his quick decision making and helping nature even beyond his comfort zone has made my journey easier. He is someone you can always bank upon in challenging times. He always made sure that he is approachable and made sure that I get all the resources I need for my research. His positive attitude, encouragement and constant support to all the students he is associated with is something I look up to and admire. In addition, I have learned a lot about teaching in a simple yet clear and effective manner from him. I wish I could imbibe these qualities from him.

I express my deep regards to Prof. Alison Funston for her valuable guidance in scientific endeavors. She is full of encouraging words which gave me confidence and positive impact in the work I was doing. I am immensely thankful for her contribution and guidance over the years.

I thank Prof. Siva Subramaniam Iyer for allowing me to work in his lab for the transient absorption experiments. Without him, it would not be possible to finish my work in time.

A lot of people have helped me during my PhD journey. I am very much indebted to Anchal Yadav for providing me the nanomaterial samples to work with. Without her, it would not have been possible to finish my thesis in time. I also thank Kanika Jain for providing me the porphyrin samples she synthesized. I thank Avinash, Tuhin, Sucheta, Soumyadipta, Hemen,

Sharmistha, Souradip, Fariyad, Tanuja, Rituparna, Prajit. Thanks are due to all my cheerful and helpful lab mates. I learned a lot from each of them. They played an important role from performing experiments, scientific and non-scientific discussions and made the challenging time in lab a memorable and enjoyable stay which I would cherish for lifetime. I also thank my lab mates Laurent, Simon, Ali, Ari, Anchal, Anum for their support during my stay at Monash university.

I thank my constant companions Abhishek and Laxman during my PhD. They are a great support system I had. We had a wonderful time together during our stay. They are the key motivators for me during challenging times of research and personal issues. I also thank Fariyad, Hemen and Souradip who listened to me and gave constructive advice during minor setbacks.

I gratefully acknowledge IITB-Monash Academy, IRCC, NCPRE for the research grants and fellowship.

I finally thank my parents, family for their support in my each and every decision. I thank my wife Mounika for her support and understanding of my work life and motivating me.

--- Bala Gopal Maddala

# Abstract

Quest for the alternative energy sources as compared to fossil fuels is on the rise. Currently, photovoltaics is considered as one of the alternatives which are dominated by crystalline silicon. There are many low-cost solar cell materials such as metal-semiconductor nano heterostructures, metal nanoparticle assemblies, and organic dye molecules which could compete with fossil fuels and crystalline silicon. Understanding the excited state dynamics of these materials is necessary to create cost-effective devices. This thesis examines the ultrafast excited-state dynamics in gold nanoparticle assemblies, Titanium dioxide nanorod-phenothiazine porphyrin systems, Copper Zinc Tin Sulphide-gold (CZTS-Au), and Lead sulfide-gold (PbS-Au) nano heterostructures using transient absorption spectroscopy (pump-probe spectroscopy).

The first section of the thesis we report hot electron relaxation dynamics in GNP dimers and trimers, prepared by self-assembly using a dithiol linker. Global analysis of femtosecond transient absorption kinetic data of these systems shows that their hot electron relaxation, through electron-phonon and phonon-phonon coupling, is faster than that of monomers in solution phase. This is attributed to greater extent of overlap of electron oscillation and phonon spectra in the region of enhanced electric field intensity. Control over the tunability of hot electron relaxation dynamics in these assemblies of gold nanoparticles bears promise in development of their potential applications as commercial and cost efficient saturable absorbers in optical switches for compact lasers and other optical devices.

Further, we studied electron transfer dynamics in cubic shaped PbS-Au heterostructures using transient absorption spectroscopy. We analyzed the electron transfer rates and charge

relaxation dynamics from $1S_e$ and $1P_e$ states of conduction band from excited state absorption dynamics experiments from pump probe data. Ultrafast charge separation at the junction of the metal-semiconductor interface before Auger recombination and other relaxation channels is observed which is very crucial for the development of solar cells where multiple charge carriers created from the MEG can be extracted efficiently leading to overcome Shockley-Queisser limit.

Next, we studied ultrafast charge relaxation dynamics in CZTS-Au nano heterostructures at different pump fluence energies. Pump probe data of the transient absorption spectroscopy shows photoinduced absorption in the entire probe region suggests the domination of excited state absorption over ground state bleach. Transient absorption spectra in CZTS-Au nanostructures resulted in reduction of the optical density of the ESA suggesting an ultrafast charge transfer faster than the hot electron trapping process and within the instrument response function (200 fs). This ultrafast charge transfer process faster than the trapping process is crucial in optimizing the CZTS based nanostructures in photovoltaic applications.

Finally, we have designed a $A_3B$ porphyrin sensitizer in which the three meso-positions were decorated with three phenothiazine moieties tethered to porphyrin core, and the other meso-position is functionalized with phenyl carboxylic acid which can play a dual role as acceptor and anchoring group. A series of phenothiazine-porphyrin systems in which phenothiazine tethered to porphyrin with different linkages such as phenyl, alkynyl, and phenoxyl alkyl linkages and carboxylic acid anchoring group to attach to the semiconductor nanoparticles such as $TiO_2$ and the efficiency of photo-induced electron transfer and the solar energy conversion to electricity w.r.t. linker sizes were investigated. Efficient charge separation before the charge recombination and other undesired pathways is evident in the studied phenothiazine porphyrin dye in the presence of semiconductor $TiO_2$ nanorods. In addition, tunability of electron

injection and back electron transfer rates is observed with different spacers between porphyrin and phenothiazine moieties.

## Table of Contents

# List of Figures

# 1 Introduction

Ultrafast charge carrier relaxation dynamics in noble metal nanoparticles and quantum dots have been of immense interest to material scientists around the world due to their wide range of applications. A wide range of phenomena are being studied in these systems, from shape dependence of the nanoparticles on the ultrafast carrier dynamics to the application of semiconductor quantum dots for efficient solar energy harvesting. While surface plasmon resonance of various metal nanoparticles and exciton dynamics in quantum dots are well studied, considerable interest has been generated to study the ultrafast dynamics in controlled metal nanoparticle assemblies and metal-semiconductor heterostructures. In the present thesis we try to focus on understanding of hot electron relaxation dynamics in these systems. Before going into discussing the results, it is important to understand the background required for such analysis. The rest of the chapter gives a brief overview of underlying principles in metal and semiconductor nanoparticles.

## 1.1 Metal Nanoparticles

Materials in the nanometer size regime acquire interesting properties when compared to the bulk. By definition, the size of nanomaterials range from 1-100 nm. Enhancements in optical, thermal and mechanical properties are observed for metallic nanoparticles compared to their bulk counterparts. These unique properties are the result of the confinement of electrons within the nanomaterial under these very small size regimes.[1] The intense colour and their ability to tune the properties of the particles comes from the phenomenon called surface plasmon resonance.[2]

The unique optical properties of metal nanoparticles such as gold (Au), silver (Ag), copper (Cu) are due to the localized surface plasmon resonance (LSPR). The electrons in the half filled s-subshell are responsible for this. These free electrons in the conduction band known as free electron gas interact with incident electromagnetic radiation. The oscillating electric field of the radiation induces the free electrons to move in phase with the phase of the electromagnetic excitation. The electric field displaces the negatively charged electrons away from the nucleus which creates a dipole inside the nanoparticle. This dipole creates an electric field that opposes the incoming field thus creating a restoring force. The stronger the displacement of electrons from the nucleus the stronger will be the restoring force. Coulombic restoring force between nucleus and the electron cloud causes the free electrons to oscillate relative to the gold nuclei which is associated with a natural frequency. When this natural frequency matches with the frequency of the incoming electromagnetic radiation, the corresponding energy of the radiation is absorbed giving rise to a surface plasmon absorption. This effect which is localized at the surface of the particles is termed as the localized surface plasmon resonance, the LSPR ( Figure 1.1).[3]

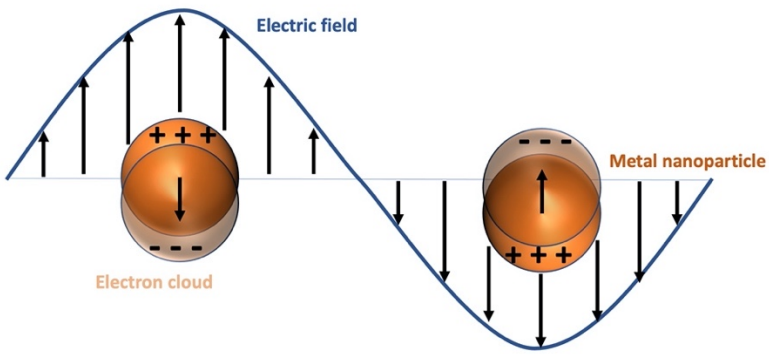


Figure 1.1. Schematic of surface plasmon resonance in metal nanoparticle.

The optical response of the metal nanoparticles depends on the extinction coefficient of these systems. For example if the particle absorbs half of the incident photons then its absorption

cross-section is half of its geometrical cross section. Similarly, some photons incident on particle gets scattered in different directions, this gives the scattering cross section. Overall the extinction coefficient depends on sum of the absorption and scattering cross section of the particles and describes the total number of photons absorbed and scattered out of all the incident photons by the particle. As the size of the particle increases the optical cross section and scattering component increases and results in broadening of the plasmon peak and shift towards longer wavelength (known as a "red shift").[3] In addition to the surface plasmon excitation there are interband transitions in metal nanoparticles. Metals have a continuous density of states formed by mixing of valence and conduction band. Apart from these there are some inner level bands that did not split enough to overlap with continuous bands, transition from these inner bands to conduction band results in absorption edge in the blue region of the spectrum similar to what's observed in quantum dots.[4] These interband relaxation results in feeble fluorescence in metal nanoparticles.[5] This fluorescence is not observed as efficiently in bulk but when the particle size decreases to very few atoms per particle, energy bands are not formed very well and interband transitions become prominent. `For gold nanoparticles, there is a overlap of surface plasmon band and interband transition, whereas for silver nanoparticles they are well separated. This leads to a broad surface plasmon band in gold NPs as compared to much narrower spectrum observed in silver NPs.[4] Another interesting phenomena observed in metal nanoparticles is that surface plasmon band is of high intensity as compared to interband transition. When surface plasmons are excited a large density of free electron cloud interacts generating a huge electric field within the particle which extends much beyond the geometrical boundary of it. This generated field is in opposite direction to the incident electric field and interferes destructively, thus surface plasmon band can have higher extinction much beyond the NP surface as compared to interband transition. As a result these electron oscillations

induce electric field enhancements (Figure 1.2) within the close proximity of metal nanoparticles (under 10 nm).[6]

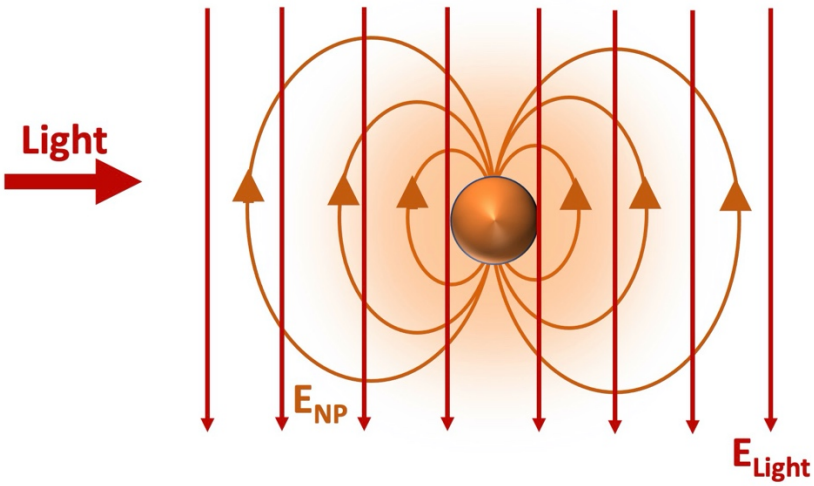


Figure 1.2. Electric field enhancement near the surface of nanoparticle in presence of applied external electric field.

## 1.2 Theoretical models

Surface plasmons corresponds to the interaction between free electrons and incident electromagnetic radiation. So, solving the maxwells equations with certain boundary conditions explains the optical properties of metal nanoparticles. This analytic studies were first performed by Gustav Mie in early 20th century.[7–11] Mie theory assumes particles are well separated between themselves so that the external field of one nanoparticle does not interfere with the others, so the analytic solution is only possible for certain conditions and geometries. Under these conditions Maxwells equations can be solved for spherical NP to get the extinction cross section as follows.[9]

$$\sigma_{ex} = \frac{2\pi R^2}{|k|^2} \sum_{L=1}^{\infty} (2L+1) Re[a_L + b_L] \qquad (1.1)$$

where,

$$a_L = \frac{m\psi_L(mx) \,.\, \psi'_L(x) - \psi_L(x) \,.\, \psi'_L(mx)}{m\psi_L(mx) \,.\, \eta'_L(x) - \eta_L(x) \,.\, \psi'_L(mx)}$$

$$b_L = \frac{\psi_L(mx) \,.\, \psi'_L(x) - \psi_L(x) \,.\, m\psi'_L(mx)}{\psi_L(mx) \,.\, \eta'_L(x) - \eta_L(x) \,.\, m\psi'_L(mx)}$$

Where $x = |k| \cdot R$, R is the NP radius, k is the light wavevector in the dielectric medium, $m = n/n_m$, $n$ and $n_m$ are refractive index of the material and surrounding medium. $\psi_L$, $\eta_L$ are cylindrical Bessel-Riccati equations. Mie theory strongly depends on dielectric constants of the particle and their surrounding medium. The dielectric constants of metal nanoparticles contain real and imaginary parts and are frequency dependent.[12,13] The real part deals with the LSPR position and imaginary part gives the information about damping or dephasing of the electrons.[10]

### 1.2.1 Dielectric constant of Noble metals

A simple model for dielectric constant of metal nanoparticles is first given by Drude model.[12,13] In this model conduction band electrons are treated as free electron cloud or free electron gas. Dielectric constant of the small nanoparticles is effected by surface scattering of these free electrons. Therefore to account this a size dependent damping term must be included in the Drude model.[10,1415] Solving the equation of motion for a single electron gives the response of NPs to the incident electromagnetic radiation, multiplying this by number of electrons per unit volume yields the general expression for dielectric constant as follows

$$\varepsilon(\omega) = 1 - \frac{\omega_p^2}{\omega(\omega + i\gamma_b)} \qquad (1.2)$$

Where, $\omega_p$ is the plasma frequency, $\gamma_b$ is the bulk damping constant, $\omega\ is\ the\ natural\ frequency$. The damping constant is related to the mean free path (l) of the

electrons in the nanoparticle by $\gamma_b = \frac{\upsilon_f}{l}$ , $\upsilon_f$ is the Fermi velocity.[12,13] The bulk plasma frequency with density of electrons (n), effective mass($m_e$) and vacuum permittivity($\varepsilon_0$) is given by

$$\omega_p = \sqrt{\frac{ne^2}{\varepsilon_0 m_e}} \qquad (1.3)$$

For small nanoparticles with sizes less than the bulk mean free path, the damping constant varies as a large number electrons experience surface scattering, which changes the effective path length ($l_{eff}$). [14,15] In the case of small NPs, the effective damping constant in Equation 1.2 modified as

$$\gamma(l_{eff}) = \gamma_b + \frac{A\upsilon_f}{l_{eff}} \qquad (1.4)$$

A is a constant that depends on the interaction of electron and surface.[16,17] The $l_{eff}$ depends on the size and shape of the particles, and for various shaped particles this can be measured using 4V/S formula. Here, V is the volume and S is surface area of the particle.[16,18] The Drude model gives good description for the dielectric constant of the noble metals like gold and silver in the near IR region, but it fails near the UV-Visible region since there is an overlap of interband transitions there.[19,20] Frequency dependent damping is observed with interband transitions. Adding an extra term corresponds to interband contribution ($\varepsilon^{ib}(\omega)$) in Equation 1.2 can resolve this.[20,21]

$$\varepsilon(\omega) = \varepsilon^{ib}(\omega) + 1 - \frac{\omega_p^2}{\omega(\omega + i\gamma(l_{eff}))} \qquad (1.5)$$

The electron surface scattering term plays an important role when the size of the nanoparticle is below the bulk mean path length of electrons i.e, 20 nm. There are various theoretical

calculations for other complex structures other than simple spheres and for particles of different size regimes. Rod shaped particles are better described by Gans theory.[22–24] Particles with other shapes can be better described by the numerical methods such as discrete dipole approximation (DDA)[25,26] or finite element calculation.[27] In the DDA method any shaped particle is assumed to be a ensemble combination of small spheres of that shape. The effective field at the each sphere is taken as the sum of external field induced by other particles and incident electromagnetic field. This way any shape can be approximately calculated.[7,28]

### 1.3 Effect of shape on surface plasmons

The resonance of the surface plasmons is greatly dependent on the shape of the particles. Charge accumulated near the surface of the nanoparticle dictates the restoring force thereby resonance frequency.[28,29] A very simple example would be the case of rod shaped particles (Figure 1.3). For the rod shaped nanoparticles, charge is accumulated along the axis (longitudinal mode) and perpendicular to the axis (transverse mode). Since the charge accumulated along the axis is less, restoring force will be less therefore longitudinal mode will be red shifted as compared to the transverse mode which has a higher restoring force and high resonant frequency, i.e, lower wavelength region. In rods by changing the aspect ratio we can tune the surface plasmon peak from UV to near IR region. Tuning the plasmon peak into near IR region has applications in medicine (photothermal therapy (PTT)).[2,30–32] Other geometries like bipyramids, stars, prisms, cubes etc can be made using chemical synthesis.[32] Deviation from spherical particles usually gives plasmon resonances at longer wavelengths.[28]

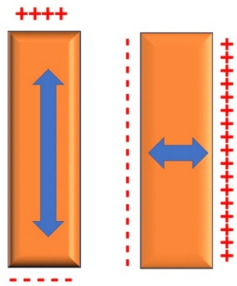

Figure 1.3. Charge accumulation illustration in rod shaped particles, longitudinal and transverse surface plasmons respectively

## 1.4 Effect of surrounding media on surface plasmons

The optical properties of metal nanoparticles are sensitive to the surrounding medium. The dielectric function of the medium determines the wavelength of the incident light near the surface of the particle. This effects the electric field near the surface. In addition, the induced electric field of the NP induces polarization of the dielectric medium. This creates charge accumulation near the interface between metallic nanoparticle and dielectric medium, and this slightly compensates the charge accumulation due to conduction band electrons in the nanoparticle. So stronger the dielectric constant of the surrounding media, stronger the compensation (reduction of charge), leading to reduced restoring force of the charge carriers. This shifts the plasmon band to longer wavelengths or lower energy. Simply, as the refractive index increases near the surface, a red shift in the plasmon band is observed. Similarly, a blue shift (shift towards shorter wavelength) is observed if the refractive index of the medium decreases.[4]

## 1.5 Plasmon coupling and orbital hybridization analogy

When two nanoparticles come within the distance two times the radius, their near fields will interact resulting in large enhancements of local electric field at the junction of these closely spaced particles. This phenomenon is termed as plasmon resonance coupling.[32] Plasmon coupling in nanoparticles is analogous to hybridisation model of atomic orbitals in molecules

(Figure 1.4).[33–35] When two nanoparticles come close and interact, their plasmon bands hybridize resulting in a low energy (red shift) bonding plasmon mode (σ, π) and high energy (blue shift) antibonding plasmon mode ($\sigma^*$, $\pi^*$).[36,37] Plasmon modes with a net dipole moment of zero correspond to dark states and not show up in the optical spectrum. This coupling leads to enhanced electric field in the junction of interacting particles.[38] Coupled nanoparticles have generated significant interest due to the range of potential applications based on their optical response to incident radiation,[39] including Surface Enhanced Raman Scattering (SERS),[40–42] two-photon absorption (TPA),[43] four-wave mixing,[44,45] solar light harvesting[46,47] and optical switching.[46,48] Many of these applications utilize hot electrons and therefore understanding hot electron relaxation dynamics in these systems is critical.

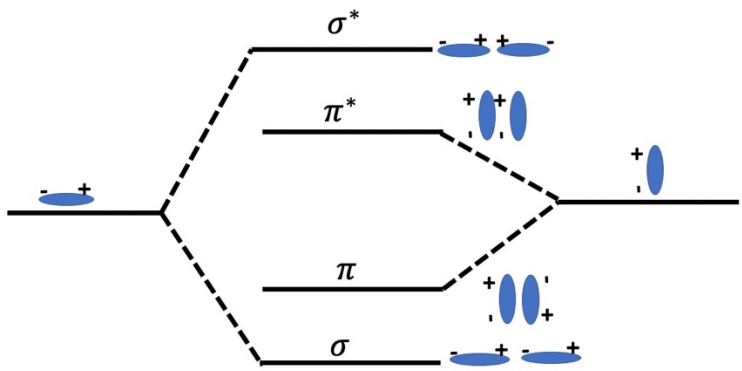


Figure 1.4. Plasmon coupling model analogous to hybridization of atomic orbitals in molecules.

## 1.6 Hot electron relaxation dynamics in nanoparticles post laser excitation

Plasmon resonance dephasing occurs either by intrinsic damping process of the metals or surface scattering of electrons. This process leads to absorption of photons.[12,17] The energy of the photons gets deposited to the electron cloud in metal nanoparticles that spread over conduction band.[49,50] The energy can also be deposited in electron distribution by interband transitions (blue region to the LSPR band) and intraband excitation (red region of the LSPR

band).[51] Information for initial excitation in the conduction band is different for different size and shaped particles. Once the electrons get excited, they quickly thermalize among themselves with few hundreds of femtoseconds.[51–54] After this process, the electrons do not have any memory of how they are initially excited. Now the themalized electrons relax though coupling with the phonon modes of the crystal lattice. This process happens in few picoseconds.[49,54,55] The coupling between the hot electron system and phonon is well explained by a two temperature model (TTM).[50,56–58] Electrons have a much higher heat capacity as compared to the phonon system. So, initially electrons are at a higher temperature and due to the temperature gradient, the generated energy then transfers to phonon system, which is at a lower temperature. The coupling energy between electron and phonon subsystem is given by following differential equation.

$$C_e(T_e)\frac{dT_e}{dt} = -g(T_e - T_l) \qquad (1.6)$$

$$C_l\frac{dT_l}{dt} = g(T_e - T_l) \qquad (1.7)$$

Where, $C_e$ and $C_l$ are the temperature dependent electronic heat capacity ($C_e(T_e) = \gamma T_e$)[12,13] and lattice heat capacity, $T_e$ and $T_l$ are the electronic and lattice temperature, $\gamma\ is\ a\ coefficient\ that\ can\ be\ derived\ experimentally$ and g is electron phonon coupling constant.[56,57] The initial electronic temperature effects the electronic heat capacity ,thereby electron-phonon coupling rate depends on the excitation pulse used.. The electron phonon coupling timescales of the various metal nanoparticles are well studied using transient absorption spectroscopy. The goal of these studies is to find the dependence of size and shape on electron phonon coupling rates.[49,55,59] However, these studies are challenging because the relaxation times are highly dependent on excitation laser power. Researchers have been solving this problem by two different ways. Firstly, exciting the sample with very low power and

observing the dynamics.[49,60,61] Secondly, exciting the sample with a series of pump powers and extrapolating the results to zero power.[30,31,55] Both the methods give good estimation of the electron phonon coupling constant. Pump probe experiment show that typical time scale of electron phonon coupling in high conductive metals like gold, silver is around 1 ps, whereas for metals like platinum it is much faster due to a large electron-phonon coupling constant.[58,62] The optical excitation of metal nanoparticles with laser increases the lattice temperature from few kelvins to tens of kelvins.[63–67] Raising the temperature of the lattice leads to expansion of the particle.[65,67,68] The expansion coordinate of the particles consists of a linear combination of normal vibrational modes.[30,49,69] The time scale for heating of particles greater than 10 nm is usually few tens of picoseconds which is faster than the periods of vibrational modes. This implies vibrational modes which corresponds to the expansion of the particle can be coherently excited.[30,49,70–73] Transient absorption studies of coherently excited vibrational modes have been examined for different size and shaped nanoparticles.[47]

After the electron-electron thermalization and electron-phonon coupling the energy is lost to the surroundings in two ways, heat transfer between interface and surrounding and heat dissipation in the surroundings.[49,59] Interface conductance is given by Equation 1.8.

$$C_e(T_e)\frac{\partial T_p}{\partial t} = -\frac{3G}{R\rho_p C_p}(T_p(t) - T_s(R,t)) \qquad (1.8)$$

Where, G is interface thermal conductivity, $\rho_p$ $and$ $C_p$ are density of the particle and heat capacity of the particle.[74] $T_p$ and $T_s$ are the temperature of the particle and temperature of the surrounding respectively. Heat diffusion in the surroundings for spherically symmetric particle is given by Equation 1.9.[74]

$$\frac{\partial^2(rT_s)}{\partial t} = \frac{1}{\alpha_s}\frac{\partial(rT_s)}{\partial t} \qquad (1.9)$$

Here, $\alpha_s = \frac{\Lambda_s}{\rho_s C_s}$ is thermal diffusivity. $\rho_s$ , $C_s$ and $\Lambda_s$ are density, heat capacity and thermal conductivity of the surrounding. Solving Equations 1.8, 1.9 gives the rate of cooling of the particle.[75–77]

The sequence of events post laser excitation of metal nanoparticle is shown in Figure 1.5. Typically dephasing occurs in 10s of femtoseconds, electron-electron thermalization occurs in hundreds of femtoseconds, electron-phonon coupling in 1-5 picoseconds and finally heat dissipation occurs in 10-100 picoseconds. The typical time scales vary depending on the size, shape and laser power used to excite the samples.[2,31,51,55,78]

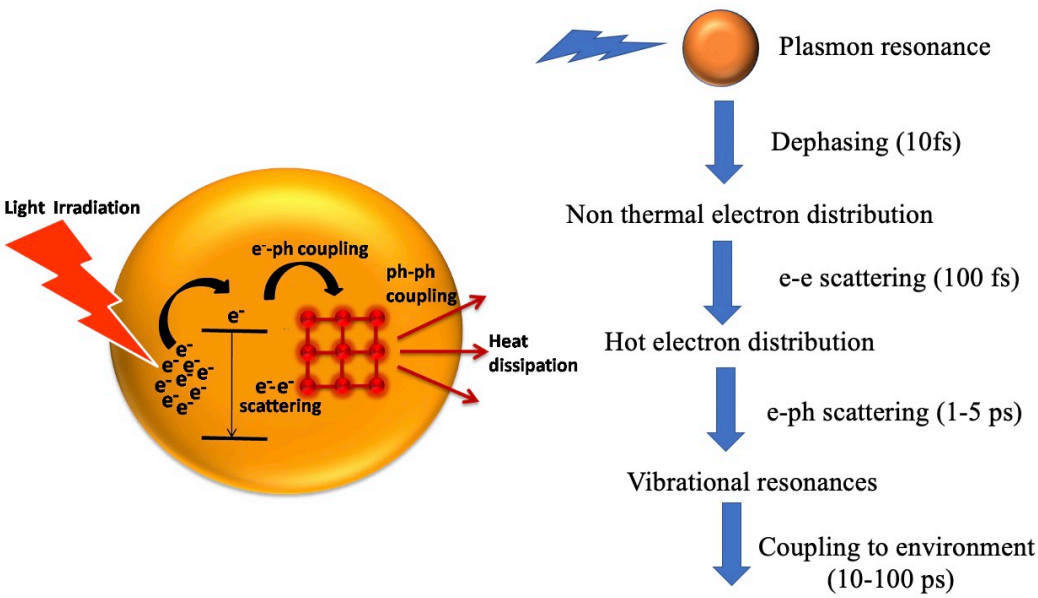


Figure 1.5. Sequence of events post laser excitation of metal nanoparticles.

Researchers around the world have conducted experiments to find the correlation between size and shape dependency of these hot electron relaxation dynamics. At very low power the electron-phonon coupling time in metal nanoparticles is found to be less than 1 ps. This is of the same scale as electron-electron thermalization. Moreover, these timescales are probe wavelength dependent. Choice of probe wavelength is shown to effect the time scale of

electron-phonon coupling times. Due to all these factors there are lot of inconsistencies in the literature regarding the hot electron dynamics in these systems.[30,49,79]

### 1.6.1 Size and shape dependence of hot electron relaxation dynamics in metal nanoparticles.

Transient absorption studies performed on Ga and Sn revealed that the electron-phonon relaxation time decreases with decrease in size of the particle.[80,81] This trend was attributed to enhanced electron-surface scattering for smaller particles.[82] Meanwhile other groups have shown no dependence of size on the electron-phonon coupling time and some have shown electron cooling slows in small particles.[54,83–85] Among vast number of studies, studies by Vallee and Del Fatti are widely accepted.[61,86] Their studies at low perturbation regime with low noise data reveal that both electron-electron and electron phonon coupling times decreases i.e, they get faster in size regime below 10 nm. This faster coupling time scales was attributed to electron spill effect at the boundary of the nanoparticle of smaller sizes, which reduces the electron density, leading to reduced screening between electrons and increased interaction between electron and phonon subsystem.[61,87] Hot electron relaxation dynamics of gold nanorods reveal that electron-electron and electron-phonon dynamics are similar to those of bulk gold. Some recent studies on gold nano shells reveal faster dynamics as compared to bulk gold.[88] Overall these experiments reveal that electron dynamics of metal nanoparticles below the 10 nm size regime exhibit significant changes, but shape is not a very important factor.

### 1.6.2 Hot electron relaxation dynamics in coupled nanoparticles

Transient absorption studies have been majorly carried out on isolated nanoparticles of different sizes, shapes and materials. Coupled nanoparticles are of great interest due to their property of localizing the incident electric field much efficiently in the gap between the two

closely spaced particles and their applications in surface enhanced Raman scattering.[89–93] Hot electron relaxation dynamics of thick films and large aggregates in solution showed fast relaxation dynamics,[60,94] whereas aggregated hollow gold nanoparticles and gold necklaces showed slower dynamics.[88,95] This discrepancies could be due to various environments they have been prepared in. In addition, the role of surface ligands and environment on hot electron relaxation dynamics is not well understood. Further, the optical response of coupled nanoparticles is very complicated due to their broad absorption and probe wavelength dependent dynamics.[49,78]

## 1.7 Quantum dots

Quantum dots (QD's) are semiconductor nanoparticles of the size regime of few tens of nanometers based on the material. Generally, they consist of few thousands of atoms depending on the size forming a crystal lattice structure.[96–99] Their morphology consists of inorganic core and organic surface molecules surrounding the core. The inorganic core is responsible for all the optoelectronic properties of the quantum dot whereas surface organic ligand molecules acts as a stabilizers providing colloidal stability. Quantum dots have properties intermediate to the bulk materials and the single molecules. The uniqueness in the properties of quantum dots comes from the dimension of the particles. Quantum dot properties can be described by particle in a three dimensional box with potential well model.[96–99] Due to these properties, the charge carriers in QDs are confined to small spaces which are otherwise free in bulk materials. This confinement of charge carriers leads to many size and shape dependent optoelectronic properties. The research in quantum dots started in early 1980's through work of L. Brus, A.I. Ekimov and A.L. Efros.[100,101] Since then the research in this field turned multidisciplinary with various applications in biomedical,[102–104] thermoelectrics,[105] optoelectronics,[106] solar light harvesting,[107–110] light emitting devices[111–113] etc. Tunablity of

properties with the function of size and shape combined with the manipulation of physico-chemical properties made quantum dots an unique material with wide range of applications. The quantum confinement effect in quantum dots enables the size and shape dependent tunablity of optical, electronic and charge transport properties.[96–98] Irrespective of the material, quantum dots show tunablity of size dependent optical properties in absorption and photoluminescence(PL).[114,115] Just by decreasing the size of the quantum dots, we can have a blue shift in absorption maxima and photoluminescence of the QDs. With the advent of chemical synthesis from the past two decades, it is now possible to tune the optical properties of QDs from Ultraviolet (UV) region to although near infra-red (NIR) region.[102,114,115] In addition, quantum dots shows broad two photon absorption i.e., a large absorption cross section with a high molar extinction coefficient, narrow photoluminescence band, high quantum yield of photoluminescence and high photothermal stability.[96] Due to these wide range of superior optical properties, the quantum dots find applications in solar cells, lasers, light emitting devices, optical storage devices, chemical sensors, bio imaging sensors etc.

## 1.8 Energetics of bulk semiconductor crystals

To understand the quantum confinement effect in semiconductor nanocrystals, one needs to understand the basic band electronic structure of bulk semiconductors. The microscopic behaviour of electrons in crystalline solids i.e., periodic arrangement of atoms are considered to be in periodic electric potential field.[116–119] In metals, the electrons are loosely bound and are free to move, but in insulators they are tightly bound. The electrons in semiconductors lie somewhat in between metals and insulators. The time dependent Schrodinger's equation of single electron in a solid crystal in one dimension is given by

$$\frac{-\hbar^2}{2m}\frac{d^2\Psi(x)}{dx^2} + V(x)\Psi(x) = E\Psi(x) \qquad (1.10)$$

$$V(x) = V(x + na); n = 1,2,3, \ldots. \qquad (1.11)$$

$$V(x) = \sum_{n=-\infty}^{\infty} V_n e^{i2\pi x/a} \qquad (1.12)$$

$$\frac{-\hbar^2}{2m}\frac{d^2\Psi(x)}{dx^2} + \left[\sum_{n=-\infty}^{\infty} V_n e^{i2\pi x/a}\right]\Psi(x) = E\Psi(x). \qquad (1.13)$$

Where, m is mass of the electron, E is the allowed electron energy, V(x) is the potential energy felt by electron, a is the crystal lattice constant and $\Psi(x)$ is the electron wave function.[116–119]

Solving the Schrodinger equation using Bloch functions gives the energy of the electron in crystal lattice and thereby information of electronic band structure can be obtained.[116–119] The energy of the electron obtained is similar to the free particle (Equation 1.14). Here, k is the wavenumber of the incident particle.

$$E = \frac{\hbar^2 k^2}{2m} \qquad (1.14)$$

Semiconductors show threshold of photon absorption energy. This is defined as a band gap of the semiconductor which plays an important role in controlling its optical properties. Crystalline solids have large number of closely spaced energy levels which forms its energy bands. These bands are the collection of individual energy levels of electrons. Pauli exclusion principle does not allow the electrons to have same energy levels of closely spaced atoms in a crystalline solid. This results in formation of closely spaced energy levels forming bands.[120] The band formation model of metals, semiconductors and insulators is shown in Figure 1.6. The gap between the conduction band and valence band, which is termed energy gap, is the characteristic property of the bulk material. Fermi level is another important characteristic parameter in bulk materials. It is described as a hypothetical energy level which have 50%

probability of being occupied at a given time under thermodynamic equilibrium.[116–119] The position of the Fermi level with respect to conduction band and valence band determines the nature of material and governs its opto-electronic properties.

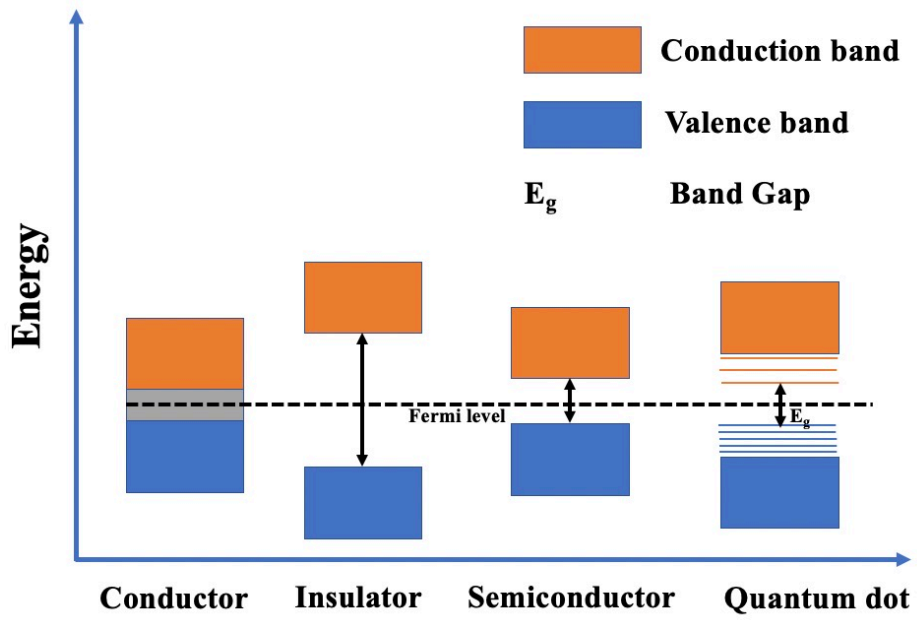


Figure 1.6. Electronic band structure of Conductor, Insulator, Semiconductor and Quantum dots.

In conductors, valence band and conduction band overlap and the Fermi level lies in that overlap region. There is a huge energy gap between valence band and conduction band in insulators. The Fermi level lies within the bandgap in semiconductors and it can be populated by optical and thermal excitations and partial conducting behaviour is observed. Upon thermal and optical excitations, an electron and hole pair is generated. Due to coulombic attraction between these two charge carriers they are in a “bound state” and is called an “exciton”. In a crystal lattice these excitons are highly delocalized over several lattice sites, known as “Wannier exciton”.[116–119] In its bound state, exciton is a electrically neutral quasiparticle. The motion of this exciton can be thought as similar to modified hydrogen atom which moves in

crystal within effective mass approximation.[116–119] Excitons experience screened electrostatic coulomb force. In the exciton bound state, the distance between the electron and hole is known as the "exciton-bohr radius ($a_B$)" (shown in Figure 1.7). Exciton formed remains in a dielectric medium therefore exciton-Bohr radius can be determined by the bulk optical dielectric constant of the material. Exciton-Bohr radii of a bulk exciton is given by the following Equation 1.15.

$$a_B = \frac{\hbar^2 \varepsilon}{e^2}\left[\frac{1}{m_e^*} + \frac{1}{m_h^*}\right] \qquad (1.15)$$

Where, $m_e^*$ and $m_h^*$ are the effective mass of electron and hole respectively, e is the elementary charge, "$\varepsilon$" is the bulk dielectric coefficient or relative permittivity. The excitons generated can be normalized by a recombination event either by radiation which is in the form of photons or in the form of thermal energy which is in the form of phonons.

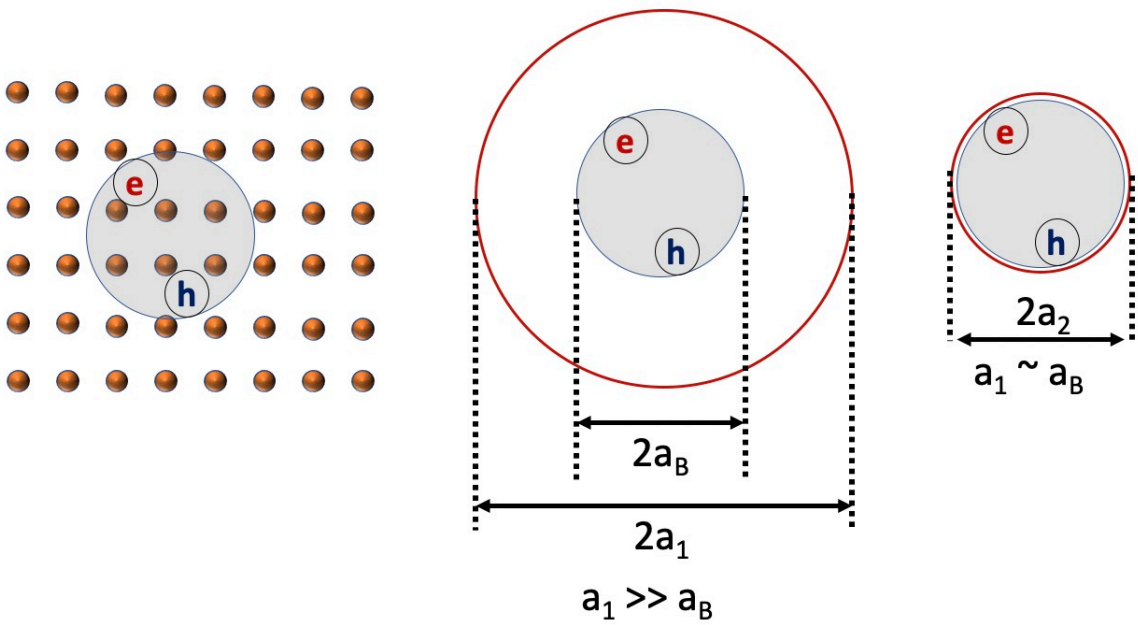


Figure 1.7. (a) Schematic of exciton delocalized in crystal lattice (b) Exciton in bulk, where exciton-Bohr radii is smaller than dimension of the material (c) Exciton in quantum dots, where exciton-Bohr radii is comparable to the size of the material.

## 1.9 Confinement effect in Nanocrystals

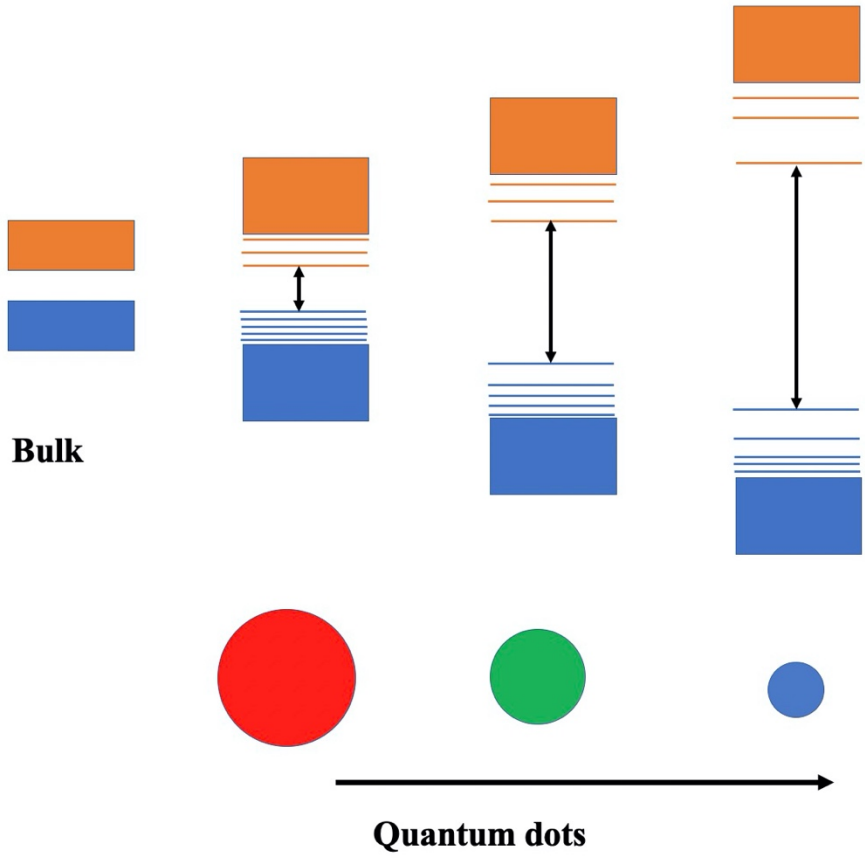


Figure 1.8. Quantum confinement effect in quantum dots as a function of size.

Properties of the materials in bulk regime depends on chemical composition but not on their size and shape . When the size of the crystal lattice decreases to nanometer size regime, material properties depend on size, shape and surface area to volume ratio. This size dependence on material properties specifically arise when size of the particle is comparable to the exciton-Bohr radius of the nanomaterial.[96–98] As the size of the material decreases to the limit of exciton Bohr radius, the motion of the exciton is confined and it cannot extend beyond the boundary of the nanomaterial. This spatial confinement of excitons lead to quantum confinement of the exciton wave function. This spatial confinement changes the electronic structure of the nanomaterial as compared to bulk particle. The confinement results in quantization of energy bands and both density of states energy separation between them gets effected. The continuous

electronic bands near the edge of valence band and conduction band become discrete quantized energy levels as shown in Figure 1.6. This Quantization effect in quantum dots is strongly size dependent (Figure 1.8).[96–98,121–125] The energy difference between these discrete energy levels increases as the size of the particle decreases. As a result size dependent optoelectronic properties of the quantum dots is obtained.[96–98,122–125] The quantum confinement effect in quantum dots allows us to tune the optical properties like absorption and photoluminescence (PL) in the wide range of optical spectrum just by keeping the composition of the material constant and by changing the size of the material.

## 1.10 Electronic energy structure in semiconductor quantum dots

The simplest model used to describe the quantum confinement effect in semiconductor quantum dots is "particle in a three dimensional spherical box", based on "effective mass approximation method".[100,126–129] This method gives an approximate solution for the size dependent electronic structure in quantum confined particles. Simply it gives the band gap of quantum dots as a function of its size. Within the quantum dots, coulombic and confinement potentials are operative on exciton. Based on all the considerations discussed above, Brus et.al showed the lowest energy electronic transition can be approximately calculated for CdE (E= S, Se) by following Equation 1.16,[100,127]

$$E_g(1Se - 1Sh) = E_g + E_{conf}^{e} + E_{conf}^{h} + E_{coul}$$

$$= E_g(bulk) + \frac{\pi^2\hbar^2}{2R^2}\left(\frac{1}{m_e^*} + \frac{1}{m_h^*}\right) - \frac{1.8\, e^2}{\varepsilon R} \qquad (1.16)$$

Where, $E_g$ is the band gap of the bulk semiconductor, $E_{conf}^{e}$ $and$ $E_{conf}^{h}$ are the confinement energy potential of electron and hole respectively. $E_{coul}$ is the coulombic interaction of hole and electron, R is the radius of the quantum dot and $\varepsilon$ is the bulk dielectric constant. As the

size of the quantum dot decreases, the confinement potential energy increases by the factor $1/R^2$. This leads to increase in band gap of quantum dots as compared to bulk material. The coulombic interaction effect is less compared to potential energy confinement with varying size.[100,127] The electronic structure in quantum dots is described in terms of series of excitonic states.[98,130,131] These discrete electronic states get manifested in optical spectra of QDs (absorption, photoluminescence). Other than lowest energy state of exciton, high energy states are also effected by the size induced quantum confinement effect as shown in Figure 1.9.

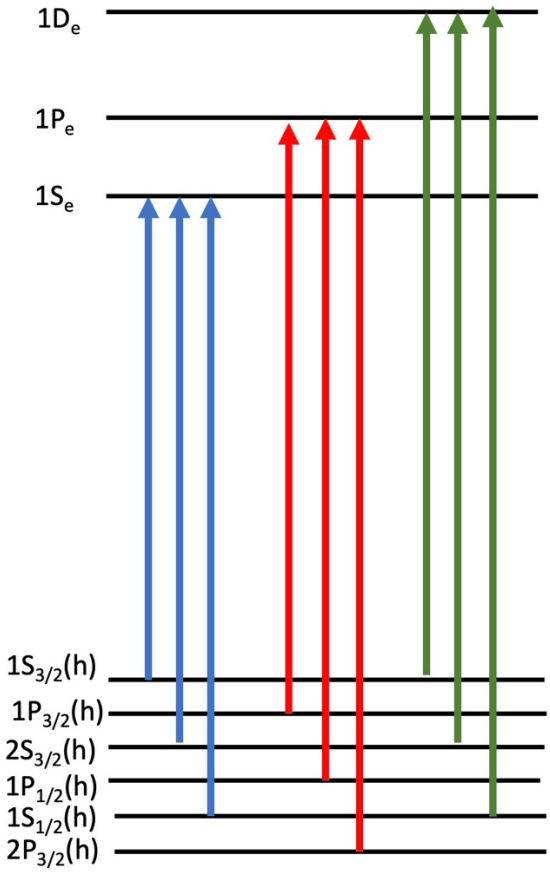


Figure 1.9. Discrete atomic like states in conduction band and valence band of quantum dots. Complex structure of valence band is due to mixing of different hole sub bands.

## 1.11 Effect of surface on optical properties of quantum dots

The optical properties of quantum dots are greatly dependent on their surface.[132–135] With the decrease in the size of the quantum dots, surface to volume ratio increases and large number of atoms are at the surface. These atoms at the surface are different when compared to atoms inside the QDs. The inner atoms are completely bonded and complete their valency, whereas atoms at the surface are not. These unsatisfied valency sites of the atoms at the surface creates non bonded energy states in the band gap of quantum dots. These are known as "dangling bonds" (shown in figure 1.10).[132–135]

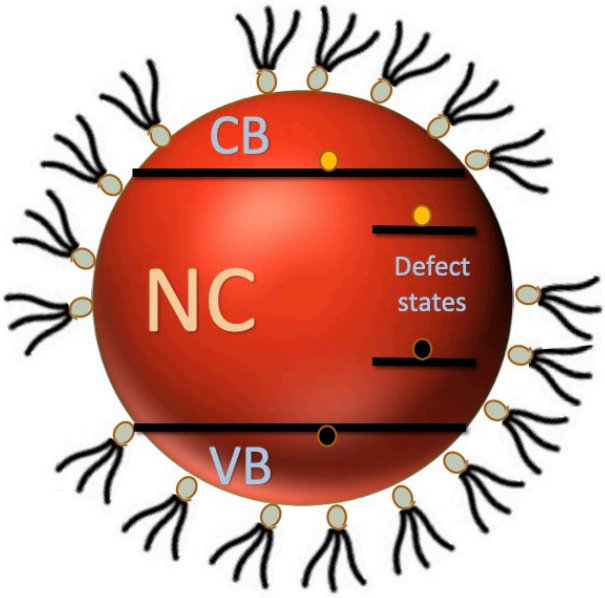


Figure 1.10. Defect states formed in band gap of quantum dots due to lack of passivation of surface atoms

These energy states which are present in the region between conduction and valence band of quantum dots often trap the excited charge carriers. This is a detrimental effect of optical properties in QDs. Trapping of charge carriers by these mid gap dangling bonds increases the chances of non-radiative recombination of charge carriers and decreases the photoluminescence quantum yield (PLQY).[136] During the synthesis of quantum dots, long

chain stabilizing organic molecules (fatty acids, amines, thiols etc) are used to prevent aggregation and induce colloidal stability of quantum dots.[136] These molecules passivate the surface dangling bonds by covering them to some extent. These ligand molecules attach to the surface by metal-ligand bonding. However these organic molecules are in dynamic equilibrium with free organic molecules in the solution. Therefore perfect passivation of dangling bonds cannot be achieved. In addition, the surface of semiconductor nanocrystals are prone to oxidation and reduction.[137] Oxidation of the surface generates defect states and it effects the photoluminescence(PL) and stability of QDs.[137]

### 1.12 Excited states in semiconductor nanocrystals

Excited state properties of the charge carriers in semiconductor nanocrystals govern their optoelectronic properties and device performance.[120] Electron in the valence band of semiconductors can be excited by photons of energy equal or above the band gap. The semiconductor is now out of equilibrium and subsequent charge carrier relaxation dynamics occur through a variety of mechanisms. Huge number of theoretical and experimental studies of excited state dynamics in semiconductors have been studied.[138–140] If the absorbed photon energy by the electron is greater than the band gap. The excess energy is stored as kinetic energy in carriers. Such carriers are not in equilibrium and cannot be described by Boltzmann statistics.[141] The initial carrier distribution reaches equilibrium by rapidly interacting with each other through carrier collisions forming a quasi-equilibrium with Boltzmann like distribution. The carrier with extra kinetic energy at higher levels in conduction band as known as “hot carriers”. The carrier-carrier interaction is called carrier thermalization which typically happens at a fast time scales (<100 fs).[141] After carrier thermalization hot carrier equilibration with lattice occurs through carrier phonon interaction. Phonons are typically optical vibrational modes of the material.[141] This excess energy is lost to phonons though Auger process and other

separate interactions which will be discussed in coming sections. The carrier cooling process takes place until carriers heat the lattice and reach thermal equilibrium with each other.

### 1.12.1 Carrier types

#### 1.12.1.1 Free carriers and excitons

The bound electron-hole pair is an independent quasi particle with net neutral charge.[142] This bound pair exciton has internal energy lower than unbound electron and hole with its binding energy of the order of meV in inorganic semiconductors. In order to use the excitons in photocurrent devices, excitons needs to be dissociated into their free charge carriers. This is a significant limitation in organic semiconductor materials since the dissociation of excitons is typically of the order of ~1eV which is huge.[143] However, the excitons typically recombine giving a photon which has applications in light emitting devices.

#### 1.12.1.2 Hot carriers

Hot carriers which were discussed in the earlier section shows a great promise in devices such as solar cells allowing to break the 33% Shockley-Queisser limit thereby increasing the efficiency of light harvesting materials manifold.[144] It is typically very hard to examine hot carrier dynamics due to their typically short lifetimes and their unclear manifestation in optical measurements.[145146]

#### 1.12.1.3 Polarons

In highly polar crystals or ionic crystals, the coulombic force of interaction between conduction electrons and lattice ions takes place resulting in strong electron-phonon coupling. In such cases, electrons are surrounded by huge number of virtual phonons.[147] The electron push or pull the surrounding lattice ions depending on their charge. The electron and virtual phonon

can be treated as a special quasi particle called “polaron”. Polarons can have a strong influence on charge transport properties in semiconductor nanocrystals. The basic polaron theory and how it effects the carrier-carrier interaction is still being refined to the present day.[147]

### 1.13 Recombination mechanisms in semiconductor nanocrystals

Recombination of excited charge carriers plays an important role in determining the applications of quantum dots in various devices. It can be a limiting factor for devices such as light emitting diodes or solar cells. In this section, different charge recombination mechanisms in semiconductor nanocrystals will be discussed.

Geminate recombination is the process where electron-hole pair which is bound by coulombic interaction(exciton) recombine. Their recombination is accompanied by the generation of photon. The carrier separation in excitons is required for charge carrier extraction for photovoltaic applications.[142] Non geminate process is where the free carriers recombine i.e., free electron and free hole recombine either radiatively or non-radiatively.

Trap assisted recombination process is where either one of the charge carrier or both the charge carriers gets trapped in the defect states formed in band gap region by surface dangling bonds. The trapped charge carrier often recombine non radiatively and difficult to extract. Thus it is a undesirable mechanism. The trapped electron in the defect state can recombine with a hole of its trapped state.[120]

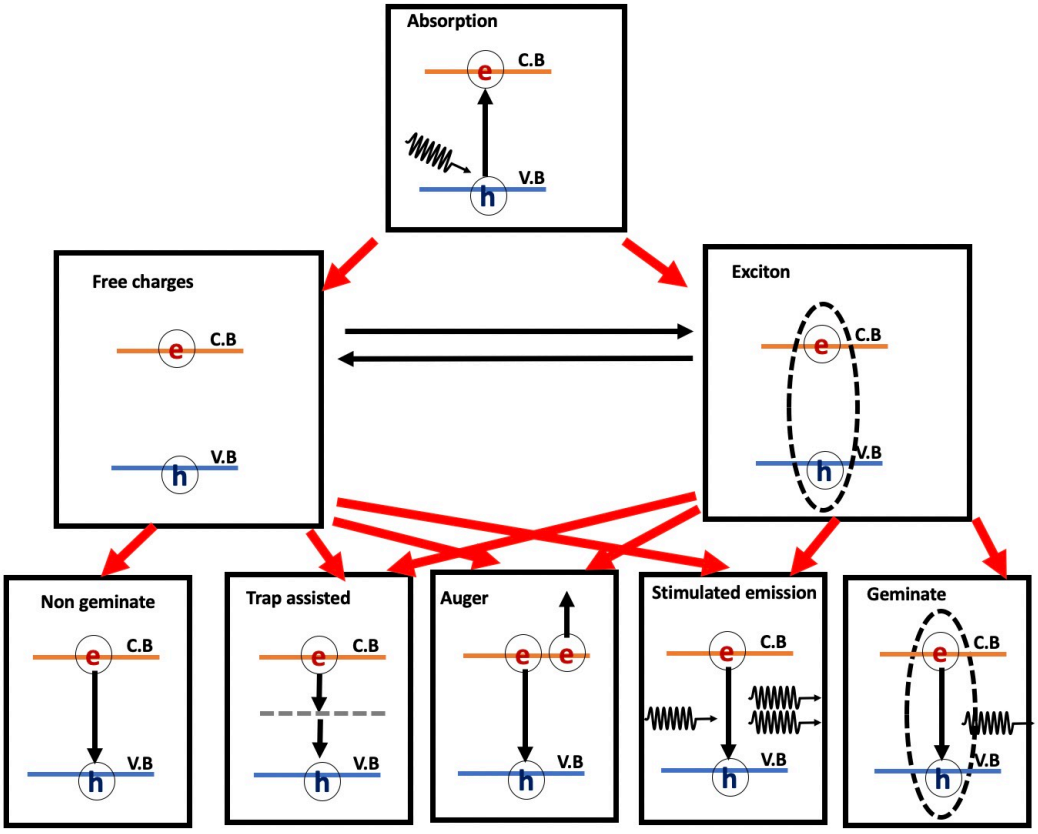


Figure 1.11. Schematic representation of various carrier recombination mechanisms.

Stimulated emission is a special case of radiative recombination. When an incoming photon induces the recombination of excited electron with its hole instead of exciting an electron from valence band to conduction band, it does so with the emission of a photon of same phase, frequency, polarization and direction similar to incoming photon. This leads to amplification of the emitted light under a certain set of conditions. This phenomena is widely used in making laser system.[142] The schematic mechanism is depicted in the Figure 1.11.

Auger recombination process is a non-radiative process. For a Auger process to occur, three charge carriers are required.[120] Either two holes and one electron or two electrons and one hole. During the recombination of one set of electron-hole pair, the energy released is transferred to the third particle sending it to higher excited states in its band. This high energy carrier then relaxes non radiatively by transferring its energy to a phonon subsystem.[148]

### 1.13.1 Hot exciton relaxation

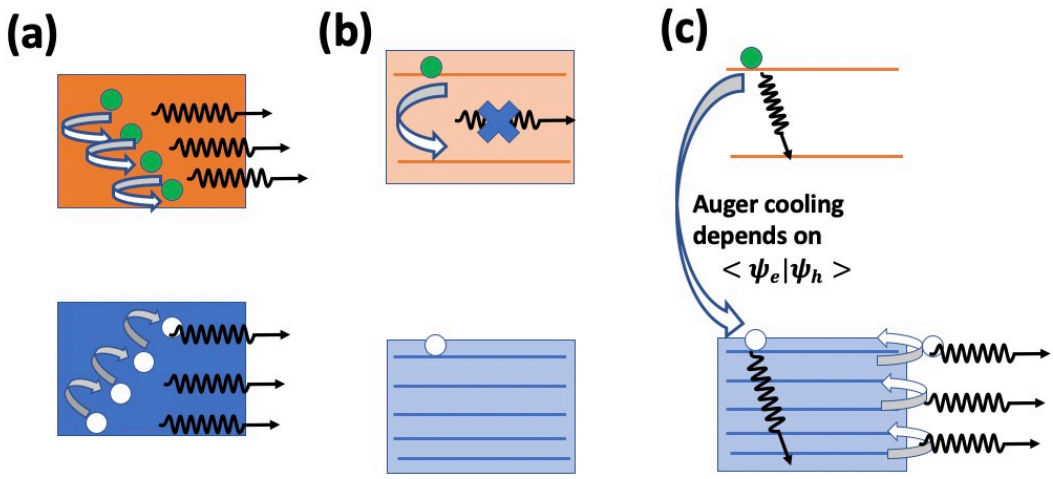


Figure 1.12. (a) Hot carrier relaxation in bulk materials through phonon emission (b) Phonon bottleneck in QDs (c) Auger assisted cooling by transferring its excess energy to hole.

When excited with energy much higher than the band gap of the QDs, hot electrons are generated (carrier lies in the higher intraband states). In bulk semiconductors there are continuous closely spaced energy levels (shown in Figure 1.12). So the excess energy of the charge carriers can be lost via phonon emission. In QDs the intraband energy levels of electron in the conduction band are well separated with a gap of ~1eV. It cannot relax via phonon emission since phonon energies are typically in the range of few meV. Due to this hot electron has to relax through multiple phonon emissions which is a very slow process. This expected slow cooling of hot electrons in quantum dots is known as "Phonon bottleneck".[149–155] One predominated mechanism here is Auger assisted cooling. The hot electron by coupling with its hole transfers its excess energy.[149–151,156–158] Holes having higher effective mass compared to electrons also have high density of states and it can easily relax through phonon emission. Then the decoupled electron relaxes slowly. In the absence of the hole, i.e., when hole is trapped the electron can relax through other mechanisms where it transfers its excess energy to vibrational mode of surface ligand.

## 1.14 Metal-semiconductor hetero nanocrystals

Metal-semiconductor hetero nanocrystals are important class of materials . In these materials, metals are grown directly on the surface of semiconductor nanocrystals giving rise to exciton-plasmon coupling effects.[159–166] When these materials are excited the electron in the conduction band of the semiconductor jumps to metal nanoparticle leaving the hole behind. This charge carrier separation has a applications in photocatalysis, solar cell, water splitting etc. The studies on hetero nanocrystals was started from the work of Mokari et al. where they have grown Au tips CdSe rods and CdSe tetrapods.[161] Since then various metals like Au, Ag, Pt, Co etc. have been grown on various semiconductor nanoparticles.[159,160,167–170] TA measurements can be employed to study the charge separation and other recombination mechanisms in the hetero nanocrystal systems.[167,168,170–172]

The thesis is organized as follows

**Chapter 2** contains synthetic procedures of gold nanoparticle assemblies, metal-semiconductor heterostructures, $TiO_2$ nanoparticles and phenothiazine porphyrin molecules. It also gives brief overview of the instrumentation of steady state spectroscopy and ultrafast transient absorption.

**Chapter 3**, we report hot electron relaxation dynamics in GNP dimers and trimers, prepared by self-assembly using a dithiol linker. Surface modification of MNPs with these linker molecules yields functional assemblies. With dithiol linkers, it is possible to obtain assemblies with small interparticle spacings and consequently, greater plasmon coupling. Dimers and trimers formed in the solution phase are further purified using gel electrophoresis. Understanding the electron relaxation dynamics in these systems can be exploited for

optimizing the photochemical reactions and electron transfer reaction between metal semiconductor nanoparticles or molecular adsorbates.

**Chapter 4** presents studies of electron transfer dynamics in cubic shaped PbS-Au heterostructures using transient absorption spectroscopy. We analyzed the electron transfer rates and charge relaxation dynamics from $1S_e$ and $1P_e$ states of conduction band from excited state absorption dynamics experiments from pump probe data. Ultrafast charge separation at the junction of the metal-semiconductor interface before Auger recombination and other relaxation channels is observed which is very crucial for the development of solar cells where multiple charge carriers created from the MEG can be extracted efficiently leading to overcome Shockley-Queisser limit.

**Chapter 5** presents ultrafast charge relaxation dynamics in CZTS-Au nano heterostructures at different pump fluence energies. Pump probe data of the transient absorption spectroscopy shows photoinduced absorption in the entire probe region suggests the domination of excited state absorption over ground state bleach. Transient absorption spectra in CZTS-Au nanostructures resulted in reduction of the optical density of the ESA suggesting an ultrafast charge transfer faster than the hot electron trapping process and within the instrument response function (200 fs). This ultrafast charge transfer process faster than the trapping process is crucial in optimizing the CZTS based nanostructures in photovoltaic applications.

**Chapter 6** , we have designed a $A_3B$ porphyrin sensitizer in which the three meso-positions were decorated with three phenothiazine moieties tethered to porphyrin core, and the other meso-position is functionalized with phenyl carboxylic acid which can play a dual role as acceptor and anchoring group. A series of phenothiazine-porphyrin systems in which phenothiazine tethered to porphyrin with different linkages such as phenyl, alkynyl, and phenoxyl alkyl linkages and carboxylic acid anchoring group to attach to the semiconductor

nanoparticles such as $TiO_2$ and the efficiency of photo-induced electron transfer and the solar energy conversion to electricity w.r.t. linker sizes were investigated. Efficient charge separation before the charge recombination and other undesired pathways is evident in the studied phenothiazine porphyrin dye in the presence of semiconductor $TiO_2$ nanorods. In addition, tunability of electron injection and back electron transfer rates is observed with different spacers between porphyrin and phenothiazine moieties.

# 2 Materials and methods

## 2.1 Synthesis of gold nanoparticle assemblies

### 2.1.1 Chemicals

Gold(III) chloride trihydrate ($HAuCl_4.3H_2O$, >99.0%), bis(p-sulfonatophenyl) phenylphosphine (BSPP, 97%), 1-9 Nonanedithiol (DT, 95%), sodium citrate (SC, trisodiumcitrate dihydrate), tris base (tris(hydroxymethyl)aminomethane) and O-[2-(3-mercaptopropionylamino) ethyl]-O-methyl-poly(ethylene glycol) (mPEG-SH (PEG5000), MW 5000) from Sigma Aldrich were used as received.

### 2.1.2 Synthesis

#### 2.1.2.1 Synthesis of gold nanospheres

Gold nanospheres were synthesized by the method of Lu et al.[173] Briefly, sodium citrate (30 mM, 1 ml) was added to ultrapure water (14 mL) and heated at 137 $^{o}$C for 90 minutes. $HAuCl_4$ (100 µL, 25 mM) was added to the hot solution, followed by Tris base (500 µL, 0.1 M) after 1 minute. After 20 minutes, the solution temperature was rapidly decreased to 100$^{o}$C by transferring the flask to a preheated oil bath at this temperature. Two additional aliquots of $HAuCl_4$ (25 mM, 100 µl) were added to the solution at an interval of 30 min. The solution was cooled to room temperature and the as-synthesized gold nanospheres were used as prepared for the subsequent steps.

#### 2.1.2.2 Ligand exchange of gold nanospheres

BSPP (90 mM, 50 µl) solution was added to 10 ml of synthesized Au spheres and kept overnight. The solution was concentrated by centrifuging at 7000 rpm for 20 minutes, the supernatant removed and the pellet redispersed in 250 µl of 90 mM BSPP buffer.

#### 2.1.2.3 Assembly of gold nanoparticles

Gold nanoparticle (GNP) assemblies were prepared using the method of Bidault *et. al.* with the following modification.[174] NaCl (1 µL, 90 mM) solution and 1,9-nonanedithiol (1 µL, 0.1mM) were added to the 15 µl of the BSPP coated concentrated Au sphere solution in an eppendorf and left for 30 minutes. Ficol solution (4 µL, 2%) was added and the resulting suspension of thiol- linked assemblies were loaded in 2% agarose gel in 0.5x Tris- Borate-EDTA as running buffer. The gels were run at 8 V/cm for 45 minutes. The extraction procedure was carried out following published protocols to separate dimers and trimers.[175,176]

## 2.2 Synthesis of PbS and PbS-Au nano heterostructures

### 2.2.1 Chemicals

Lead Chloride ($PbCl_2$ ;99.9% trace metal basis), oleylamine (OLA, 70%), octadecene (ODE, 90%), gold(III) chloride ($AuCl_3$; 99.99%; trace metal basis), sulfur (S≥99.99% trace metal basis, dodecanethiol (DDT; 98%), dodecyl mercaptan (t-DDT; 99%) and tri-n-octylphosphane oxide (TOPO; >98%) are purchased from Sigma Aldrich. chloroform, isopropanol, tetrahydrofuran (THF), toluene, ethanol (99.7%; absolute) and methanol are obtained from Merck. Oleylamine (OAm; 70% technical grade) and octadecene (ODE, 90%, technical grade) are degassed and stored in a nitrogen filled glovebox prior to use. The remaining precursors and solvents are used without further purification.

### 2.2.2 Synthesis

#### 2.2.2.1 Synthesis of PbS nanoparticles:

The synthesis is adapted from the procedure reported by Jian et al.[177] $PbCl_2$ (1 mmol, 0.28 g) is dissolved in 5 mL of oleylamine at 90 °C, forming a homogeneous and clear solution. Elemental sulfur (0.33mmol, 10.5mg for 7 nm) is dissolved in 2.5 mL of oleylamine, and the resulting sulfur solution is quickly injected into the optically clear Pb-oleylamine complex solution at 90 °C. The resulting mixture is heated to 220 °C and aged at that temperature for 1 h, resulting in a black colloidal solution. The precipitate is washed twice with toluene/ethanol, centrifuged at 4400 rpm and retrieved by redispersing in toluene producing PbS nanocrystals which is then dispersed in toluene.

#### 2.2.2.2 Synthesis of Au shells on PbS nanostructures

The PbS-Au nano heterostructures are obtained from Monash university, Australia. The detailed synthesis is reported elsewhere.[178]

## 2.3 Synthesis of CZTS nanostructures

### 2.3.1 Chemicals

Copper(II) chloride dihydrate (CuCl2.2H2O; 99.99%), Copper (II) acetate (CuAc); 99%), zinc acetate (ZnAc; 99%) zinc chloride (ZnCl2, 99.99%), tin(II) chloride dihydrate (SnCl2.2H2O, 99.99%) (ODE), oleylamine (OLA, 70%), Octadecene (ODE, 90%) gold(III) chloride (AuCl3; 99.99%), dodecanethiol (DDT; 98%), dodecylmercaptan (t-DDT; 99%) and tri-n-octylphosphane oxide (TOPO; >98%) were purchased from Aldrich. Chloroform, isopropanol, tetrahydrofuran (THF), toluene, and methanol were of analytical grade and obtained from various sources. Oleylamine and Octadecene were used after degassing and was stored in

nitrogen filled glovebox. The remaining precursors and solvents were used without further purification.

### 2.3.2 Synthesis

#### 2.3.2.1 Synthesis of CZTS nanostructures:

CZTS NCs are prepared by the protocol established by Alexey et al.[179] In a typical synthesis, $CuCl_2 \cdot 2H_2O$ (5.4mmol), ZnO (4.8 mmol), and $SnCl_4 \cdot 5H_2O$ (1.8 mmol) is dissolved in THF (0.5mL). Afterward, distilled OLA (24 mmol, 6.43 g) and ODE (20 g) are added to the reaction mixture. The solution is heated under nitrogen to 175 °C and maintained at this temperature for ∼1 h. After purging with nitrogen, the mixture is cooled to 100 °C and 50 mmol of t-DDT and 5 mmol of DDT are added. The solution is then heated to 250 °C and maintained at this temperature for 1 h. The formation of NCs is noted by a gradual darkening of the reaction mixture at ∼135−145°C described in section 2.3.1. Final CZTS NCs are recovered by adding 5mL ethanol in the solution at 80°C and washing with toluene/ethanol mixture. It is then centrifuged at 7000 rpm for 10 minutes, and the nanocrystal precipitate is dispersed in the toluene. The redispersed NC solution is then reprecipitated using the same 1:3 (v/v) solvent: anti-solvent ratio with the same centrifugation conditions. The procedure is repeated twice and is finally filtered and redispersed in the toluene.

#### 2.3.2.2 Synthesis of CZTS-Au heterostructures

The CZTS-Au nano heterostructures are obtained from Monash university, Australia. The detailed synthesis is reported elsewhere.[180]

## 2.4 Synthesis of $TiO_2$ nanorods

$TiO_2$ nanorods have been synthesized using a previously reported method.[181] Briefly, 35 g of oleic acid is taken in a round bottomed flask and heated at $120^0$C with continuous stirring for one hour under nitrogen atmosphere. Vacuum and nitrogen is altered for every 15 minutes to remove moisture inside. 5 mmol of titanium tetraisopropoxide is added to the reaction mixture. After 5 minutes the solution turns from colourless to pale yellow. It is then followed by rapid injection of 2.5 mL of trimethyl amine. The reaction mixture turns to turbid with viscosity increasing gradually up to 90 minutes. Reaction mixture is then kept for overnight stirring followed by washing and redispersing in chloroform.

## 2.5 Synthesis of Phenothiazine porphyrin

Commercially available chemicals and reagents were procured from TCI, Sigma-Aldrich, Spectrochem and Merck. Analytical reagent (AR) grade solvents were used for the reactions while laboratory reagent (LR) grade solvents were used for purifications and column chromatography. *N, N*-dimethylformamide, Dichloromethane, chloroform, acetonitrile and were dried in presence of calcium hydride under nitrogen atmosphere. Toluene and Hexanes were purified using sodium metal added benzophenone by refluxing overnight, distilled under vacuum and stored over 4Å molecular sieves. Triethylamine was distilled with NaOH pellets. Silica gel (100-200 mesh) was used for column chromatography. Thin-layer chromatography was performed on Merck-pre-coated silica gel 60-F254 plates. Flash chromatography was performed for purification of all compounds. The reactions were carried out under nitrogen or argon atmosphere using dry and degassed solvents. Methyl-4-formylbenzoate, Phenothiazine, tetrakis(triphenylphosphane) palladium were purchased from sigma Aldrich. Zinc acetate ($Zn(CH_3COO)_2.2H_2O$) and pyrrole were purchased from Otto chemicals. Sodium hydrogen carbonate ($NaHCO_3$), potassium hydroxide (KOH), N-

Sodium hydrogen carbonate ($NaHCO_3$), potassium hydroxide (KOH), N-Bromosuccinimide (NBS) were purchased from Spectrochem. 4-formylphenylboronic acid was procured from TCI Chemicals. The phenothiazine based precursor, 10-Hexyl-10H-phenothiazine **(Hexyl-PTZ)**,[182] 10-hexyl-10H-phenothiazine-3-carbaldehyde (**2.2**),[183] 3-bromo-10-hexyl-10*H*-phenothiazine (**2.3**),[184] were synthesized according to the reported literature procedures. The $A_3B$ ester porphyrins were prepared by Adler Longo and Lindsey's procedure.[185186] (Please note the compound names mentioned in brackets are from scheme 2.1 and 2.2).

**(a) Synthesis of formyl phenothiazines and their precursors**

**10-Hexyl-10*H*-phenothiazine (Hex-PTZ, 2.1).**[182] A 250 mL round bottom flask was charged with phenothiazine (5g, 25.09 mmol), NaH (1.2 g, 30.1 mmol, 60%) and 120 mL of DMF. The mixture was stirred for 30 min and 1-bromohexane (4.97 g, 30.1 mmol) was then added. The mixture was stirred overnight at room temperature. The reaction mixture was quenched with ice water and extracted with ethyl acetate. The combined organic fractions were washed with brine and dried over $Na_2SO_4$. The solvent was removed under pressure and the residue was purified with silica gel column chromatography using petroleum ether as eluent to give the compound **2.1** as a viscous liquid (6.39 g, 90 %). $^1$H NMR (500 MHz, $CDCl_3$):δ (in ppm): 7.17- 7.14 (m, 4H, *phenothiazine-H*), 6.92 (t, 2H, *J* = 7.5 Hz, *phenothiazine-H*), 6.87 (d, 2H, *J* = 8.0 Hz *phenothiazine-H*), 3.85 (t, *J* = 6.8 Hz, 2H, -$CH_2$), 1.82- 1.79 (m, 2H, -$CH_2$), 1.44-1.43 ( m, 2H, -$CH_2$), 1.33- 1.30 (m, 4H, -$CH_2$), 0.90- 0.88 (m, 3H, -$CH_3$). HRMS (ESI) m/z: $[M+H]^+$calcd for $C_{18}H_{22}NS$ 284.1473, found 284

**10-hexyl-10H-phenothiazine-3-carbaldehyde (2.2):**[183] To a three-necked flask containing a mixture of $POCl_3$ (1.26 mL, 8.47 mmol) and DMF (3.27 mL, 8.47 mmol) was added dropwise **2.1** (2.0 g, 7.06 mmol) in DMF (50 mL) with dropwise in an ice bath with stirring. After the

addition was completed, the reaction mixture was heated to 90˚C for 12 hours. After cooling, the organic fraction was extracted with $CH_2Cl_2$ and dried using anhydrous sodium sulphate. The crude product obtained after evaporation of the solvent was subjected to silica gel column chromatography. The mixed solvent system of dichloromethane: pet ether (1:1 v/v) was used as an eluent to give titled compound **2.2** as a yellow solid. Yield: 1.17 g (78%). $^1$H NMR (500 MHz, $CDCl_3$) : δ ( in ppm) : 9.78 (s, 1H, -*CHO*), 7.64 (d, 1H, *J* = 1.5 Hz, *phenothiazine-H*), 7.57 (d, 1H, *J* = 1.5 Hz, *phenothiazine-H*), 7.16 (t, 1H, *J* = 7.7 Hz, *phenothiazine-H*), 7.12 (d, 1H, *J* = 7.5 Hz , *phenothiazine-H*), 6.96 (t, 1H, *J*= 7.5 Hz, *phenothiazine-H*), 6.84 (t, 2H, *J*=8.5 Hz, *phenothiazine-H*), 3.88 (t, 2H, *J* = 7.2 Hz, -$CH_2$), 1.83-1.77 (m, 2H, -$CH_2$), 1.46-1.40 (m, 2H,-$CH_2$), 1.31-1.30 (m, 4H,-$CH_2$), 0.87 (t, 3H, *J* = 7.0 Hz, -$CH_3$); ESI-MS m/z: $[M+H]^+$ Calcd for $C_{19}H_{21}NOS$: 311.1344; Found: 312.

**3-bromo-10-hexyl-10*H*-phenothiazine (2.3).**[184] To a solution of **2.1** (3.2 g, 11.30 mmol) in DMF (50 mL) NBS (2.41 g, 13.56 mmol) in DMF (30 mL) was added dropwise for 30 min. The mixture was stirred overnight at room temperature. The reaction mixture was quenched with ice water and extracted with ethyl acetate. The combined organic fractions were washed with brine and dried over $Na_2SO_4$. The solvent was removed under reduced pressure and the residue was used for the next step without any further purification.

**4-(10-hexyl-10H-phenothiazin-3-yl)benzaldehyde (2.4):**[187] To **2.3** (3.00 g, 8.27 mmol) taken in Schlenk flask, 4-formylphenylboronic acid (1.48 g, 9.93 mmol), potassium carbonate (3.31 g, 24.00 mmol), and tetrakis(triphenylphosphane)palladium (0.478g, 0.413 mmol) were added. A mixture of THF (15 mL) and distilled water (5 mL) was degassed and added to the reaction mixture. The reaction mixture was stirred and refluxed for 12 h under nitrogen. The progess of the reaction was monitored using TLC and the consumption of the limiting reagent 2.3 marked the completion of the reaction. The reaction was quenched using ice cold water and the

compound was extracted using DCM. The organic fraction was dried by passing over sodium sulphate and the solvent was evaporated to give the crude product which was subjected to further purification by silica gel column chromatography. The solvent system used to obtain the compound was petroleum ether: chloroform (1:1v/v). The compound **2.4** was obtained (1.5 g, 46.75 %) as an orange viscous liquid. $^1$H NMR (500 MHz, $CDCl_3$): δ (in ppm): 10.02 (s, 1H, -*CHO*), 7.91 (d, *J* = 8 Hz, 2H, *phenyl-H*), 7.69 (d, *J* = 8 Hz, 2H, *phenyl-H*), 7.44- 7.41 (m, 2H, *phenothiazine-H*), 7.18-7.14 (m, 2H, *phenothiazine-H*), 6.93 (t, *J*= 7.7 Hz , 2H, *phenothiazine-H*), 6.88 (d, *J* = 8.5 Hz, 1H, *phenothiazine-H*), 3.87 (t, *J*= 7.2 Hz, 2H, -$CH_2$ ), 1.86- 1.80 (m, 2H, -$CH_2$), 1.46- 1.42 (m, 2H, -$CH_2$), 1.32- 1.30 (m, 4H, -$CH_2$), 0.88-0.82 (m, 3H, -$CH_3$). HRMS (ESI) m/z: $[M+H]^+$ Calcd for $C_{25}H_{25}NOS$: 388.1735; Found: 388.1735.

**4-((10-hexyl-10H-phenothiazin-3-yl)ethynyl)benzaldehyde (2.5) :**To a degassed solution of **2.3** (400.0 mg, 1.10 mmol) in dry $Et_3N$ (30 mL) were successively added $[Pd(PPh_3)_2Cl_2]$ (48.7 mg, 0.063 mmol), $PPh_3$(33.4 mg, 0.3309 mmol), CuI (0.19 mg, 0.209 mmol) and 4-ethynylbenzaldehyde (287.3 mg, 2.20 mmol). The reaction mixture was refluxed under nitrogen until the complete consumption of bromide **2.3** (monitored by TLC). The reaction was quenched using ice cold water. The reaction was quenched using ice cold water and the compound was extracted using DCM. The organic fraction was dried by passing over sodium sulphate and the solvent was evaporated to give the crude product which was subjected to further purification by silica gel column chromatography. The solvent system used to obtain the compound was petroleum ether: chloroform (70:30 v/v). The compound **2.5** was obtained (163 mg, 36%) as orange viscous liquid.$^1$H NMR (500 MHz, $CDCl_3$): δ ( in ppm): 10.00 (s, 1H, -*CHO*), 7.84 (d, 2H, *J* = 8 Hz, *phenyl-H*), 7.62 (d, 2H, *J* = 8 Hz, *phenyl-H*), 7.33-7.31 (m, 1H, *phenothiazine-H*), 7.29-7.27 (m, 1H, *phenothiazine-H*), 7.24-7.22 (m, 1H, *phenothiazine-H*), 7.15 (t, 1H, $J_1$ = 7.5 Hz, $J_2$ = 8.0 Hz, *phenothiazine-H*), 7.11(d, 1H, 7.0 Hz, *phenothiazine-H*),6.93(t, 1H, *J*= 7.7 Hz, *phenothiazine-H*), 6.85(d, 1H, *J* = 8.0Hz, *phenothiazine-H*), 6.80 (d,

1H, *J* = 8.5 Hz, *phenothiazine-H*), 3.83( t, 2H, *J*= 7.2 Hz, -$CH_2$), 1.82-1.75(m, 2H, -$CH_2$), 1.42-1.41 (m, 2H, -$CH_2$), 1.31-1.29 (m, 4H, -$CH_2$), 0.87-0.83 (m, 3H, -$CH_3$). HRMS (ESI) m/z: $[M+H]^+$Calcd for $C_{27}H_{25}NOS$: 412.1657; Found: 412.1734.

**$H_2$-5-(4-methoxycarbonylphenyl)-10,15,20-tris(10-hexyl-10H-phenothiazin-3-yl)porphyrin[$(PTZ)_3$-$H_2$PCOOMe]:** 10-hexyl-10H-phenothiazine-3-carbaldehyde **2.2** (1.5 g, 4.81 mmol), and methyl-4-formyl benzoate (0.26 g, 1.60 mmol), was dissolved in propionic acid (48 mL) and nitrobenzene (8 mL) and the mixture was heated to reflux. Then a solution of pyrrole (0.465 mL, 6.421 mmol) in nitrobenzene (3 mL) was added dropwise slowly. The system was kept to reflux for another 8 hours till both the aldehyde get consumed. After the solvents were removed under reduced pressure,(vacuum distillation at 90°C, then 120°C, 140-150°C) the residue was dissolved in $CH_2Cl_2$ (40 mL) and then poured into 10 mL $NH_3$ solution and stirred overnight. The organic phase was washed with distilled water and dried with anhydrous sodium sulphate (extracted using chloroform), the solvent was removed and the residue was washed with petroleum ether, to remove the traces of nitrobenzene. The residue was dried by applying vacuum. Compound was purified by column chromatography (silica gel) using $CHCl_3$/petroleum ether 1:1 v/v as eluent. Evaporation of the solvent yielded the purple coloured solid. Yield: 135 mg, 6.6%. $^1$H NMR (500 MHz, $CDCl_3$): $\delta$ (ppm) 8.92-8.75 (m, 8H, β-pyrrole-H), 8.43 (d, 2H, *meso-o*-carbomethoxyphenyl-H, *J* = 8 Hz), 8.29 (d, 2H, *meso-m*-carbomethoxyphenyl-H, *J* = 7.5 Hz), 7.97-7.94 (m, 6H, phenothiazine-H), 7.29- 7.28 (m, 3H, phenothiazine-H), 7.23-7.20 (m, 6H, phenothiazine-H), 7.05 - 7.00 (m, 6H, phenothiazine- H), 4.11-4.08 (m, 9H, -$CH_2$-H and -COOMe-H), 2.08-2.02 (m, 6H, -$CH_2$-H), 1.64 - 1.58 ( m, 6H, -$CH_2$-H),1.46-1.39 (m, 12 H, -$CH_2$-H), 0.97-0.94 (m, 9H, -$CH_3$-H), (t, 9H, -$CH_3$-H, 7.2 Hz), -2.77 (s, 2H, -NH proton). HRMS (ESI) m/z: $[M+H]^+$calcd for $C_{82}H_{78}N_7O_2S_3$ 1288.5379, found 1288.5369

**$H_2$-5-(4-methoxycarbonylphenyl)-10,15,20-tris(10-hexyl-10H-phenothiazin-3-yl)phenyl porphyrin (PTZ-Ph)$_3$-$H_2$PCOOMe :** 4(10-hexyl-10H-phenothiazin-3-yl)benzaldehyde **2.4** (1.8 g, 4.64 mmol), and methyl-4-formyl benzoate (0.25 g, 1.54 mmol), was dissolved in propionic acid (46.90 mL) and nitrobenzene (7.74 mL) and the mixture was heated to reflux. Then a solution of pyrrole (0.45 mL, 6.19 mmol) in nitrobenzene (5 mL) was added dropwise slowly. The system was kept to reflux for another 8 hours till both the aldehyde get consumed. After the solvents were removed under reduced pressure,(vacuum distillation at 90°C, then 120°C, 140-150°C) the residue was dissolved in $CH_2Cl_2$ (40 mL) and then poured into 10 mL $NH_3$ solution and stirred overnight. The organic phase was washed with distilled water and dried with anhydrous sodium sulphate (extracted using chloroform), the solvent was removed and the residue was washed with petroleum ether, to remove the traces of nitrobenzene. The residue was dried by applying vacuum. Compound was purified by column chromatography (silica gel) using $CHCl_3$/petroleum ether 90:10 v/v as eluent. Evaporation of the solvent yielded the purple coloured solid. Yield: 150 mg (6.5%). $^1$H NMR (500 MHz, $CDCl_3$): $\delta$ (ppm) 8.94-8.80 (m, 8H, β-pyrrole-H), 8.45 (d, 2H, *meso-o*-carbomethoxyphenyl-H, $J$ = 8 Hz), 8.32 (d, 2H, *meso-m*-carbomethoxyphenyl-H, $J$ = 8.0 Hz), 8.25-8.23 (m, 6H, phenyl H), 7.90 (d, 6H, $J$ = 7.2 Hz, phenyl H), 7.70-7.69 (m, 6H, phenothiazine-H), 7.21- 7.18 (m, 6H, phenothiazine-H), 7.04-7.02 (m, 3H, phenothiazine-H), 6.97 – 6.92 (m, 6H, phenothiazine- H), 4.11 (s, 3H,-COOMe-H), 3.94 (t, 6H, $J$ = 7.0 Hz), 1.93- 1.87 (m, 6H, -$CH_2$-H ), 1.52-1.49 (m, 6H, -$CH_2$-H), 1.38 – 1.35 ( m, 12H, -$CH_2$-H), 0.93-0.89 (m, 9H, -$CH_3$-H), -2.71 (s, 2H, -NH proton). HRMS (ESI) m/z: $[M+H]^+$calcd for $C_{82}H_{78}N_7O_2S_3$ 1288.5379, found 1288.5369

**$H_2$-5-(4-methoxycarbonylphenyl)-10,15,20-tris(10-hexyl-10H-phenothiazin-3-yl)phenyl acetylene porphyrin (PTZ-PhAc)-$H_2$PCOOMe:** 4(10-hexyl-10H-phenothiazin-3-yl)benzaldehyde **2.5** (1.65g, 4.00 mmol), and methyl-4-formyl benzoate (0.22 g, 1.33 mmol), was dissolved in propionic acid (40 mL) and nitrobenzene (6 mL) and the mixture was heated

to reflux. Then a solution of pyrrole (0.38 mL, 5.34 mmol) in nitrobenzene (2 mL) was added dropwise slowly. The system was kept to reflux for another 10 hours till both the aldehyde get consumed. After the solvents were removed under reduced pressure,(vacuum distillation at 90°C, then 120°C, 140-150°C) the residue was dissolved in $CH_2Cl_2$ (40 mL) and then poured into 10 mL $NH_3$ solution and stirred overnight. The organic phase was washed with distilled water and dried with anhydrous sodium sulphate (extracted using chloroform), the solvent was removed and the residue was washed with petroleum ether, to remove the traces of nitrobenzene. The residue was dried by applying vacuum. Compound was purified by column chromatography (silica gel) using $CHCl_3$/petroleum ether 80:20 v/v as eluent. Evaporation of the solvent yielded the purple coloured solid. Yield: 115 mg (5.4%).$^1$H NMR (500 MHz, $CDCl_3$): $\delta$ (ppm) 8.88-8.80 (m, 8H, β-pyrrole-H),8.44 (d, 2H, *meso-o*-carbomethoxyphenyl-H, $J$ = 8 Hz), 8.30 (d, 2H, *meso-m*-carbomethoxyphenyl-H, $J$ = 8.0 Hz), 8.18 (d, 6H, phenyl H, $J$ = 8 Hz), 7.89 (d, 6H, $J$ = 7.7 Hz, phenyl H),7.46-7.43 (m, 6H, phenothiazine-H), 7.19- 7.15 (m, 6H, phenothiazine-H), 6.95 (t, 3H, phenothiazine-H, $J$ = 7.4 Hz), 6.88 (t, 6H, phenothiazine- H, $J$ = 8.5 Hz), 4.11 (s, 3H,-COOMe-H), 3.88 (t, 6H, $J$ = 7.2Hz, -$CH_2$-H), 1.87-1.81 (m, 6H, -$CH_2$-H ), 1.55-1.34 (m, 6H, -$CH_2$-H), 1.33 – 1.31 ( m, 12H, -$CH_2$-H), 0.91-0.89 (m, 9H, -$CH_3$-H), -2.79 (s, 2H, -NH proton). HRMS (ESI) m/z: $[M+H]^+$calcd for $C_{106}H_{90}N_7O_2S_3$ 1588.6318, found 1588.6312

***General procedure for synthesis of $A_3B$ monoacid porphyrin:***

(0.05 mmol of ester porphyrin was dissolved in 30 mL of THF and subjected to base hydrolysis in the presence of a base KOH (5 mmol) in 5mL of water. The reaction mixture was refluxed at 80°C for 24 hours. After completion of the ester, the reaction mixture was cooled to room temperature. Aqueous 1M HCl (10 mL) was added to the reaction mixture. The reaction mixture was washed with aqueous saturated solution of $NaHCO_3$ (50 mL) and then dried over

$Na_2SO_4$. The solvent was removed under vacuum and the resultant was subjected to silica gel column chromatography and separated using Chloroform : EtOAc 95:5. V/V as eluent.

**$H_2$-5-(4-Carboxyphenyl)-10,15,20-tris(10-hexyl-10H-phenothiazin-3-yl) porphyrin (PTZ)$_3$-$H_2$PCOOH (2.7):** Yield : 85%. $^1$HNMR (500 MHz, $CDCl_3$): $\delta$ (ppm) 8.95- 8.78 (m, 8H, β-pyrrole-H), 8.53 (d, 2H, *meso-o*-carboxyphenyl-H, *J* = 7.2 Hz), 8.35 (d, 2H, *meso-m*-carboxyphenyl-H, *J* = 7.4 Hz), 7.98-7.95 (m, 6H,phenothiazine-H), 7.29-7.28 (m, 3H, phenothiazine-H), 7.24-7.21 (m, 6H, phenothiazine-H), 7.06-7.00 (m, 6H, phenothiazine-H), 4.10 (t, 6H, -$CH_2$-H), 2.09-2.03 (m, 6H, -$CH_2$-H),1.64-1.58 (m, 6H, -$CH_2$-H), 1.44-1.40 (m, 12H, -$CH_2$-H),0.97-0.94 (m, 9H, -$CH_3$-H), -2.74 (s, 2H, -NH proton). HRMS (ESI) m/z: $[M+H]^+$calcd for $C_{81}H_{76}N_7O_2S_3$ 1274.5223, found 1274.82

**$H_2$-5-(4-Carboxyphenyl)-10,15,20-tris(10-hexyl-10H-phenothiazin-3-yl) phenyl acetylene porphyrin (PTZ-PhAc)$_3$-$H_2$PCOOH (2.11):**Yield: 80%$^1$H NMR (500 MHz, $CDCl_3$): $\delta$ (ppm) 8.89-8.83 (m, 8H, β-pyrrole-H), 8.52 (m, 2H, *meso-o*-carboxyphenyl-H), 8.36-8.34(m, 2H, *meso-m*-carboxyphenyl-H), 8.20- 8.18 (m, 6H, phenyl H), 7.90 (d, 6H, *J*= 7.2 Hz, phenyl H),7.46-7.43 (m, 6H, phenothiazine-H), 7.19-7.13 (m, 6H, phenothiazine-H), 6.95 (t, 3H, phenothiazine-H, *J* = 7.4 Hz), 6.88 (t, 6H, phenothiazine- H, *J* = 8.5 Hz), 3.90-3.87 (m, 6H, -$CH_2$-H), 1.87- 1.83 (m, 6H, -$CH_2$-H ), 1.47-1.43 (m, 6H, -$CH_2$-H), 1.34 – 1.32 ( m, 12H, -$CH_2$-H), 0.91-0.90 (m, 9H, -$CH_3$-H), -2.77 (s, 2H, -NH proton).

***General Procedure for the Synthesis of Zn Insertion***

(0.05 mmol of free base acid porphyrin was dissolved in chloroform, 10 equivalents of zinc acetate ($Zn(CH_3COO)_2.2H_2O$) (0.5 mmol) in methanol was added to it and the reaction mixture was refluxed for 2 hours. The reaction mixture was cooled to room temperature, washed with water and dried over $Na_2SO_4$. The solvent was removed under vacuum. The resultant was

subjected to silica gel column chromatography and the desired product was eluted using Chloroform:EtOAc 90:10.v/v. The compound was recrystallized using chloroform and methanol.

**5-(4-Carboxyphenyl)-10,15,20-tris(10-hexyl-10H-phenothiazin-3-yl) porphyrinato zinc (II) (PTZ)$_3$-ZnPCOOH (2.8):**Yield: 90%, $^1$H NMR (500 MHz, $CDCl_3$): $\delta$ (ppm) 8.90-8.74 (m, 8H, β-pyrrole-H), 8.64-8.51 (m, 2H, *meso-o*-carboxyphenyl-H), 8.30 - 8.24 (m, 2H, *meso-m*-carboxyphenyl-H), 7.93-7.72 (m, 6H, phenothiazine-H), 7.16-6.89 (m, 15H, phenothiazine-H) , 4.06- 3.90 (m, 6H, -$CH_2$-H),2.00-1.94 (m, 6H, $CH_2$-H), 1.63-1.57 (m, 6H, $CH_2$-H), 1.38-1.32 (m, 12 H, $CH_2$-H), 0.91-0.90 (m, 9H ,-$CH_3$-H). HRMS (ESI) m/z: $[M+H]^+$calcd for $C_{81}H_{74}N_7O_2S_3Zn$ 1336.4358, found 1337.4272.

**5-(4-Carboxyphenyl)-10,15,20-tris(10-hexyl-10H-phenothiazin-3-yl) phenyl porphyrinato zinc (II)**: **(PTZ-Ph)$_3$-ZnPCOOH (2.10):** Yield: 85%,$^1$H NMR (500 MHz, $CDCl_3$): $\delta$ (ppm) 9.00-8.87 (m, 8H, β-pyrrole-H), 8.43- 8.41- (m, 2H, *meso-o*-carboxyphenyl-H), 8.31- 8.30 (m, 2H, *meso-m*-carboxyphenyl-H), 8.24 -8.23 (m, 6H, phenyl H), 7.89- 7.88 (m, 6H, phenyl H),7.68 - 7.66 (m, 6H, phenothiazine-H), 7.19-7.14 (m, 6H, phenothiazine-H), 6.98-6.90 (m, 9H, phenothiazine-H), 3.92-3.90 (m, 6H, -$CH_2$-H), 1.89-1.87 (m, 6H, -$CH_2$-H ), 1.50-1.48 (m, 6H, -$CH_2$-H), 1.34–1.30 ( m, 12H, -$CH_2$-H), 0.92-0.90 (m, 9H, -$CH_3$-H). HRMS (ESI) m/z: $[M+H]^+$calcd for $C_{99}H_{86}N_7O_2S_3Zn$ 1564.5297, found 1564.5295.

**5-(4-Carboxyphenyl)-10,15,20-tris(10-hexyl-10H-phenothiazin-3-yl)phenyl acetylene porphyrinato zinc (II)(PTZ-PhAc)$_3$-ZnPCOOH (2.12)**: Yield: 80%, $^1$H NMR (500 MHz, $CDCl_3$): $\delta$ (ppm) 8.80-8.74 (m, 8H, β-pyrrole-H), 8.38-8.36 (m, 2H, *meso-o*-carboxyphenyl-H), 8.16-8.14 (m, 2H, *meso-m*-carboxyphenyl-H), 8.09-8.05 (m, 6H, phenyl H), 7.78-7.77 (m, 6H, phenyl H), 7.34-7.31 (m, 3H, phenothiazine-H), 7.08- 7.04 (m, 6H, phenothiazine-H), 6.84-6.83 (m, 3H, phenothiazine-H), 6.81-6.79 (m, 6H, phenothiazine- H), 3.80-3.78 (m, 6H,

-$CH_2$-H), 1.75-1.73 (m, 6H, -$CH_2$-H ), 1.49-1.47 (m, 6H, -$CH_2$-H), 1.35 – 1.30 (m, 12H, -$CH_2$-H), 0.89-0.86 (m, 9H, -$CH_3$-H). HRMS (ESI) m/z: $[M+H]^+$calcd for $C_{105}H_{85}N_7O_2S_3Zn$ 1636.5297, found 1637.5256.

**Table 2.1:** Summary of synthetic details for free base porphyrin esters.

| Porphyrin Compound | Pyrrole (mL) | Methyl 4-formyl benzoate (gm) | Aldehyde (gm) | Reaction Time (hr) | Yield (%) |
|---|---|---|---|---|---|
| **$(PTZ)_3$-$H_2PCOOMe$** | 0.46 | 0.26 | 1.5 | 6 | 6.6 |
| **$(PTZ\text{-}Ph)_3$-$H_2PCOOMe$** | 0.45 | 0.25 | 1.8 | 5 | 6.5 |
| **$(PTZ\text{-}PhAc)_3$-$H_2PCOOMe$** | 0.38 | 0.22 | 1.65 | 8 | 5.4 |

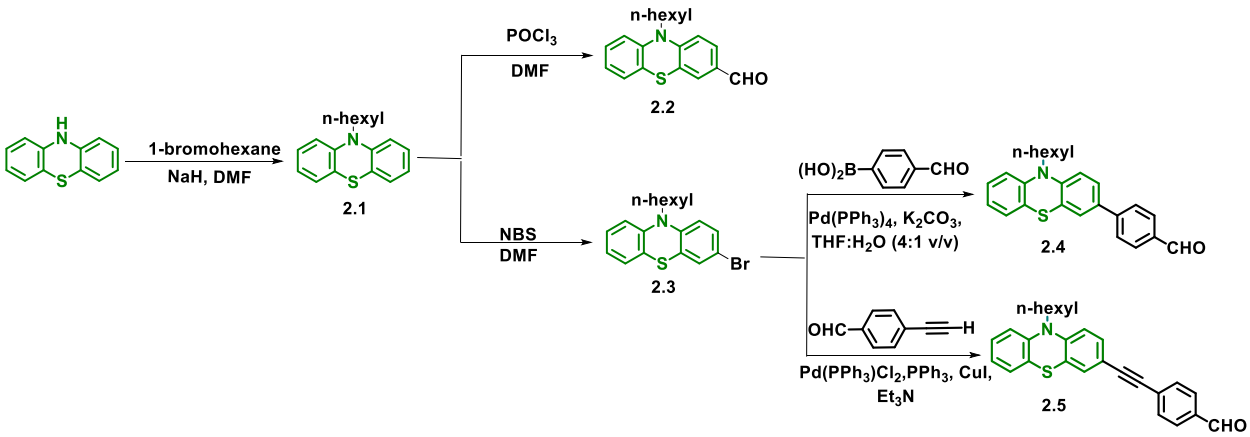


**Scheme 2.1**: Synthetic scheme for the aldehyde precursors.

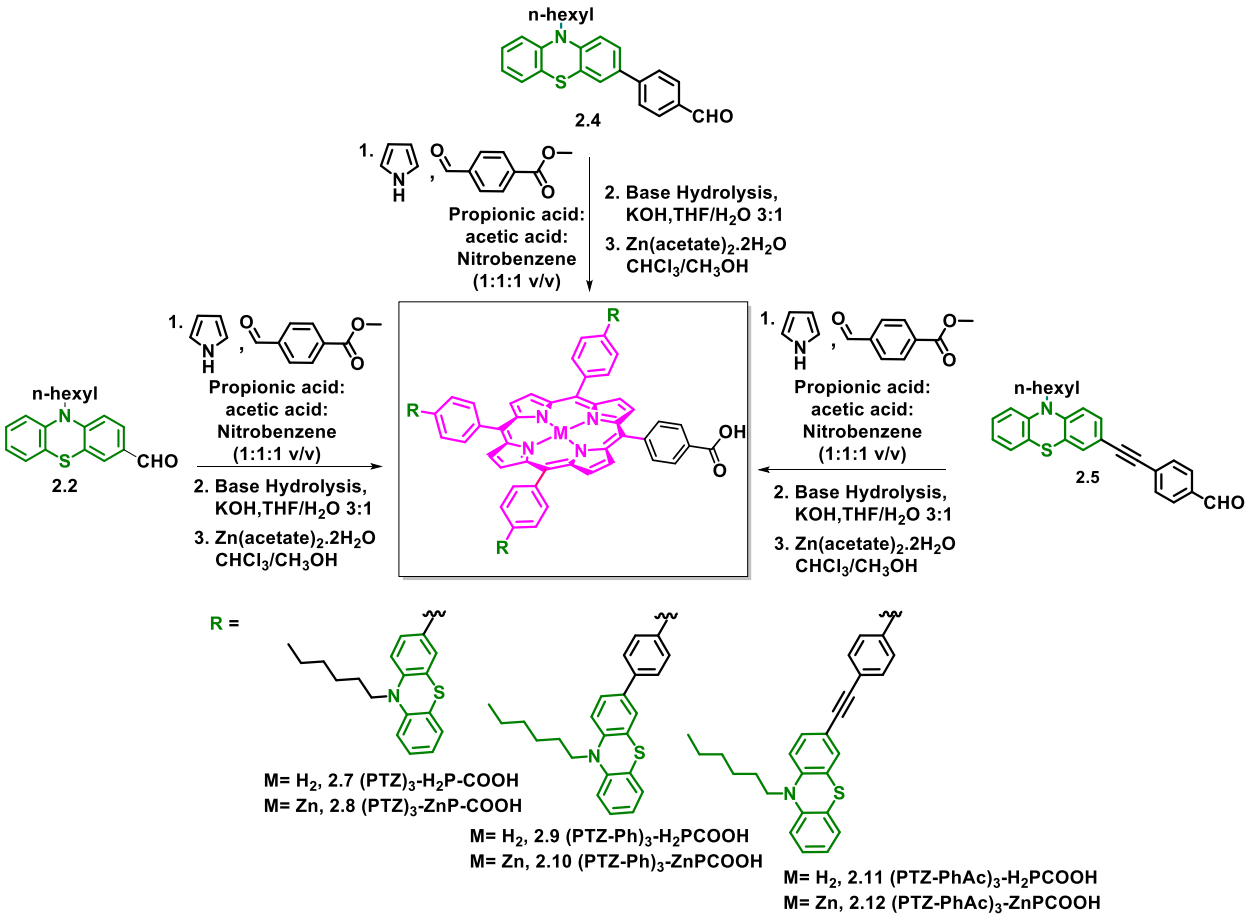


**Scheme 2.2**: Synthetic scheme for phenothiazine porphyrin compounds .

## 2.6 Steady state spectroscopic measurements

### 2.6.1 Absorption

Ultraviolet-visible (UV-VIS) absorption spectra of all the samples in solution phase are measured using JASCO V-530 instrument having a fixed band pass of 2 nm. A baseline correction with the solvent is done before taking the absorption spectra of the material. This is done to remove the absorbance effects that are not from the sample of interest. The wavelength range of the instrument is between 190 nm- 1100 nm. The Deuterium lamp is used for UV

range 190-350 nm and halogen lamp is used for visible region 330-1100 nm. Silicon photo diode is used as the detector.

UV-VIS spectrophotometer measures the absorbance of the sample by measuring the intensity of the light (transmittance or reflectance) before and after the sample at different wavelengths. Intensity of the light decreases after passing through it due to absorbance by the sample. At a fixed path length of the sample (l), absorbance of the transparent sample solution depends on its concentration. The absorbance of the sample is given by Beer-Lamberts law (Equation 2.1)

$$A = \log_{10}(I_0/I) = \varepsilon.c.l \qquad (2.1)$$

Where A is the measured absorbance, I is the intensity of the light after passing through the sample, $I_0$ is the incident intensity of the light at that particular wavelength. C is the concentration of the sample, “l” is the path length and "$\varepsilon$" is the molar absorptivity constant of the sample which is the intrinsic property. The absorption efficiency of the sample depends on the wavelength of incident electromagnetic radiation. Wavelength dependence of "$\varepsilon$" and absorbance (A) is known as absorption spectrum. A schematic is given in the following Figure 2.1

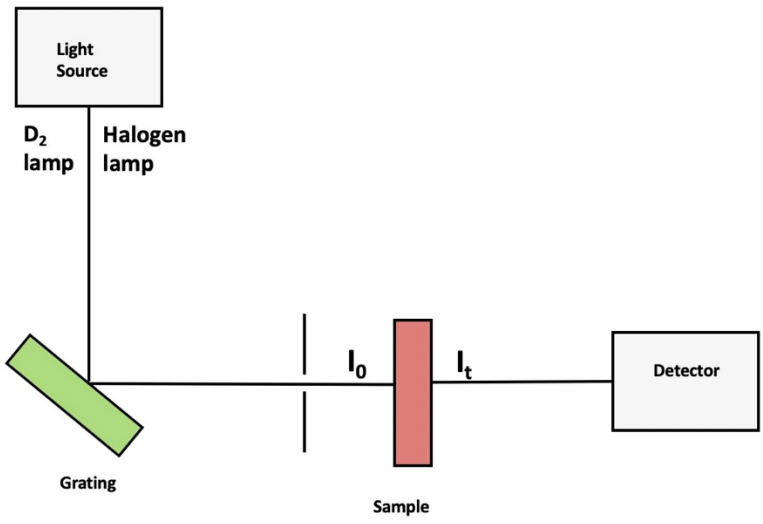


Figure 2.1. Schematic layout of UV-VIS absorption spectrophotometer

### 2.6.2 Spectrofluorimeter

Fluorescence of the sample is measured using spectrofluorimeter. Spectrofluorimeter consists of a light source, photodetector, two monochromators (one for excitation and one for emission). Monochromator is a mechano-optic device that selects a narrow band of wavelengths from a wide range of wavelengths. A monochromator contains an entrance and exit slit, dispersion medium (prism) or diffraction medium (grating). The excitation monochromator selectively passes the narrow band of wavelength to excite the sample. The fluorescence from the sample reaches the detector via emission monochromator. To record the photoluminescence of the sample the excitation monochromator is constant while emission monochromator rotates to collect the different wavelengths to pass. This way intensity of the different emission wavelengths can be collected and emission spectra of the sample is recorded. The emission is collected at ninety degrees from the sample to minimize any transmitted or reflected excitation wavelength. A simple schematic of the spectrofluorimeter is shown in the Figure 2.2

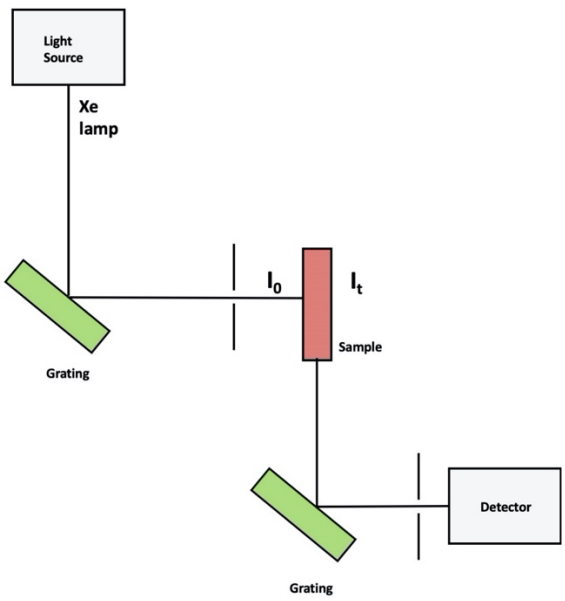


Figure 2.2. Schematic layout of spectrofluorimeter

Ratio of number of photons emitted by the sample to the number of photons absorbed gives the fluorescence quantum yield (QY,$\emptyset_f$) of the sample. QY is calculated with respect to a standard sample (reference sample) with known quantum yield keeping excitation wavelength same for sample and reference. QY of the sample is calculated using following Equation 2.2.

$$\emptyset_f^{sample} = \emptyset_f^{ref} . \frac{\left(\frac{F_{sample}}{1-10^{-A_{sample}}}\right)}{\left(\frac{F_{ref}}{1-10^{-A_{ref}}}\right)} . \left(\frac{\eta_{sample}}{\eta_{ref}}\right)^2 \qquad (2.2)$$

Where, $A_{sample}$ and $A_{ref}$ are the absorbance of the sample at reference at excitation wavelength. $F_{sample}$ and $F_{ref}$ are the integrated emission intensity, $\eta_{sample}$ and $\eta_{ref}$ are the refractive index of the solvent of sample and reference respectively.

In this thesis, fluorescence of the samples are measured using Varian Cary Eclipse Spectrofluorimeter. Band pass of 5 nm is used for both excitation and emission.

## 2.7 Time resolved spectroscopy

### 2.7.1 Time corelated single photon counting

The nanosecond lifetime was measured using a DeltaFlex Time Correlated Single Photon Counting (TCSPC) spectrometer using 420 nm excitation light with full width half maxima (FWHM) of the Instrument Response Function as 80 ps. The excitation light was generated from a tunable Mai-Tai Laser with a repetition rate of 80 MHz which was scaled down to 1/10$^{th}$ i.e. 8 MHz with a pulse picker. A hybrid photomultiplier (HPPD) was used as a detector in the above setup. The decays were collected at magic angle (54.7°) polarization with respect to vertically polarized excitation light to eliminate the effects of rotational anisotropy. The decays were fitted to a sum of exponential functions shown below in Equation 2.3, by iterative reconvolution using Ez Time built in software package.

$$I(t) = \sum_i A_i . \exp\left(-{}^{t}/_{\tau}\right) + B \qquad \text{Eqn. (2.3)}$$

Where $A_i$ and $\tau$ are the lifetime and amplitude of the i$^{th}$ component and also $\sum A_i = 1$. B is the background signal.

#### 2.7.1.1 Working principle

The arrival time of single photon with respect to the reference laser pulse excitation is measured in TCSPC. The laser reference pulse acts as start signal and fluorescence light acts as stop signal. The time difference between start and stop signal is measured. This measurement is repeated millions of times and difference time is stored in the form of histogram. The decay curve of the histogram gives fluorescence lifetime of the sample. It is very important that in TCSPC only single photon is counted per laser pulse excitation event. Multi photon events cause erroneous results ("pulse pile up effect") in histogram statistics.[188] To ensure this, photon counting rate is kept as low as 5 % or lower in comparison to the rate of laser excitation pulse.

#### 2.7.1.2 Instrumentation

The schematic of TCSPC spectrophotometer is shown in Figure 2.3. A laser source of 8 MHz is used to excite the sample. Laser light is split initially into two parts. One part is used as a reference pulse and activates the capacitor called time to amplitude converter (TAC). This is analogous to the stopwatch where start pulse activates the stop watch and fluorescence light acts as a stop signal. The start pulse passes through the vertical polarizer and excites the sample. The emitted photon from sample is again passes through emission polarizer at magic angle of $54.7^0$ with respect to vertical polarisation to eliminate rotational anisotropy. This finally goes through a monochromator and finally to photon counting photo multiplier tube (PMT). The amplified emission signal from PMT acts as a stop signal. The time difference between start and stop signal is stored as a voltage. This voltage is then converted to time by analog to digital convertor. The process where reference starts the TAC and emission stops the TAC is known as "forward" mode operation. However, forward mode has a disadvantage of TAC overuse. In the forward mode, due to inherent low counting rate of the photons, most of the times emission photon does not reach the detector, thereby resulting in overcharging TAC. To overcome this problem "reverse mode" operation is employed. In reverse mode, emission photon acts a "start" signal and reference acts a "stop" signal. The reference signal used in reverse mode is not an optical signal rather electric signal. The time delay between reference and emission signal is adjusted using a delay line.

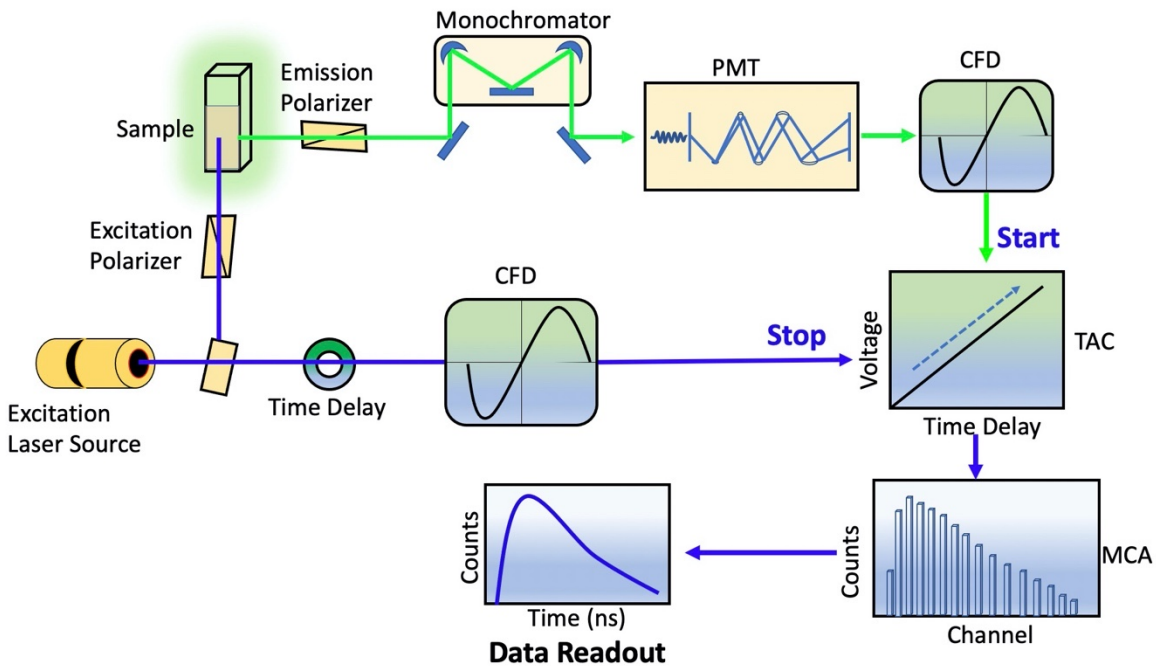


Figure 2.3. Schematic of the TCSPC spectrophotometer.

The arrival time of the signal in TAC is important in TCSPC measurement. To measure the accurate arrival time of start and stop signal, constant fraction discriminator (CFD) is used. The leading edge of the discriminator introduces error due to variation of the signal strength. To overcome this, signal is divided into two parts, one of it is inverted and delayed by certain time. Then, the two signals are added. The resulting signal has a zero crossing point which is independent of signal strength.[189,190]

### 2.7.2 Non-linear optics for Ultrafast spectroscopy

Ultrafast time resolved spectroscopy deals with the study of molecular processes which occurs at sub picosecond timescale. Requirement of short laser pulses with temporal resolution of sub-picosecond to sub-femtosecond is the core of ultrafast spectroscopy. This is realized with the advent of mode locked lasers almost 40 years ago. From then, shortening the laser pulses to attosecond regime now is the state of the art. The generation of such short pulses with different frequencies is based on the principles of non-linear optics.

Linear spectroscopy involves light matter interaction where induced polarization (P) of the matter is directly proportional to the applied electric field (E) of the light source used, $P = \varepsilon_0 \chi E$, This relation fails when we use high intensity laser pulses during ultrafast spectroscopy. Non-linear effects comes into place in such scenario and the resulting polarization is following.

$$P = \varepsilon_0 \chi E + \frac{1}{2}\chi^2 E^2 + \frac{1}{6}\chi^3 E^3 + \cdots (2.3)$$

Here, $\chi^2$ and $\chi^3$ are second and third order nonlinear susceptibility. The typical values of $\chi$ and its higher orders are 1, $10^{-12}$ m/V and $10^{-23}$ $m^2/V^2$ respectively. Materials lacking centre of symmetry shows second order non-linear effects and third order non-linear effect can be shown by any material. Typical examples for second order non-linear crystals are Beta barium borate (β-BBO), lithium triborate (LBO), etc.)

Generation of pump pulses of certain frequency depending on the absorption of the material of interest requires the tuning of the laser output wavelength. Non-linear interaction of laser with the crystals is used to generate pump and probe pulses. The typical non-linear processes used are second harmonic generation (SHG), difference frequency generation (DFG), optical parametric amplification (OPA), non collinear optical parametric amplification (NOPA). Conservation of energy ($\omega$) and momentum (k) has to be followed for the incident and exiting light fields on these non-linear materials.

$$\omega_3 = \omega_1 + \omega_2 \ldots\ldots 2.4$$

$$k_3 = k_1 + k_2 \ldots\ldots\ldots 2.5$$

These two conditions should be met for generation of ultrafast pulses in the non-linear crystals. This can be achieved by phase matching ($\Delta k = 0$) of the incident fields on the bi-refringent non-linear crystal at a certain angle. The simplest frequency conversion process of all is second

harmonic generation, where a single fundamental light is focused on the non-linear crystal to generate the light of double the frequency ($\omega_3 = 2\omega_1$). When two pulses of different frequencies interact with the non-linear crystal with all the phase matching conditions, output field can be of light with frequency corresponding to sum of the frequencies of two incoming radiations ( $\omega_3 = \omega_1 + \omega_2$). This process is typically known as sum frequency generation. With the right orientation and non-linear material, generation of light with frequency corresponding to the difference of the interacting two frequencies (DFG, $\omega_3 = \omega_1 - \omega_2$) can also be achieved. Optical parametric amplification is the process where amplification of the seed pulse (signal pulse) takes place by a pump pulse of higher frequency resulting in reduced intensity of the pump pulse along with the idler pulse of remaining energy which is generated due to conservation of energy.

The most prominent femtosecond laser used in ultrafast spectroscopy is titanium doped sapphire solid state lasers ($Ti^{3+}$: $Al_2O_3$). Typically titanium sapphire crystals produce sub 100 fs laser pulses. The central emission wavelength can be tuned from 600 to more than 1000 nm. This depends on pump source, cavity length and material. The laser pulse repetition rate is governed by the cavity length and its typically in the range of 80 MHz for Ti:Sapphire lasers. Generation of laser pulses in visible region is difficult using solid state lasers due to the complexity involved. The fundamental output of Ti:Sapphire is used to generate pulses of different frequencies using optical parametric amplification process discussed in the previous paragraph. One part of the frequency doubled beam of the fundamental of Ti:Sapphire using BBO crystal is overlapped with the super continuum white light generated in another BBO crystal. Depending on the orientation of the second non-linear crystal, seed pulse is amplified corresponding to the phase matching condition at a particular angle of the crystal. Addition of another non-linear crystal allows us to mix signal and idler beams generate difference frequency pulse signal in the infra-red region.

Interaction of high energy pulses with the transparent materials like sapphire or calcium fluoride, creates a self-phase modulation phenomena which is a third order non-linear response. The high intensity beam changes the refractive index of the medium (optical kerr effect) leading to spectrally broadened output pulse generating white light super continuum (SCG, super continuum generation). White light generated is used to generate seed pulse for OPAs and probe pulse in the transient absorption spectroscopy. The white light generated (spectral, temporal parameters) strongly depends on the initial central wavelength incident on Sapphire or $CaF_2$ . All the non-linear processes discussed is shown in figure 2.4.

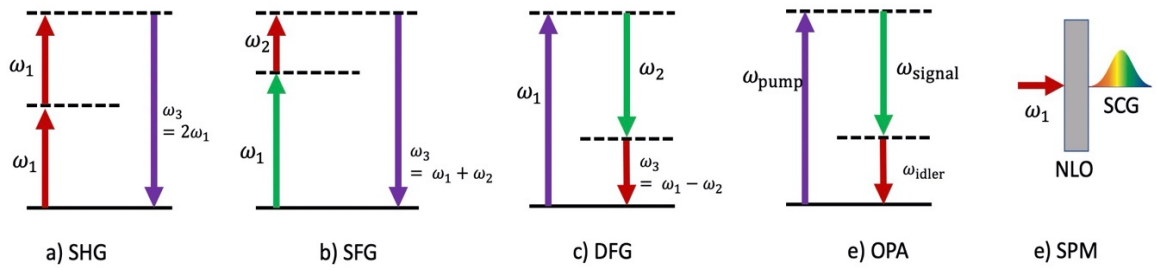


Figure 2.4. Different non-linear process observed with high intensity pulses of femtosecond pulses for different frequency generation a) second harmonic generation (SHG), b) sum frequency generation (SFG) c) difference frequency generation (DFG) d) optical parametric amplification (OPA) and e) self- phase modulation (SPM).

### 2.7.3 Transient absorption spectroscopy

Transient absorption is a technique to study the excited state dynamics of a system. Two ultrafast femtosecond pulses (pump/probe) are incident on the sample with a time delay in between them. Initially, pump pulse is absorbed by the sample and excited state is generated. Within a small time, delay probe pulse is absorbed by the sample which is in excited state. Thus by varying the time delay between pump and probe pulse, we can study the relaxation dynamics of the charge carriers. The change in optical density (ΔOD) of the sample is measured by taking the ratio of intensity of probe light transmitted from the sample in the presence and

absence of pump pulse as shown in Equation 2.6. Here, $I_{pump}$ and $I_{without\ pump}$ are the probe intensity transmitted in the presence and absence of pump pulse on the sample respectively.

$$\Delta OD = -\log (I_{pump}/I_{without\ pump}) \qquad (2.6)$$

There are three main components in transient absorption spectra (Figure 2.5). First, the ground state bleach component. Depopulation of the ground state by the pump pulse results in less ground state absorption of the probe pulse as compared to reference probe pulse where pump is not present. This results in the more transmission of probe light giving negative signal. Second, the excited state absorption. Excited states created by the pump pulse absorb the probe light resulting in less probe light transmitted as compared to sample in absence of pump pulse where there are no excited states to absorb. Thus excited state absorption component gives positive ΔOD. Excited state absorption (ESA) is manifested mainly in the infrared region due to intraband transitions. The positive signal just after the bleach is attributed to bi-exciton related level shifting effects.[150,151,191] Finally, the probe pulse in the excited state ejects the electrons from the excited state resulting in stimulated emission. This leads to more probe pulse getting transmitted giving negative absorption signal.

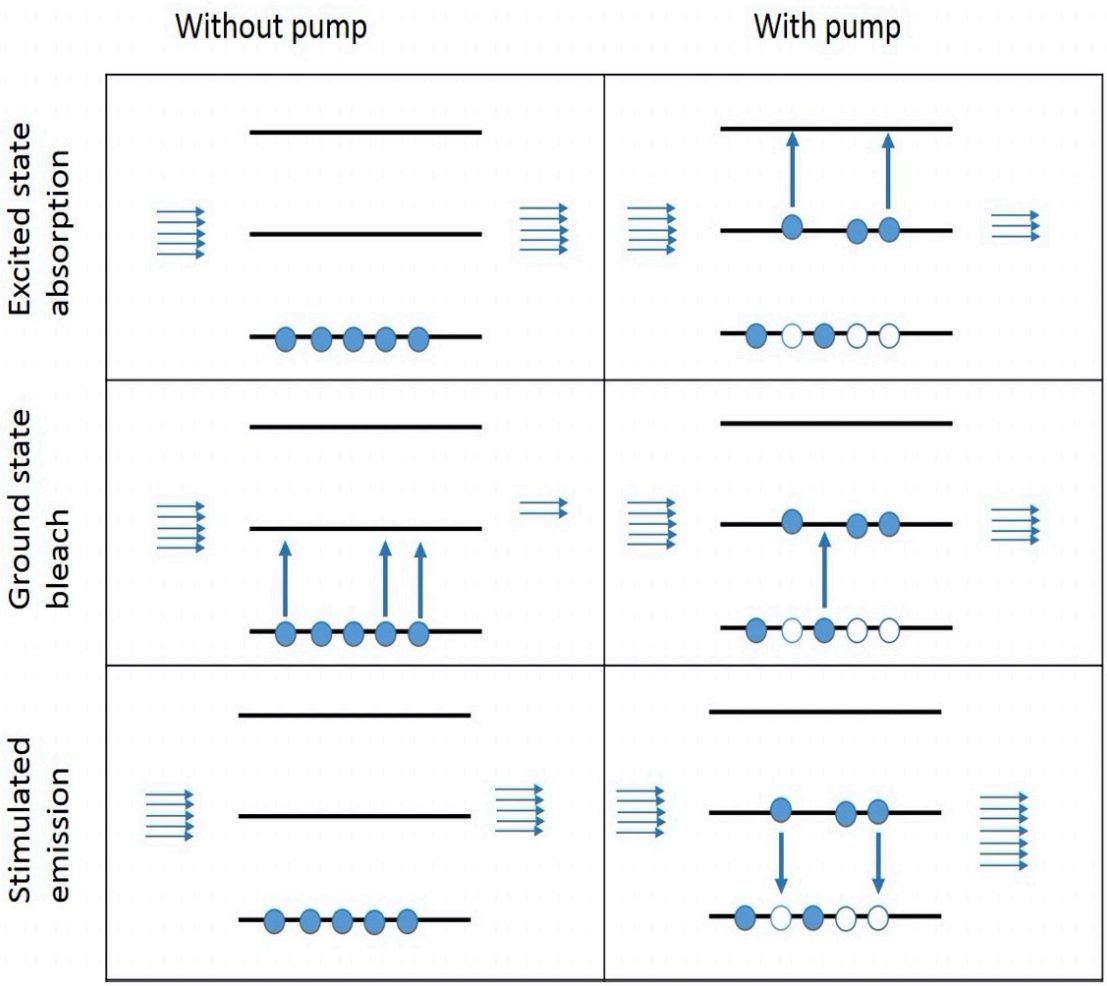


Figure 2.5. Types of signal from pump-probe spectroscopy. Top panel shows excited state absorption giving positive ΔOD. Middle panel shows ground state bleach signal showing negative ΔOD. Bottom panel shows Stimulated emission signal showing negative ΔOD.

The overall transient absorption spectrum is very complex as it consists of all the above three mentioned phenomena occurring simultaneously and it is difficult to distinguish them. The probe pulse is delayed with respect to pump pulse so that ΔOD at different time delays can be plotted. This gives us the dynamics of the excited state as a function of time. We can then fit the kinetic data to understand the timescales of the different phenomena occurring in the materials. Understanding these time scales is very important in optimizing device architecture. Transient absorption can give the rates of cooling, trapping, recombination and charge transfer at hetero junctions of metal-semiconductor interfaces.[149,150,192–194]

#### 2.7.3.1 Instrumentation

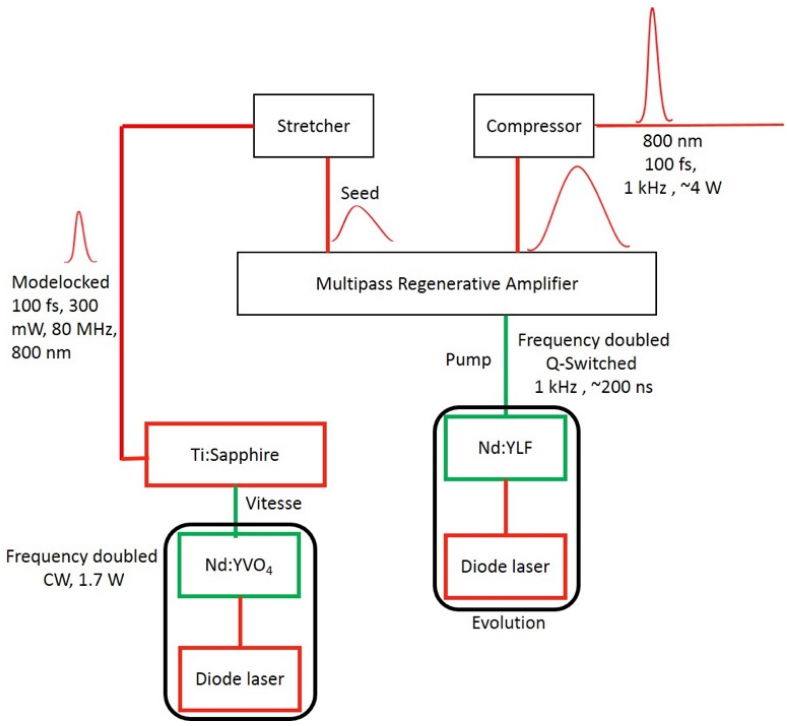


Figure 2.6: Schematic showing the generation of ultrafast femtosecond pulses.

The pump probe setup where pump and probe pulses are generated is by a regenerative amplifier (Libra, Coherent, USA). Generation of femtosecond pulses schematic in Figure 2.6. A 1.7 W output of a second harmonic Nd:$YVO_4$ is used to pump Ti:Sapphire laser to produce mode locked (100 fs, 300 mW, 80 MHz, 800 nm) which acts as a seed pulse for the regenerative amplifier. Before sending it to the amplifier it will be stretched in time to reduce the peak power. In Evolution (Coherent, USA) second harmonic (Q-switched, 1 kHz , ~200 ns) of the Nd:YLF is used as a pump for amplification in regenerative amplifier. After multiple passes in the amplifier when it reaches sufficient power, it is sent to compressor to compress the pulse using grating resulting in generation of 800 nm, 100 fs, 1 kHz , ~4 W ultrafast pulses.

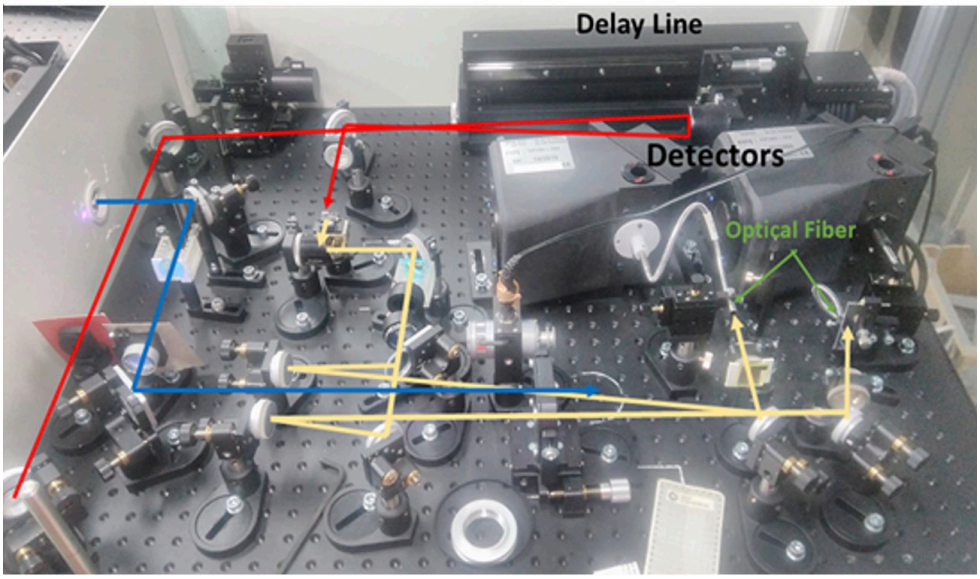


Figure 2.7. Femtosecond transient absorption spectrophotometer setup. Light beam shown in red is the fundamental output of regenerative amplifier used to generate WLC. Blue beam is pump light used and probe light is shown in light yellow color.

The generated pulse is then split into two parts for generating pump and probe pulse. Approximately 1.6W out of 4W is sent to TOPAS (Optical parametric amplifier) to generate desired pump wavelength to excite the sample. The wavelength range of TOPAS is 290-2600 nm, A chopper is used to reduce the repetition rate of pump light to 500 Hz. The residual part is used to generate white probe light (380-780 nm), white light continuum (WLC). $CaF_2$ crystal is rotated continuously to avoid the damage of the crystal. The probe light is further divided into two parts, one as a reference and other one overlaps with the pump light. The reference white light is used to remove shot to shot fluctuations. A magic angle condition is used to eliminate rotational anisotropy during measurements. The variation of pump fluence studies can be performed by using a variable neutral density filter in the path of pump light. The pump and probe light is focused on the rotating sample holder. Using the rotating sample holder minimizes the photodegradation of sample. The transmitted probe and reference light is collected using an optical fibre and sent to a Horiba CP140-104 spectrometer coupled with CMOS detector.

# 3 Enhanced Hot Electron Relaxation Rates in Small Discrete Gold Nanoparticle Assemblies

## 3.1 Introduction

Achieving a fundamental understanding of hot electron relaxation dynamics following excitation of noble metal nanoparticle (MNP) assemblies is essential to enable efficient utilization of harvested electromagnetic energy. Interaction of MNPs with electromagnetic radiation results in the collective oscillation of conduction band electrons across the nanoparticle, known as the localized surface plasmon resonance (LSPR) (refer to 1.1 for the overview of LSPR). Coupled nanoparticles (refer to 1.1) have generated significant interest due to the range of potential applications based on their optical response to incident radiation,[39] including Surface Enhanced Raman Scattering (SERS),[40–42] two-photon absorption (TPA),[43] four-wave mixing,[44,45] solar light harvesting[46,47] and optical switching.[46,48] Many of these applications utilize hot electrons and therefore understanding the hot electron relaxation dynamics in these systems is critical.

Ultrafast transient absorption spectroscopy (UTAS) is one of the most useful techniques in this context. In this technique, high energy ultrafast femtosecond laser pulses generate the free conduction band electrons in MNPs to achieve a non-thermal Fermi-Dirac distribution.[31] A two temperature model is widely used to understand the subsequent ultrafast optical response.[47,49,195] Free electrons, characterized by a small heat capacity, attain high temperatures rapidly upon absorbing energy from the ultrafast laser pulse. They are thermalized by electron-electron scattering in <100 fs. The material lattice, which has a significantly higher heat capacity, remains at a lower temperature in this time period. The consequent temperature gradient drives the transfer of thermal energy from hot electrons to the material lattice, by

electron-phonon relaxation, typically over 1-4 picosecond (ps). Subsequently, energy is lost to the surroundings by phonon-phonon relaxation, usually over few hundreds of picoseconds (50-300 ps). Electron-phonon and phonon-phonon coupling times are conveniently obtained from multiexponential fits to UTAS data, keeping in mind their dependence on laser fluence.[31] The vast body of literature in this field contains differing opinions about the effect of size, shape, ligand and environment of MNPs on hot electron relaxation times. [49,196,31,47,49,55,94,197–200] The widely accepted work of Vallee and Del Fatti explains faster electron-phonon coupling for MNPs with diameters less than 10 nm in the light of spill out of electrons from the material boundary, leading to a decrease in electron density and consequently, in electron screening.[49]

Ultrafast dynamics in MNP aggregates is less explored than in MNP monomers. Femtosecond time-resolved electron diffraction to monitor the nonequilibrium dynamics of spherical gold nanoparticles (GNPs) enables visualization of hot spot regions in dimers using photoelectron emission spectroscopy. [201] High structural homogeneity within dimers is reflected in uniform plasmonic properties at the single particle level. There is no literature report on the effect of plasmon coupling on hot electron relaxation dynamics in small and ordered MNP aggregates. Large, random aggregates of GNPs are known to exhibit faster electron-phonon relaxation than monomers in solution phase.[94] For pump powers of 90 nJ/pulse, electron-phonon coupling times decrease from 1.86 ps in the GNP monomers (diameter of 13 nm) to < 1 ps in their aggregates. Similar enhancements in electron-phonon coupling rates have been observed for thick film assemblies of similarly sized GNPs. Delocalization of hot electrons over the large aggregates results in a greater degree of interfacial scattering, leading to shorter electron phonon relaxation times. In addition, electron phonon coupling is inversely proportional to the electron oscillation phonon resonance detuning (EOPRD). Hot electrons delocalized over larger aggregates decrease EOPRD, resulting in enhanced electron-phonon wave function overlap. [60,94] Little is known about the

effect of plasmon coupling on the phonon-phonon relaxation. While these findings suggest hot electrons are delocalised across multiple nanoparticles in the aggregate, the number of nanoparticles and/or effect of assembly morphology on this delocalization is unknown.

In this chapter, we report hot electron relaxation dynamics in GNP dimers and trimers, prepared by self-assembly using a dithiol linker. Surface modification of MNPs with these linker molecules yields functional assemblies. Such MNP assemblies can also be prepared using DNA linkers,[202–204] but interparticle distances are invariably significantly larger, and the nanoparticles significantly smaller in that case. With dithiol linkers, it is possible to obtain assemblies with small interparticle spacings and consequently, greater plasmon coupling. In the present study, dimers and trimers formed in the solution phase are further purified using gel electrophoresis.[205–207] Understanding the electron relaxation dynamics in these systems can be exploited for optimizing the photochemical reactions and electron transfer reaction between metal semiconductor nanoparticles or molecular adsorbates.[208–211]

## 3.2 Experimental section

Synthesis of gold nanoparticles and assemblies is briefly described in Chapter 2. The structures of gold assemblies are characterized by transmission electron microscopy (TEM) and X-ray diffraction. UV-VIS absorption spectrum was recorded with JASCO V-530 UV/VIS spectrophotometer. Transient absorption spectrum was measured using femtosecond pump probe spectroscopy measurements. Second harmonic of 800 nm fundamental of mode locked Ti: Sapphire laser is used for the excitation of the samples. Pump pulse energy used for the transient absorption studies was 1 μJ/pulse. Probe region is maintained between 440-750 nm. The temporal resolution of the 400 nm excitation experiments were 200 femtoseconds. The path length of the rotating cells (glass) is 1mm. The concentration of all samples was maintained at 0.1 OD. Kinetic traces were obtained in the interval of 1 nm from 420-700 nm

with an integration time of 2 seconds. The assemblies are sensitive to laser light and conditions of a slightly higher pulse energy (compared to previous reports on monomers) with a shorter integration time led to no detectable damage as determined by UV-Visible spectroscopy . Over exposure of the samples to the laser results in disintegration of the assemblies to monomers. Global analysis of the data is performed using principal component analysis in surface minor pro software.[212] Kinetic data obtained were fit to biexponential data to obtain electron-phonon and phonon-phonon coupling times.

## 3.3 Results and discussion

GNP monomers are synthesised according to reported methods with slight modification.[173,175] SEM analysis of the synthesized monomers shows a size distribution of 22 ± 3 nm (shown in appendix Fig. A1). The high degree of monodispersity is crucial to obtain sufficient separation of the dimer and trimer samples assembled from the nanoparticles during purification of these assemblies by electrophoresis. The as-prepared citrate-capped GNPs are ligand exchanged with bis(*p*-sulfonatophenyl) phenylphosphine (BSPP). The formation of GNP assemblies is regulated by optimizing salt and dithiol concentrations in the solution. Alkane dithiols are well known for cross-linking MNPs to form their assemblies in solution, by virtue of the high affinity of sulfur for the gold surface. Dithiols have the added advantage that the degree of nanoparticle assembly in solution can be controlled to some degree by changing linker concentration.[213] At the concentrations used here, a high percentage of the assemblies in solution exist as monomers, dimers and trimers, along with the presence of a small proportion of higher-order structures. The $Na^+$ ion in the salt added to the solution modulates interparticle attraction, allowing the negatively charged nanoparticles to approach each other to a sufficiently close distance, so as to allow binding of the dithiol molecule to two

like-charged particles. At higher salt concentrations, uncontrolled aggregation of the nanoparticles occurs.

Separation of the mixture of assemblies in solution, into dimer and trimer bands, is carried out using gel electrophoresis as shown in Figure 3.1. Monomers move fastest through the pores of the agarose, followed by dimers and then trimers according to the assembly size. The difference in speeds leads to formation of distinct bands of monomers, dimers and trimers.

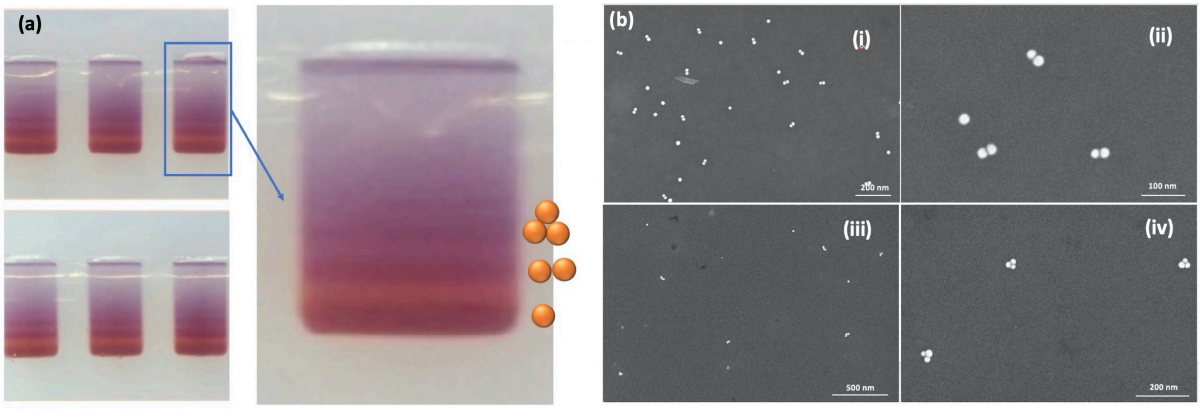


Figure 3.1. (a) Separation of dimers and trimers by gel electrophoresis. Each lane has 90 mM NaCl and 0.1 mM DT. (b) SEM images of gold nanodimers (i, ii) and gold nanotrimers (iii, iv)

The different bands formed in the gel are then cut and separated (Figure 3.1a). Homogeneity in size of GNPs is important to ensure the formation of narrow, well separated bands of monomers, dimers and trimers. In order to collect sufficient sample for spectroscopic measurements, a number of gel lanes across a number of gels are separated, with the samples combined and concentrated following this. The purity of the assemblies following deposition on a substrate (Figure 3.1b) are 65% for dimers and 55% for trimers. For the dimers, the remaining 35% are in the form of monomers while for the trimer band the other structures observed are 25% dimers and 20% of monomers. These values provide a lower limit for the purity of the assemblies, as some decomposition of the assemblies is expected to happen upon

deposition on the substrate, as a result of the strong local forces such as capillary forces, solvent pinning and Van der Waals attraction. As a result, it is most likely that the degrees of purity of dimers and trimers in solution are actually higher than those measured via deposition.[175] For DNA-based self-assembly purified via electrophoresis, samples of dimers have been prepared with purities of > 90%, as indicated by cryogenic TEM.[214] SEM images in Figure 3.1b(iii) show that the trimers formed here are composed of different orientations, including triangular and straight chain morphologies (zoom in views of different orientations of trimers are shown in appendix Fig. A2).

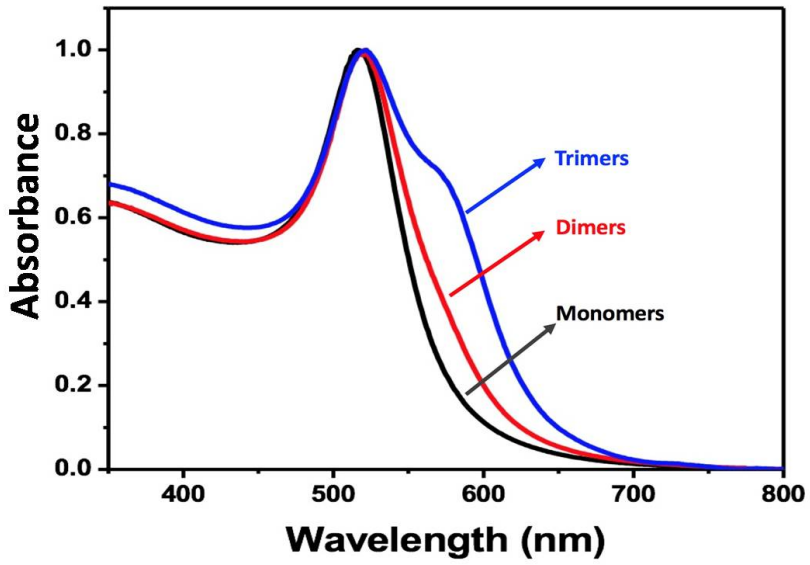


**Figure 3.2**. Normalized extinction spectra of gold nanospheres, dimers and trimers

Extinction spectra of dimers and trimers are dominated by the plasmon band at 515 nm, which is characteristic of the monomer. However, shoulders on the low energy side of the monomer resonance are also observed in these spectra (Figure 3.2), indicating longitudinal coupling between the nanoparticles. This coupling leads to enhancement in the electric field in the interparticle region between these assembled NPs.[215]

To analyse hot electron relaxation dynamics in these assembled dimers and trimers of GNP solutions, transient absorption pump probe spectroscopy is employed. A 200 fs pump pulse

(fwhm) of 1 μJ/pulse at 400 nm is used as an excitation source. Dynamics are probed using white light in the 400-700 nm region.

Transient absorption spectra of gold nanoparticle assemblies display three distinct features for monomers, dimers and trimers (Figure 3.3), which are assigned in accord with the existing model for hot electron relaxation.[31] The positive band in 430-470 nm region is attributed to electronic interband transition, while that in the 570-700 nm region is due to the absorption of thermally excited free electrons, arising from the nonequilibrium electron distribution near the Fermi level according to a two-temperature model.[31] The negative band at 515 nm is attributed to the depletion of the plasmons. The additional negative signal at 580 nm,

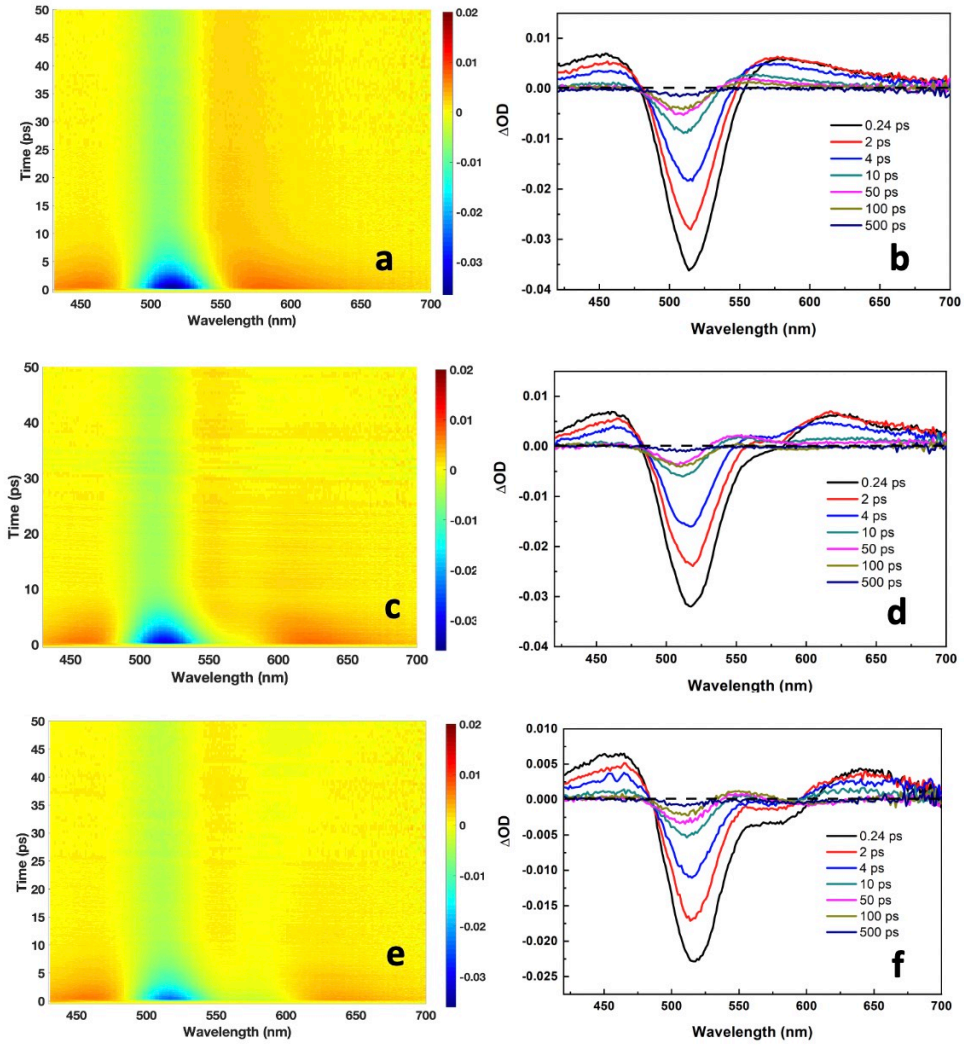


Figure 3.3. Pseudo color heat map (left), corresponding transient absorption spectra at different pump-probe delay (right) of GNP monomers (a,b), dimers (c,d) and trimers (e,f).

observed for dimers and trimers, but not monomers, is due to the bleach of the coupled plasmon longitudinal resonance. Following excitation with the pump pulse, the spectrum crosses the zero line at two points, one on the high energy side (480 nm) and the other at the low energy side (540-600 nm) of the plasmon bleach. The zero crossing point on the high energy side does not shift with the probe delay as observed in Figure 3.3. The zero crossing point on the lower energy side blue shifts with an increase in probe delay in all the three samples. A zero crossing point is observed at 550 nm in the time zero spectrum (spectrum measured just after the excitation at the probe delay of 0.24 ps) of the monomers. Within 10 ps, this point shifts to

530 nm (Figure 3.3 (a, b)). There is no further shift at longer times. Similar trends are observed in the spectra for dimers and trimers. The zero crossing point in the spectrum shifts to 530 nm from 575 nm for dimers and 600 nm for trimers (Figure 3.3 (d, f)). The initial sudden rise in the temperature of the free electrons causes an asymmetric broadening of the spectra. Over time, energy is transferred to the lattice. This narrowing of the bleach signal is due to the cooling of the lattice and has been previously observed in gold momers.[216] In addition, we can clearly see the shift in intraband excitation maxima from 575 nm for monomers to 625 nm for dimers and 650 nm for trimers. Close inspection of the temporal evolution of the transient absorption signals in all the three samples shows a considerable overlap of the surface plasmon bleach signal and intraband absorption signals. It is clear that the transient absorption signal has contributions from plasmon bleach (negative) as well as excited state absorption (positive). The usual approach for analysis of hot electron relaxation, i.e, via TTM, fitting the TA data to a biexponential decay model at a certain probe wavelength, electron-phonon time ($t_1$) and phonon-phonon coupling time ($t_2$) are obtained. we find that the electron–phonon relaxation time ($t_1$) varies with the choice of probe wavelength (Figure 3.4). A sharp dip in the time constants is observed at 490 nm for all the three samples. For longer wavelengths, the relaxation times progressively increase as the wavelength approaches 515 nm (the plasmon maximum) with a factor of two variance in the lifetimes observed across wavelengths to the red of this. The dip in the electron-phonon coupling time is greater for trimers and dimers as compared to monomers in the longitudinal bonding dipolar plasmon region. We interpret these changes in the time constants as a function of wavelength to the overlap of positive and negative signals in the region, *i.e.* the interband and intraband peak regions extend into the major bleach region.

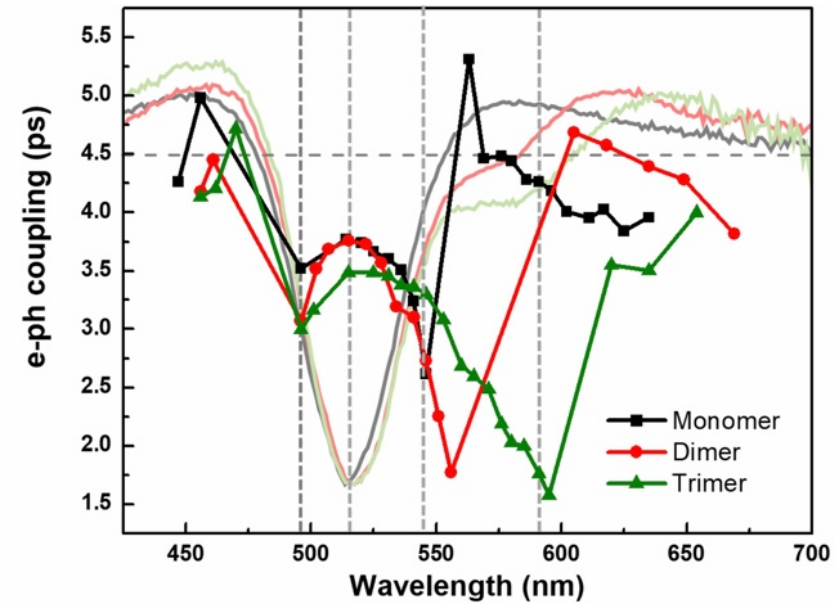


Figure 3.4. Electron-phonon coupling timescales in gold assemblies at different probe wavelengths. Normalized TA spectra of Monomers, Dimers and Trimers at 0.24 ps are shown in a lighter shade for reference. Y-axis depicts the electron-phonon coupling time scales.

Due to the significant overlap of negative plasmon bleach recovery signal and positive inter and intraband signals, conventional analysis of the transient signal at single wavelengths is inadequate to accurately describe the time constants for these systems, with largest errors for the coupled structures. Therefore, the data have been analysed globally using principal component analysis (PCA).[217] Principal components which can describe the entire data with their corresponding eigenvalues, are obtained. For all samples two major principal components (PC1, PC2) are obtained using PCA (Figure 3.5).

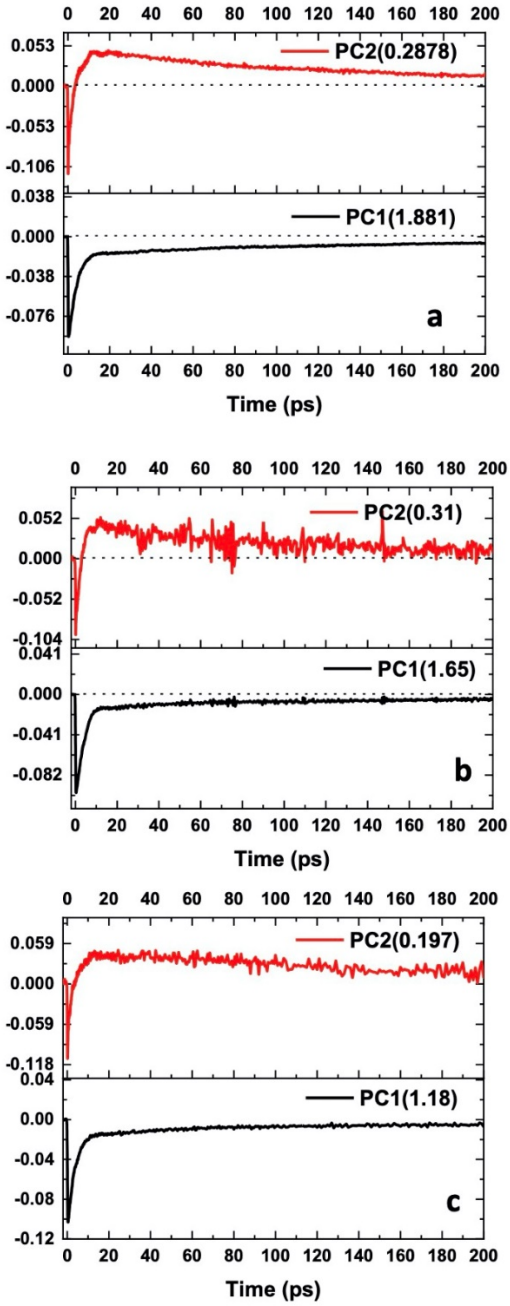


Figure 3.5. Principal component analysis for a) Monomers b) Dimers c) Trimers. Values in the parenthesis shows the eigen values of the corresponding principal component.

Table 3.1. PCA analysis

| Sample | $\tau_{e\text{-}ph}$ (ps) [a] | $\tau_{ph\text{-}ph}$ (ps) [a] |
|---|---|---|
| Monomer | 3.7±0.07 (85.7±7 %) | 203.8±5.8 (14.3±3 %) |
| Dimer | 3.5±0.11 (88.3±5 %) | 179.9±8.1 (11.7±2 %) |
| Trimer | 3.4±0.08 (84.8±6 %) | 127.5±9.6 (15.2±9 %) |

[a]The numbers in parenthesis are amplitudes in percentage. PCA denotes principle component analysis

Their corresponding eigenvalues, showing their percentage significance to the overall signal is shown in parenthesis. PC3 and PC4 in all the samples are extremely noisy and clearly lack structure aside from a sharp peak around time zero, which is the coherent signal due to the overlap of pump and probe pulse. The combined contribution of PC3 and PC4 is less than 10 % compared to PC1 and therefore can be neglected. The two major principal components (PC1 and PC2) are fit to a biexponential decay model and the relaxation times are presented in Table 1. The results of this analysis reveal enhanced electron-phonon and phonon-phonon coupling in dimers and trimers, as compared to monomers. This is reflected in a progressive decrease of electron-phonon relaxation time from 3.7 ps for monomers to 3.4 ps for trimers. Well controlled assemblies of dimer and trimer samples are associated with delocalisation of hot electrons only over one additional nanoparticle (monomer > dimer > trimer), yet a 9 % reduction in electron-phonon relaxation time is measurable. This is in contrast with the 55 % reduction in the electron-phonon relaxation time in uncontrolled random large aggregates,[94] where the larger measured reduction is likely due to the very high degree of aggregation in the sample. Very large scale delocalisation of hot electrons, extending much further than the trimer systems measured here, is observed in these large aggregates.

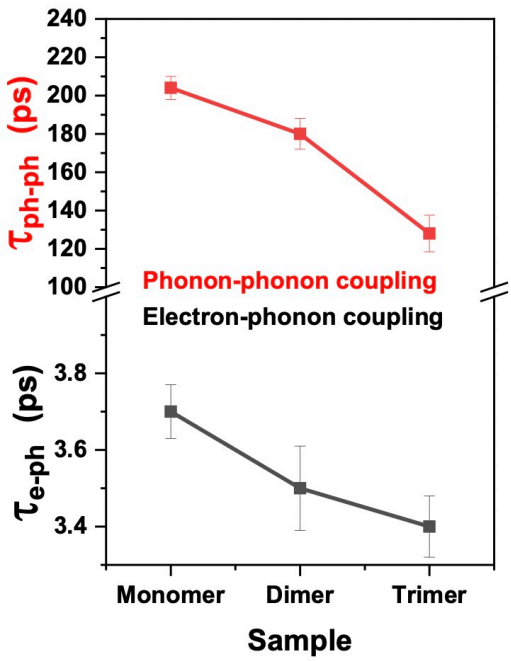


Figure 3.6. Electron-phonon and Phonon-phonon coupling timescales in gold assemblies by PCA analysis.

A progressive and surprisingly larger decrease in the phonon-phonon coupling time is observed, from 203.8 ps for monomers to 179.9 ps for dimers and 127.5 ps for trimers (Figure 3.6). This indicates that in addition to effective electronic coupling, a significant phonon-phonon coupling (wavefunction overlap) occurs in closely spaced pure aggregates. Notably, the dimer sample also contains a proportion of monomers. Similarly, the trimer sample contains a proportion of dimers and monomers. Therefore the determined lifetimes of pure dimers and trimers can be expected to be, if anything, slightly shorter.

Electron-phonon coupling time shows the strength of coupling between the electron oscillation frequency and the phonon modes of a given metal nanoparticle. This is termed as "Electron Oscillation frequency-Phonon Resonance Detuning". Smaller the detuning, stronger the coupling. The effectiveness of electron phonon coupling depends on the overlap of electron oscillation frequency with that of the phonon spectrum.[218] Our results suggest that the coupling

between the closely spaced particles leads to higher spectral overlap between electron oscillation and phonon spectrum thus enhancing the electron phonon coupling rate in dimers and trimers.[60] On the basis of the analysis we conclude that hot electron relaxation time in the assembled particles can be controlled if one can carefully assemble the particles with high precision and obtain a sample with high purity. Single particle hot electron relaxation studies in these systems would further demonstrate the feasibility of such precision plasmonics in optical devices.

### 3.4 Conclusion

In summary, ultrafast transient absorption investigation have been performed on controlled spherical gold nanoassemblies in solution phase using pump-probe spectroscopy. A plasmon coupled band in the extinction spectra of dimers and trimers is observed on the low energy side of the plasmon resonance resulting from longitudinal coupling of nanosphere assemblies. Traditional kinetic fits at the plasmon bleach maximum shows an enhanced electron-phonon coupling rate in trimers. Probing the kinetics at a chosen plasmon coupled maximum is difficult, due to significant overlap of plasmon bleach and excited state intraband excitation signals. This disadvantage has been circumvented by employing global analysis. Hence, it has been established that electron-phonon and phonon-phonon coupling processes in dimers and trimers are faster than those in monomers. This is attributed to greater overlap of electron oscillation and phonon spectra in the regions of enhanced electric field known as hot spots in the assemblies. This shows that hot electron lifetime can be tuned in assembled nanoparticles which could potentially find application as saturable absorbers in optical switches and other optical devices.

# 4 Ultrafast charge separation dynamics of cubic PbS-Au nano heterostructures

## 4.1 Introduction

Semiconductor nanocrystals are of great interest in the past couple of decades in the scientific community for their applications in light emitting diodes, photovoltaic devices, photocatalysis etc.[219–226] The quantum confinement effect in quantum dots makes the excited electron hole pair in a bound state known as "exciton". Photoexcitation of narrow band gap materials with excitation energy much larger than the band gap leads to formation of electron hole pair in higher energy states. The excess energy stored in the exciton is transferred to the electron in the valence band creating an additional exciton pair via coulomb interaction instead of losing excess energy to phonon vibrations. This process is termed as "multiple exciton generation (MEG)".[227–231] The ability of these narrow band gap materials for MEG makes them best candidates for photovoltaic devices. MEG helps to overcome the theoretical Shockley-Queisser limit of these devices and enhances the solar conversion efficiency.[144]

Narrow band gap materials like lead selenide (PbSe) and lead sulphide (PbS) have gained attention in the recent past due to their ability to generate multiple excitons in a single nanocrystal per absorbed high energy photon in ultraviolet and visible region. The broad absorption band up to near IR region from all the way to UV region makes these materials suitable for efficient solar energy conversion. MEG in the lead chalcogenide nanomaterials often lead to a fast non radiative relaxation of charge carriers termed as "Auger recombination". In Auger recombination, the recombination energy of one of the exciton is taken by the charge carrier (electron/hole) pushing them to higher energy level in the respective conduction/valence

band. This process is typically very fast in the range of tens of picoseconds. In order to extract the multiple excitons in these materials, charge carriers needs to be separated before Auger recombination.

Metal-semiconductor hybrid hetero nanostructures offer a possibility to extract the charge carriers very efficiently before Auger recombination process making them one of the best materials for solar energy conversion and photocatalysis.[232–239] Advances in solution processed synthesis of nanocrystals equipped the scientific community to synthesize wide range of heterostructures by carefully controlling the sizes of metal and semiconductors in heterostructures. These structures include metal tips on CdSe and CdS nanorods, gold attached PbS, Au, Pt attached CdSe hybrid particles, Au-PbS core-shell nanoparticles etc. [161,177,240–243] Ultrafast electron relaxation dynamics in these hybrid metal-semiconductor nanostructures are measured using combination of fluorescence upconversion and transient absorption spectroscopy. An ultrafast sub femtosecond (6 fs) electron transfer is observed from CdS nanorods to gold in CdS-Au heterostructure.[235] Ultrafast hot electron transfer as well as band edge electron transfer was observed previously in CdSe-Au systems.[232]

Multiple exciton generation was observed in PbSe and PbS nanoparticles using transient absorption studies.[244] Typically MEG was observed when excitation energies of photon is three to four times the band gap of the material. Gesuele *et al* measured the transient bleach dynamics corresponding to both $1S_e$-$1S_h$ and $1P_e$-$1P_h$ transitions and observed the carrier multiplication from both the states.[245] Ultrafast sub picosecond intraband electron relaxation dynamics and carrier multiplication were observed by El-Ballouli *et al* in PbS nanoparticles.[246] Yang *et al* measured the electron relaxation dynamics in PbS-Au heterostructure.[177] These initial studies did not reveal much of electron transfer dynamics from PbS to Au due to lack of spectral information in IR region where band edge of PbS nanoparticles lies. However typical

timescales they have observed are as follows. A fast 3.5 ps component was attributed to exciton-exciton annihilation post trap state saturation and a slower 29 ps component attributed deep trap state recombination. [177] Later Okuhuta *et al* synthesized PbS-Au heterostructure with varying gold size and studied the electron transfer dynamics from PbS to Au following the 1S bleach dynamics.[247] These studies reveal an ultrafast electron transfer component from the reduction bleach yield. In addition, they have found a slow carrier transfer with time constants ranging from 110 to 1.9 ps with the increase of gold nanoparticle diameter.

In the present chapter, we have synthesized cubic shaped PbS-Au heterostructures and studied the electron transfer dynamics using transient absorption spectroscopy. We analyzed the electron transfer rates and charge relaxation dynamics from 1Se and 1Pe states from excited state absorption dynamics experiments.

## 4.2 Experimental section

Synthesis of PbS and PbS-Au nano heterostructures is briefly described in Chapter 2. The structures of PbS and PbS-Au nanostructures are characterized by transmission electron microscopy (TEM) and X-ray diffraction. UV-VIS absorption spectrum was recorded with JASCO V-530 UV/VIS spectrophotometer. Transient absorption spectrum was measured using femtosecond pump probe spectroscopy measurements. Second harmonic of 800 nm fundamental of mode locked Ti: Sapphire laser was used for the excitation of the samples. Pump fluence used for the transient absorption was 70-300 μJ/cm2. Probe region is maintained between 440-750 nm. The temporal resolution of the 425 nm excitation experiments was 300 femtoseconds.

## 4.3 Results and discussion

TEM images of the synthesized PbS nanoparticles are shown in Figure 4.1a. The average diameter of the synthesized spherical PbS nanoparticles was measured to be around 7 ± 0.5 nm from the Image J ensemble analysis. Figure 4.1b shows the TEM image of the PbS-Au hetero nanostructures. Analysis of the TEM images after Au coating on PbS shows the change in the shape of the particle from spherical to cubic. This suggests the deposition selective growth of Au on cubic phase nanoparticle.[177] The thickness of the gold coating is found to be in the range of 3 nm from the TEM images.

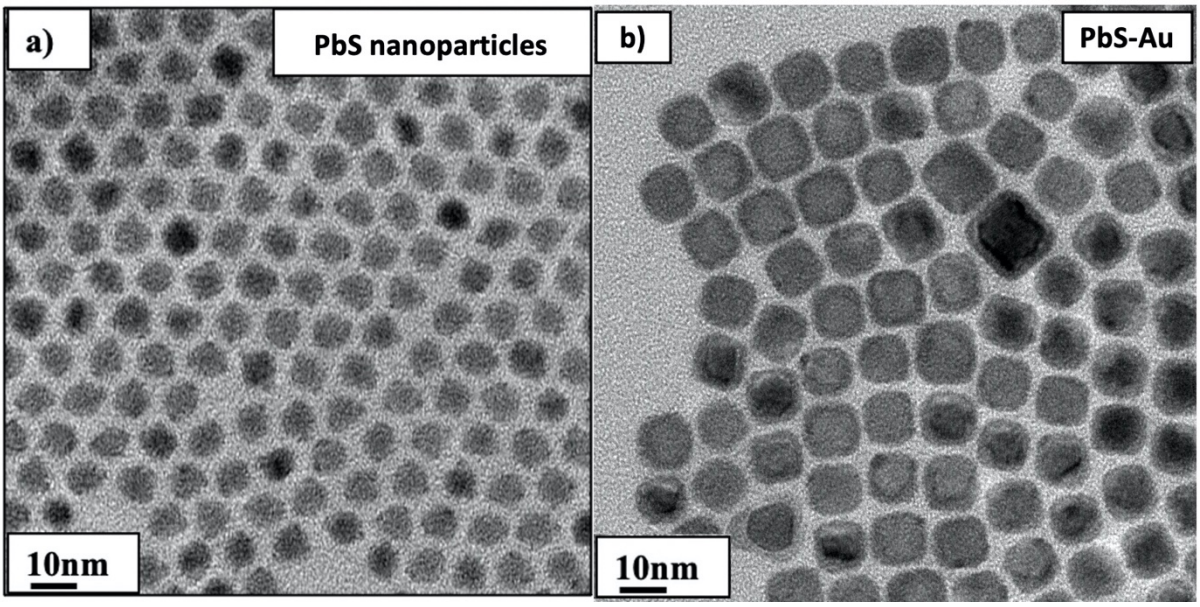


Figure 4.1 a) TEM image of the synthesized PbS nanocrystals b) PbS-Au nano heterostructures.

Steady state absorption spectra of PbS and cubic PbS-Au heterostructure is shown in Figure 4.2. The absorption spectra of PbS shows the broad absorption in the visible to NIR region with a shoulder near 550 nm. However, we could not observe the excitonic peak of PbS quantum dot which usually appears in the 1000-1700 nm based on the size of the nanoparticle. The band gap of the material was obtained from the literature reports where Moreels *et al* systematically investigated the size dependent optical properties of the PbS nanoparticles.[248] Both

experimental and theoretical data match well and the relation of band gap ($E_0$) to the size (d) of the PbS nanoparticle seemed to follow the equation $E_0 = 0.41+(1/(0.0252d^2 + 0.283d))$. From the size range estimated from TEM images, the synthesized 7 nm PbS particles corresponds to the band gap of 0.77eV which is around 1610 nm approximately. The localised surface plasmon peak was not observed for PbS-Au nanostructure in the absorption spectra. This is consistent with the literature where plasmon peak was not observed for the Au coverage less than 2 nm.[20] Stronger coupling of electronic states between metal and semiconductor often lead to broadening of the absorption spectra.[247] No photoluminescence was observed from the samples suggesting very low quantum yield which could be due to high density of deep trap states formed during synthesis.

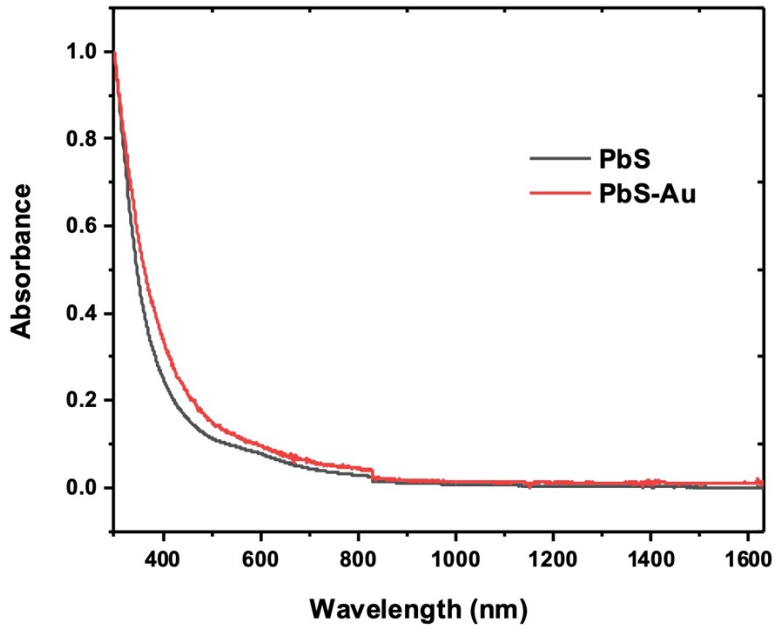


Figure 4.2. Steady state absorption spectra of PbS and PbS-Au hybrid nano heterostructure.

The probe region we relied here is in visible region (430-780 nm) due to unavailability of probe in the IR region. Due to the experimental limitation of our transient absorption spectrometer we could not excite the samples with excitation energy corresponds to band edge which is around 0.77 eV. The excitation energy of 425 nm corresponds to 2.9 eV was used for the

excitation of samples in the present study. The excitation energy employed in the current study is more than three times of the band gap of the material. The transient absorption measurements are performed at very low pump fluence (70-300 μJ/cm$^2$) in order to have less than one exciton per nanocrystal ($N_{abs}$<1) by adjusting the absorbance at excitation wavelength and experimental pump fluence J (photons/cm$^2$) by using the formula $\langle N_{abs} \rangle = J\sigma_a$, $\sigma_a$ is the absorption cross section at excitation wavelength.[248–251] Samples were stirred rigorously using magnetic bead during the experiments to avoid unnecessary multi photon absorption and photobleaching.

Figure 4.3 shows the transient absorption spectra of PbS and cubic PbS-Au hetero nanostructures excited at 425 nm and probed at 430-780 nm region. The spectra clearly shows a positive excited state absorption band with two distinct peaks at 520 nm and 650 nm. The transient absorption spectra of PbS-Au nanoparticles is broadened compared to the two distinct sharp peaks present in PbS nanoparticles. This could be due strong intermixing of the electronic levels at the interface of PbS and Au. It is well documented in the literature that in lead chalcogenide nanoparticles (PbSe, PbS), if the excitation photon energy is larger than the band gap, the excess kinetic energy stored in the exciton transfers its energy to the electron in the valence band creating an additional exciton pair (MEG).[252] The energy threshold for the multiple exciton generation is found to be around three times the band gap by V. Klimov and co-workers.[227] Gesuele *et al* have shown that on exciting the PbS samples with photon energies of $2E_g$ and $4E_g$, electron initially occupies higher energy level in the conduction band, then relaxes to the lower lying electron levels at $1P_e$ and $1S_e$.[245] They have systematically investigated the bleach dynamics of $1S_e$-$1S_h$ and $1P_e$-$1P_h$ transitions and categorically inferred carrier multiplication or multi exciton generation from both the transitions. Many research groups have shown in the past when a quantum dot has more than one exciton, the major relaxation process is governed by Auger recombination process, where the recombination

energy of one exciton is used by the third carrier (electron/hole) that is excited to a higher energy excited state.[227] This process typically happens in a few picoseconds, leaving the nanocrystal with single exciton which then can relax to trap state or via radiative recombination.[155,227,244,245,252,253] With this literature background, we attribute the two peaks at 520 nm and 650 nm in transient absorption spectra to be ESA from $1S_e$ and $1P_e$ levels to higher excited levels.

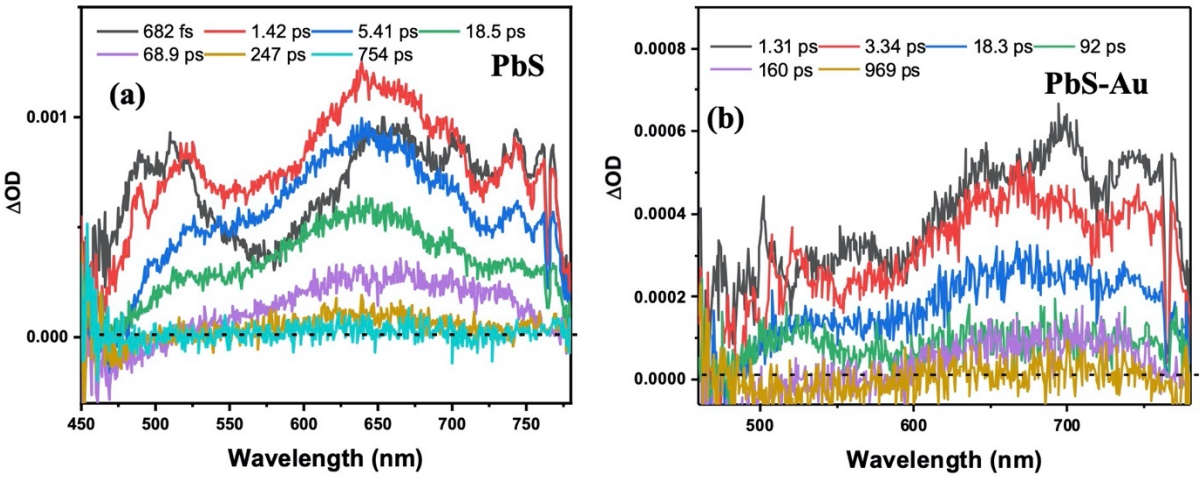


Figure 4.3. (a) Transient absorption spectra at different probe delay of PbS quantum dots and of (b) PbS-Au quantum dots

The carrier relaxation dynamics from both $1S_e$ and $1P_e$ are inferred from the kinetic decay traces at 520 nm and 650 nm for PbS and PbS-Au nanoparticles. Figure 4.5 shows the kinetic fit data of the ESA dynamics of PbS and PbS-Au from the $1S_e$ state on the left panel and from $1P_e$ state on the right panel. The analysis of the rise time for both the transitions reveal instantaneous filling of both $1S_e$ and $1P_e$ from the initially excited electron in the higher level. As discussed earlier, with excitation photon energy greater than 3Eg, the relaxation dynamics is mostly governed by Auger recombination. The excitation energy used in the current study corresponds to 3.7 times the band gap the synthesised PbS particles. The kinetic fit data of the ESA from the $1S_e$ level in PbS nanoparticles (Table 4.1) have shown bi-exponential nature with time scales of 4.4 ps and 56 ps. We attribute the 4.4 ps component to Auger recombination

rate and with the increase in pump fluence from 70-300 μJ/cm$^2$, faster Auger rate has been observed. Considering very low PL and decay of ESA intensity to zero within 300 ps, we attribute the second component of 56 ps to the non-radiative recombination of the charge carriers. However, in the presence of gold the transient decay kinetics of $1S_e$ band is fitted with a fast 0.36 ps component in addition to the other two components of 4.9 ps and 63 ps for lowest pump fluence. We attribute this 0.36 ps component to the fast electron transfer from the $1S_e$ level of conduction band to the gold creating charge separation. This kind of ultrafast charge separation at the junction of the metal-semiconductor interface before Auger recombination and other relaxation channels is very crucial for the development of solar cells where multiple charge carriers created from the MEG can be extracted efficiently leading to overcome Shockley-Queisser limit. The schematic of the dynamics from $1S_e$ level in shown in Figure 4.4.

Table 4.1 Kinetic fitting parameters of the ESA from the $1S_e$ level in PbS and PbS-Au nanoparticles at different pump fluence obtained from transient absorption spectroscopy.

| **Probe** | **Pump fluence (μJ/cm$^2$)** | **Sample** | **$\tau_1$ (ps)** | **$a_1$** | **$\tau_2$ (ps)** | **$a_2$** | **$\tau_3$ (ps)** | **$a_3$** |
|---|---|---|---|---|---|---|---|---|
| 520 nm ESA ($1S_e$) | 70 | PbS | -- | -- | 4.4±0.09 | 0.61±0.06 | 53±11 | 0.39±0.02 |
| | | PbS-Au | 0.36±0.09 | 0.54±0.05 | 4.9±0.07 | 0.10±0.01 | 63±10 | 0.36±0.03 |
| | 150 | PbS | -- | -- | 4.2±0.08 | 0.70±0.07 | 58±12 | 0.3±0.02 |
| | | PbS-Au | 0.42±0.08 | 0.42±0.04 | 5.1±0.09 | 0.23±0.03 | 67±11 | 0.35±0.04 |
| | 300 | PbS | -- | -- | 3.5±0.07 | 0.65±0.06 | 37±9 | 0.35±0.04 |
| | | PbS-Au | 0.42±0.07 | 0.65±0.06 | 4.4±0.07 | 0.09±0.02 | 43±6 | 0.22±0.02 |

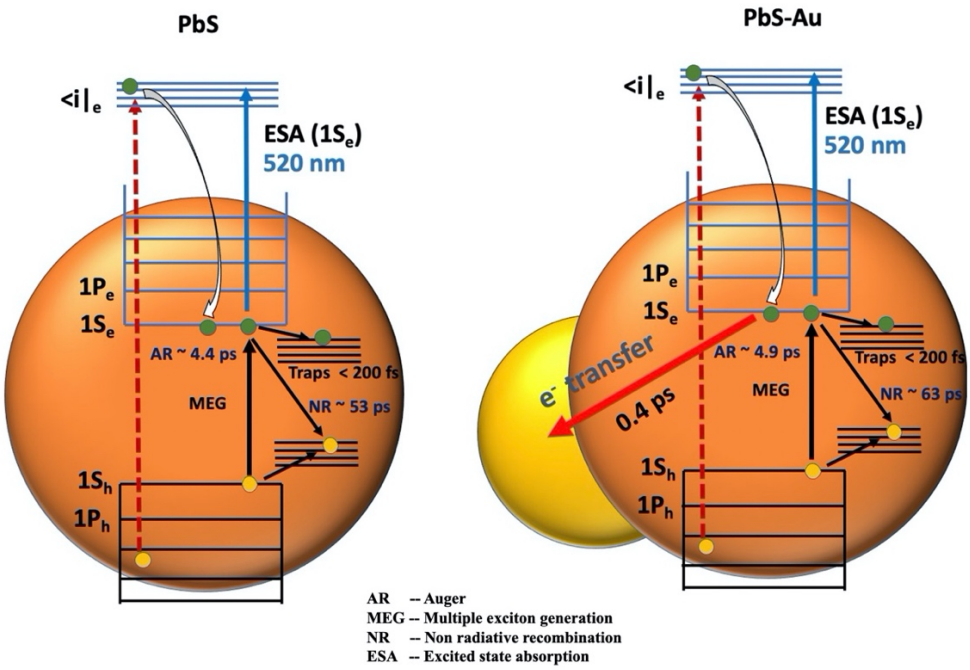


Figure 4.4. Schematic of the ESA dynamics from $1S_e$ level in the PbS and PbS-Au hetero nanostructures.

Table 4.2. Kinetic fitting parameters of the ESA from the $1P_e$ level in PbS and PbS-Au nanoparticles at different pump fluence

| Probe | Pump fluence ($\mu J/cm^2$) | sample | $\tau_1$ (ps) | $a_1$ | $\tau_2$ (ps) | $a_2$ |
|---|---|---|---|---|---|---|
| 650 nm ESA ($1P_e$) | 70 | PbS | 9.5±3 | 0.63±0.06 | 133±13 | 0.37±0.03 |
| | | PbS-Au | 10.3±2.2 | 0.61±0.07 | 222±40 | 0.39±0.02 |
| | 150 | PbS | 7±1.5 | 0.68±0.07 | 117±9 | 0.32±0.02 |
| | | PbS-Au | 9.2±1.2 | 0.52±0.04 | 189±22 | 0.48±0.04 |
| | 300 | PbS | 6.4±0.3 | 0.65±0.02 | 82±6 | 0.35±0.02 |
| | | PbS-Au | 4.2±0.4 | 0.60±0.03 | 96±16 | 0.40±0.05 |

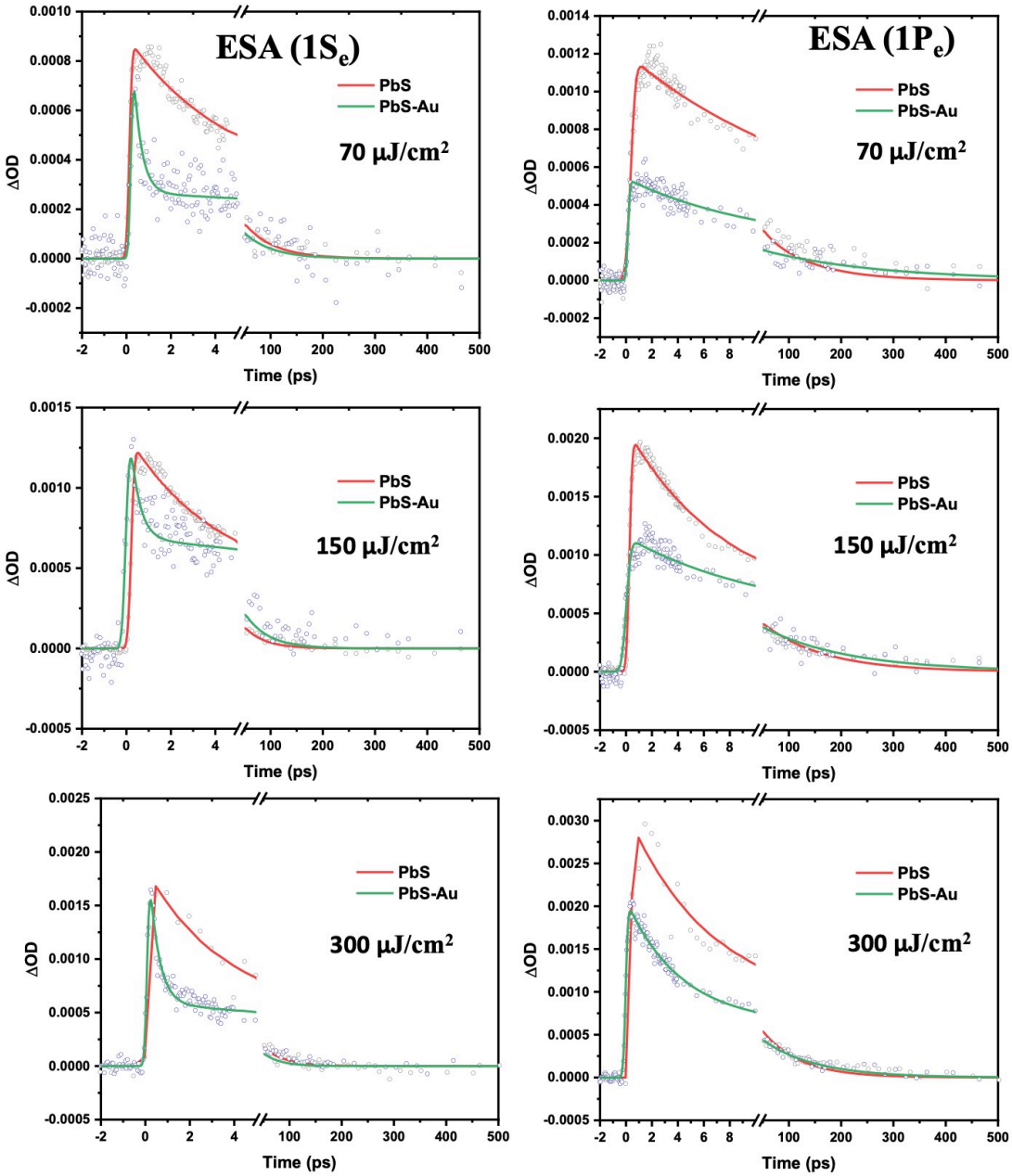


Figure 4.5. Kinetic decay profile comparison of PbS and PbS-Au heteronanostructures from $1S_e$ level( left panel, a,c,e) and from $1P_e$ level (right panel, b,d,f)

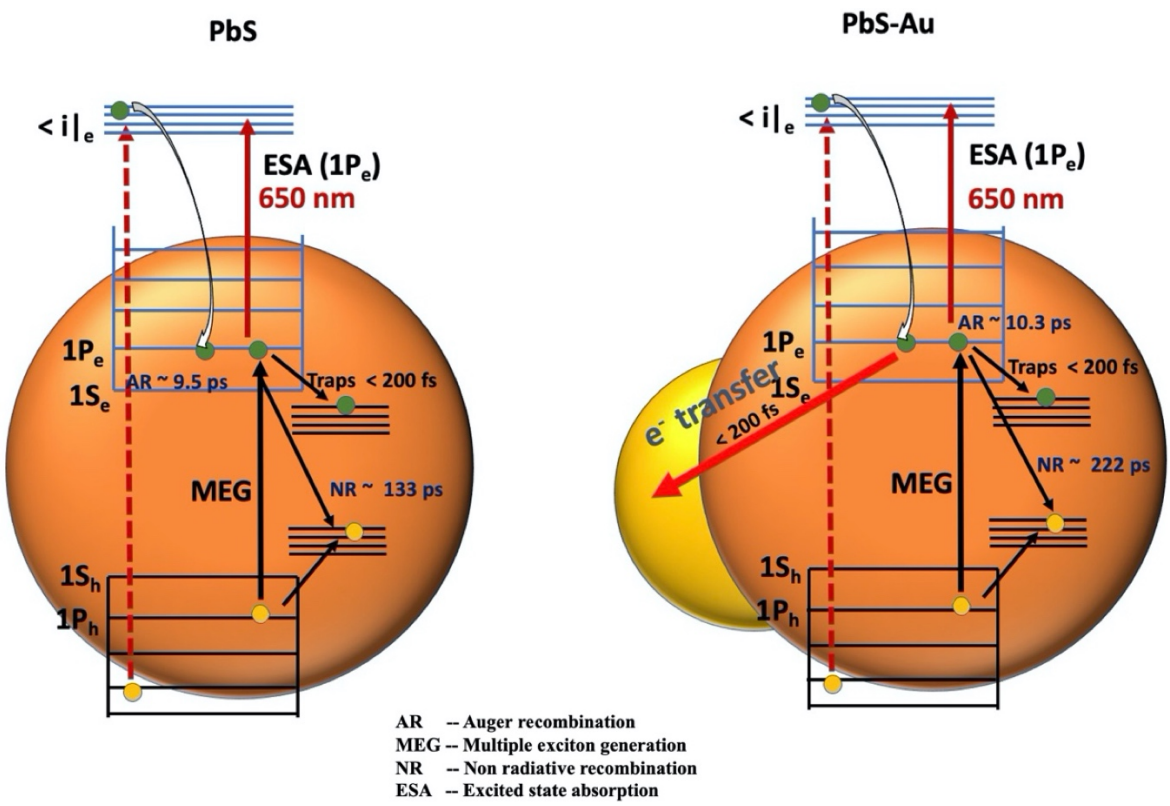


Figure 4.6. Schematic of the ESA dynamics from $1P_e$ level in the PbS and PbS-Au hetero nanostructures.

The kinetic fit data of the ESA from the $1P_e$ level in PbS nanoparticles (Table 2) have shown bi-exponential nature with time scales of 9.5 ps and 133 ps for the lowest fluence. We attribute the 9.5 ps component to Auger recombination rate and with the increase in pump fluence from 70-300 μJ/cm$^2$, faster Auger rate has been observed 9.5 ps to 6.4 ps. Figure 4.5 (b,d,f) shows the comparison of kinetic fit decay profiles of the both PbS and PbS-Au hetero nanostructures from $1P_e$ state. It is evident that at all pump fluence in the presence of gold, the ESA optical density decreases, implying an ultrafast charge transfer process faster than our instrument response function i.e 300 fs. The longer non radiative transfer component at each pump fluence seems to be slower in PbS-Au as compared to PbS samples. This could be due to decreased overlap of electron and hole wave function due to the charge separation at the gold interface, PbS interface. The schematic of the dynamics from $1P_e$ level in shown in Figure 4.6.

## 4.4 Conclusion

In summary, we have explored the ultrafast electron relaxation dynamics of cubic PbS-Au hetero nanostructures using transient absorption spectroscopy at very low pump fluence. Exciting the samples with more than 3 times the band gap is known to generate multiple excitons with a single photon in PbS quantum dots. In this context, we have systematically studied the ESA dynamics from $1S_e$ and $1P_e$ level. A 0.36 ps electron transfer component is observed from $1S_e$ level to gold and an ultrafast component faster than the instrument response function is observed from $1P_e$ level. This kind of ultrafast charge separation at the junction of the metal-semiconductor interface before Auger recombination and other relaxation channels is very crucial for the development of solar cells where multiple charge carriers created from the MEG can be extracted efficiently, leading to overcome the Shockley-Queisser limit.

# 5 Excited state charge separation dynamics in CZTS-Au nano heterostructures

## 5.1 Introduction

Metal-semiconductor hybrid heteronanostructures are the unique class of materials for solar to chemical and solar to electrical energy conversion applications. [159,254–262] Cost effective, high performance and environmentally friendly hybrid nano heterostructures are of particular interest in the solar energy conversion devices. Currently highly efficient photovoltaic devices are dominated by copper indium gallium selenide (CIGS) and cadmium telluride (CdTe). Quest for other green and earth abundant materials to circumvent toxic nature of cadmium and low abundance of indium, tellurium in the earth's crust, has picked up the momentum. One such green alternative material is copper zinc tin sulphide (CZTS)[263–266] which has gained a lot of attention because of its high absorption coefficient (>$10^4$ $cm^{-1}$), high mobility, non-toxicity, and direct band gap of 1.5 eV.[267,268] The other material such as $CZTS_xSe_{1-x}$ based materials have also been studied for photovoltaic applications and found to have efficiencies up to 12.6%. Metal nanoparticles, in particular plasmonic metals has a unique property, called as localized surface plasmon resonance which localizes the incident electric field thereby enhancing the overall light absorption, making them suitable candidates for photocatalytic and solar energy conversion. CZTS, when combined with the plasmonic metals such as Au and Pt, generates heterostructures like CZTS-Au and CZTS-Pt. These materials have gained attention for their use in the water splitting and other photocatalytic applications.[269] Also, heterostructure such as CZTS-Au is used in solar cells and is found to achieve 25% increase in the photoelectric conversion efficiency .[270]

In order to further optimize the device performance, understanding the photo physics of the excited charge carriers in these metal-semiconductor heterostructures is important. CZTS nanocrystals is known to have large surface area due to which a large number of trap states are present.[271,272] Most of the excited charge carriers are found to relax via trap mediated recombination. Pundsack *et al* have shown that the excited state in CZTS NCs are non-emissive and very short typically relaxing within 20 picoseconds.[271]

Various strategies are being explored to efficiently use the excited carriers in these systems before they relax to ground state non radiatively. Kaur *et al* have recently shown an ultrafast charge transfer in the heterojunction of CZTS/CdS system.[272] In this chapter we discuss the ultrafast charge relaxation dynamics in CZTS-Au nano heterostructures at different pump energies.

## 5.2 Experimental section

Synthesis of CZTS and CZTS-Au nano heterostructures is briefly described in chapter 2. The structures of CZTS and CZTS-Au nanostructures are characterized by transmission electron microscopy (TEM) and X-ray diffraction. UV-VIS absorption spectrum was recorded with JASCO V-530 UV/VIS spectrophotometer. Transient absorption spectrum was measured using femtosecond pump probe spectroscopy measurements. Second harmonic of 800 nm fundamental of mode locked Ti: Sapphire laser is used for the excitation of the samples. Pump excitation used was 0.5-1.3 $\mu$J/pulse. Probe region is maintained between 440-750 nm. The temporal resolution of the 400 nm excitation experiments were 200 femtoseconds.

## 5.3 Results and discussion

Optical studies have been carried out on the samples CZTS NRs and CZTS@Au nanocrystals obtained from Monash University. Figure 5.1a depicts the normalized absorption spectra of

CZTS NRs and CZTS-Au heterostructures. Absorption spectra (Figure 5.1a) match well with the reported literature on these systems and shows a broad absorption in the entire visible region.[271] Tauc plot (Figure 5.1b) shows that the band gap of the synthesized CZTS NRs to be ~1.6 eV.

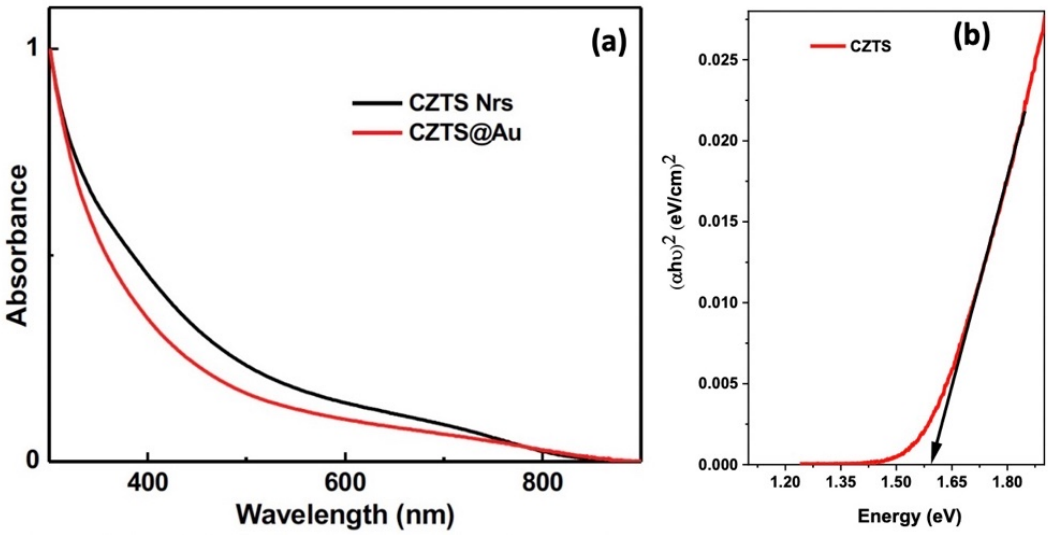


Figure 5.1. (a) Absorption spectra of CZTS NRs and CZTS@Au heterostructure at room temperature. (b) Tauc plot of CZTS nanorods.

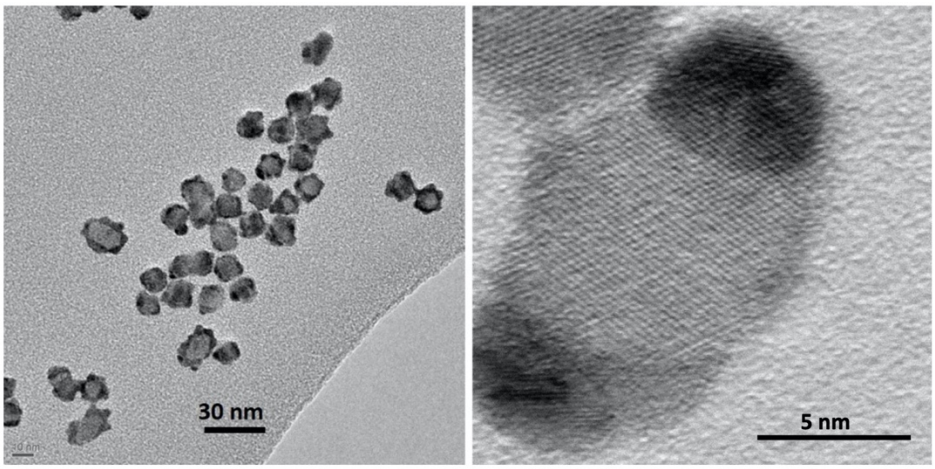


Figure 5.2: HR TEM images of CZTS@Au heteronanostructures.

High resolution TEM images of the synthesized CZTS-Au heteronanostructures shown in Figure 5.2 shows the average size of the CZTS nanorods to be around 10nm. Bohr exciton radius of the CZTS nanocrystals have been found out to be 2.5-3.3 nm by previous studies.[273] This indicates that the synthesized CZTS NRs are not in the quantum confinement regime. No photoluminescence was observed from the particles in the visible region of the spectrum, placing the quantum yield of the particles to be very low. This suggests that the majority of the charge carriers recombine non radiatively after excitation. Extraction of excited hot electrons before trapping into non emissive states is crucial for realizing the application of these materials in photovoltaics. Transient absorption spectroscopy is one such technique where we can follow these very fast non-emissive relaxation processes.

Transient absorption studies were carried on these samples at different pump energies (0.5, 1, 1.3 μJ pump energy per pulse). Optical density of both CZTS and CZTS-Au NRs is maintained constant at the excitation pump wavelength of 400 nm for all the measurements. Figure 5.3 shows the Transient absorption spectra and kinetic decay data measured at 630 nm of the CZTS NRs.

Although the transient absorption for CZTS NRs shows similar features as compared to reported literature of 5 nm CZTS nanocrystals there is change in peak maximum (red shift of about 70 nm) which is due to change in the size of the nanocrystal.[271] Here, we must note that excited state absorption is dominating the ground state bleach signal giving rise to only positive signal. Even after adjusting good optical density in the absorption of the sample, we could get only few mOD for transient absorption measurements which is due to domination of excited state absorption (ESA) over ground state bleach signal throughout the visible probe region. The high density of trap states could possibly favour the excited state absorption over ground

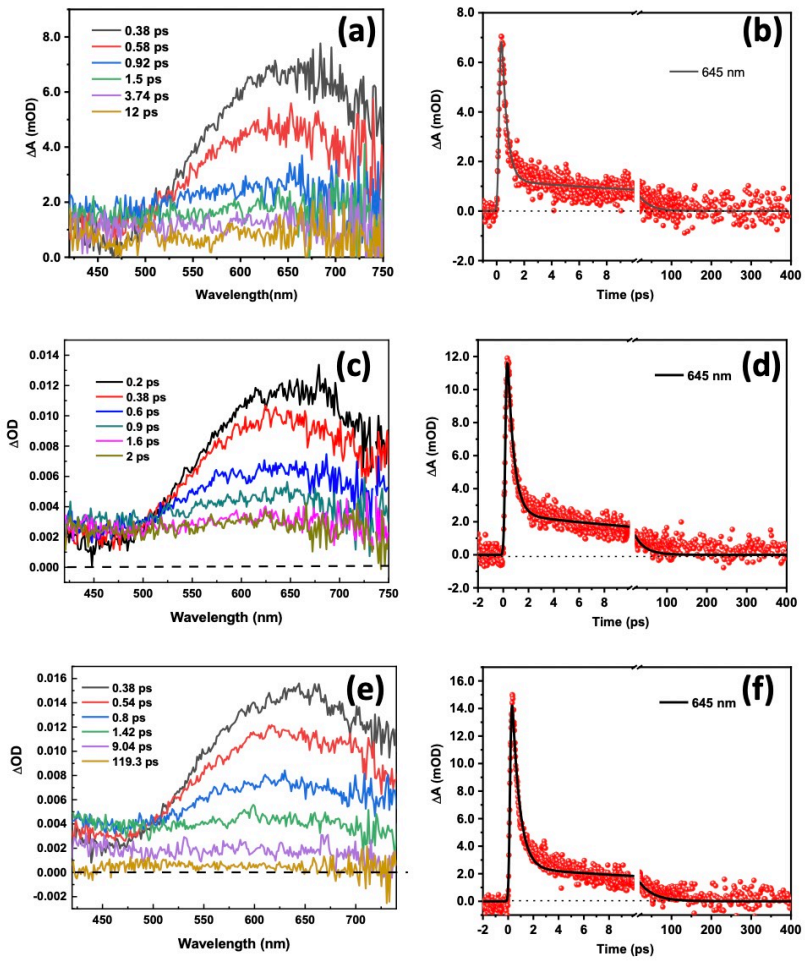


Figure 5.3 (a, c, e) Transient absorption spectra of CZTS NRs at different pump energies 0.5$\mu$J/pulse, 1$\mu$J/pulse, 1.3$\mu$J/pulse respectively. (b,d,f) Kinetic data of the CZTS NRs measured at 645 nm at pump energies 0.5$\mu$J/pulse, 1$\mu$J/pulse, 1.3$\mu$J/pulse respectively.

state bleach in the entire region probed. The blue shift in the transient absorption spectra peak maxima of 645 nm is evident at higher excitation intensities. This is due to the interband relaxation of the hot electrons within the first conduction band. Since the excitation energy is higher than the band gap of the CZTS NRs, initially electrons populate the higher energy levels in the conduction band. They store the excess energy in the form of kinetic energy. Typically these electrons are of higher temperature than the band edge electrons. These higher energy electrons are termed as hot electrons. As the time passes hot electrons relax to the lower levels in the conduction band and require higher energy to undergo the excited state absorption from

that state resulting in slight blue shift of the ESA. The kinetic fit data (shown in Table 5.1) of the ESA at 645 nm reveals a fast component of 0.4 ps in CZTS NRs followed by a comparatively slower 1 ps component and finally with a slightly longer 30 ps component. We attribute the fast component of 0.4 ps to hot electron trapping and 1 ps component to cold electron trapping after interband relaxation. Low quantum yield observed in these materials suggest that the recombination of the excited charge carriers mostly through non radiative recombination. Due to this reason and the absence of any residual bleach signal we attribute the 40 ps component to non-radiative recombination channel. Negligible effect of pump fluence on the excite state dynamics rules out the possibility of Auger processes.

Table 5.1 Time Constants, and Normalized Amplitudes for Triexponential Fits of CZTS NRs Pump−Probe Data excited at 400 nm pump pulse.

| **Pulse energy ($\mu$J/pulse)** | **Wavelength (nm)** | **$\tau_1$ (ps)** | **$a_1$** | **$\tau_2$ (ps)** | **$a_2$** | **$\tau_3$ (ps)** | **$a_3$** |
|---|---|---|---|---|---|---|---|
| 0.5 | 645 | 0.38±0.08 | 0.77±0.09 | 1.5±0.2 | 0.12±0.02 | 38.4±3.15 | 0.11±0.02 |
| 1 | 645 | 0.42±0.06 | 0.69±0.07 | 1.3±0.3 | 0.22±0.03 | 40.1±3.25 | 0.09±0.01 |
| 1.3 | 645 | 0.39±0.03 | 0.58±0.05 | 1.4±0.14 | 0.31±0.04 | 47.28±4.68 | 0.11±0.02 |

Maintaining the same OD as CZTS NRs at excitation pump wavelength 400 nm and keeping all the other variables similar, transient absorption studies were performed on the CZTS-Au heteronanostructures (shown in Figure 5.5). By following the relaxation dynamics of excited state absorption, it is found out that fast trapping of the hot electrons into shallow trap states is completely eliminated and significant decrease in the OD (shown in Figure 5.4 and figure 5.5 ) of the ESA signal suggesting that there is an ultrafast charge separation happening at the heterojunction of CZTS and gold. This ultrafast hot electron transfer from CZTS to gold occurs

faster than the instrument response function which is about 200 fs, which makes it difficult to extract that component in decay kinetics.

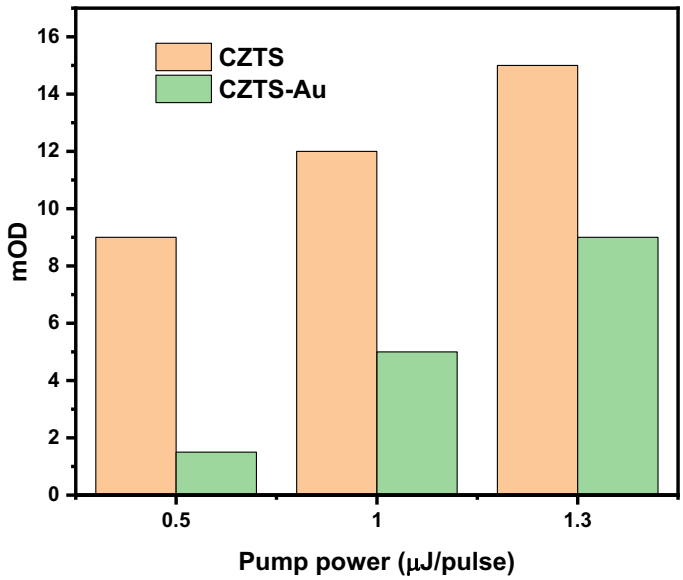


Figure 5.4. Reduction of the photoinduced absorption optical density in CZTS-Au as compared to CZTS NRs.

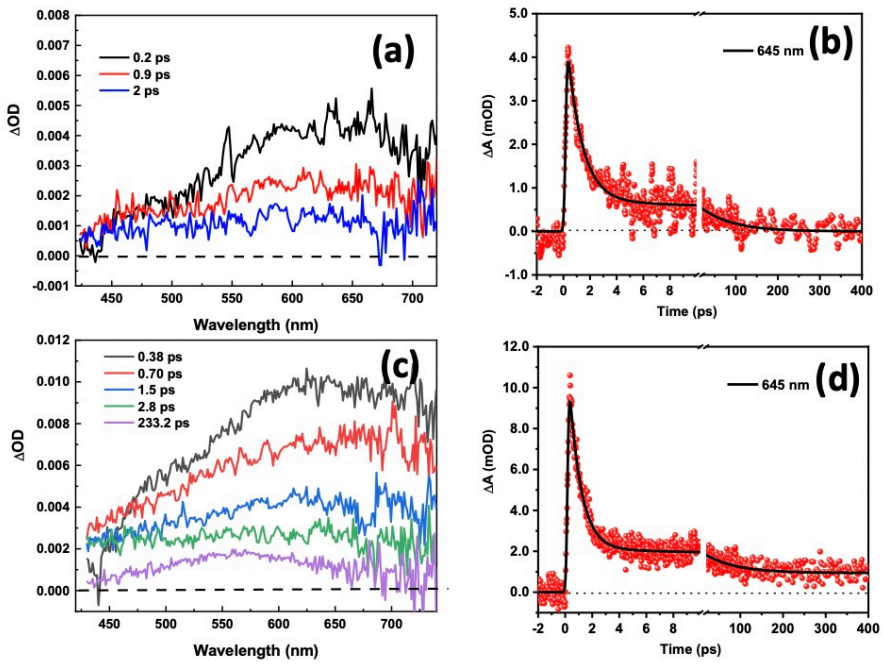


Figure 5.5. (a, c) Transient absorption spectra (b, d) Kinetic data at 645 nm of the CZTS-Au NRs measured at pump energies 1$\mu$J/pulse, 1.3$\mu$J/pulse respectively.

The kinetic fit data (shown in Table 5.2) of the ESA at 645 nm reveals a 1 ps component which is cold electron trapping after interband relaxation. It is then followed by 70 ps non emissive recombination channel. The very clear change in the second component of 40 ps in CZTS to 70 ps in CZTS-Au heterostructure could be due to the charge separation at the interface which makes the charge carriers free as compared to bound exciton state in CZTS NRs. This reduction in overlap of electron and hole wave function at the interface results in a slower non emissive recombination channel.

This effective charge separation at the interface of CZTS and gold is crucial for developing the efficient photovoltaic devices since electrons are being transferred to the gold faster than the trapping process in bare CZTS nanoparticles. The overall hot carrier relaxation dynamics in CZTS NRs and CZTS-Au heteronanostructures is schematically shown in Figure 5.6.

Table 5.2. Time Constants, and Normalized Amplitudes for Triexponential Fits of CZTS-Au hetero nanostructure Pump−Probe Data excited at 400 nm pump pulse.

| **Pulse energy ($\mu$J/pulse)** | **Wavelength (nm)** | **$\tau_1$ (ps)** | **$a_1$** | **$\tau_2$ (ps)** | **$a_2$** | **$\tau_3$** | **$a_3$** |
|---|---|---|---|---|---|---|---|
| 0.5 | 645 | -- | -- | -- | -- | -- | -- |
| 1 | 645 | 1.1±0.2 | 0.85±0.06 | 73.7±14 | 0.15±0.03 | -- | -- |
| 1.3 | 645 | 0.9±0.2 | 0.82±0.07 | 73.4±11 | 0.1±0.02 | > 1 ns | 0.08± 0.01 |

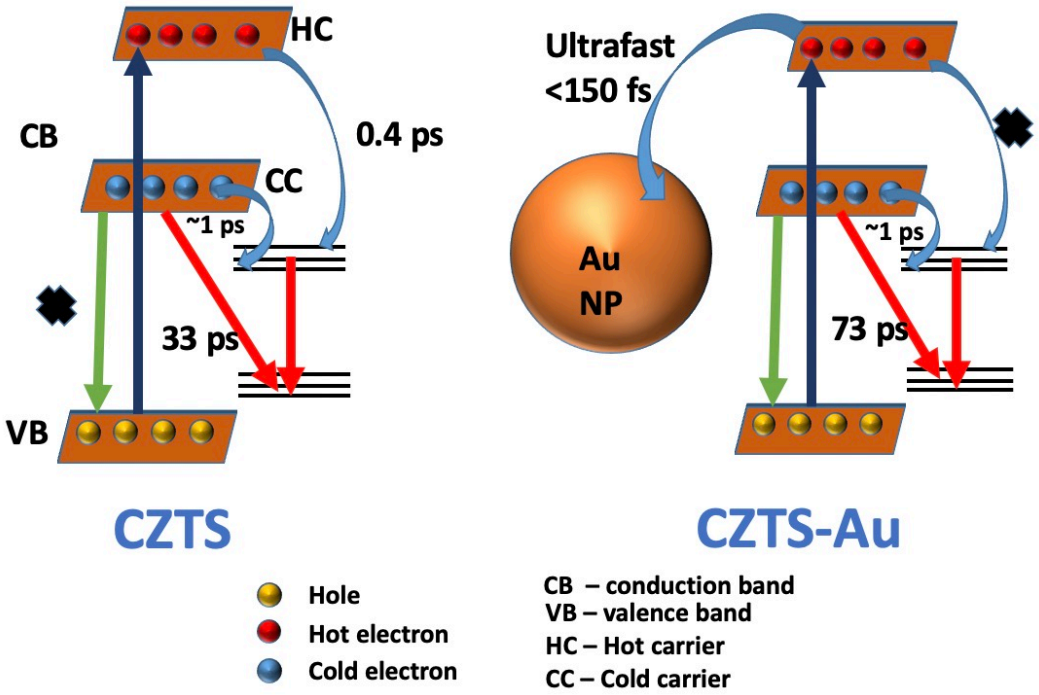


Figure 5.6. Schematic showing the hot electron relaxation dynamics in CZTS NRs and CZTS-Au heteronanostructures.

## 5.4 Conclusion

In summary, Ultrafast excited state dynamics in CZTS NRs and CZTS-Au nano heterostructures have been measured using pump probe spectroscopy for the first time. The observed photoinduced absorption in the entire probe region suggests the domination of excited state absorption over ground state bleach. Excited state dynamics of CZTS NRs reveal a very fast hot electron trapping process within 0.4 ps followed by 1 ps cold electron trapping and finally 40 ps component corresponding to the non-radiative recombination. Transient absorption spectra in CZTS-Au nanostructures resulted in reduction of the optical density of the ESA suggesting an ultrafast charge transfer faster than the hot electron trapping process and within the instrument response function (200 fs). This ultrafast charge transfer process

faster than the trapping process is crucial in optimizing the CZTS based nanostructures in photovoltaic applications.

# 6 Ultrafast charge separation at the interface of Phenothiazine porphyrin/$TiO_2$ interface

## 6.1 Introduction

Insight of multistep electron transfer processes, involving sequential electron/hole transfer between energetically well-positioned molecular entities following redox gradient eventually generating long-lived charge separated states is crucial for efficient conversion of light energy and building optoelectronic devices.[274,275] The dynamics of interfacial sequential electron transfer between molecules adsorbed on semiconductor nanoparticles has attracted research attention, especially in the context of dye sensitized solar cells and photocatalysis. Electron transfer rates are comprehensive and complicated by heterogeneity of films.[276277278] This has motivated understanding of electron transfer dynamics in well-designed systems comprising of molecules bound to semiconductor nanocrystals (NCs) dispersed in solution providing a platform for detailed investigations of the kinetics.[279,280]

Among various sensitizers studied, porphyrin based dyes have an edge over the previously studied organometallic and metal free organic dyes, due to the high molar extinction coefficient, tunablity of optical and electronic properties and synthetic viability which allows to functionalize these chromophores at multiple sites making them a good alternative. The core of the porphyrin macrocycle can be functionalized with different substituents on the meso position to obtain the desired architecture such as $A_4$, $A_3B$, $A_2B_2$, and $A_2BC$ and tune the optoelectronic properties. $A_3B$ architecture has ~~have~~ gained significant attention because of the loss of symmetry which further disturbs the delocalized π electrons creating a dipole moment which allows tuning the photophysical and electrochemical processes. In addition, $A_3B$ architecture provides us an opportunity to place bulky groups at meso position that hinders π– π stacking which in turn minimizes aggregation and promotes the solubility.

Basic design of donor -acceptor conjugates connected by either covalent bonds or supramolecular approaches demonstrating sequential electron transfer includes chromophores linked in the fashion (secondary donor)–primary donor–acceptor.[281,282] In such conjugates, when the primary electron donor is selectively excited, a radical cation and anion is generated on the donor and acceptor respectively due to primary electron transfer. It is then followed by a secondary electron transfer, as a consequence of which the hole is shifted to the secondary electron donor, consequently, creating a long lived charge separated state.[283,284]A variety of photo/redox-active entities such as triphenylamine, ferrocene,[285,286] tetrathiofulvalene,[287,288] phenothiazine,[185,289] and etc., have been employed as terminal secondary electron donors with the idea to promote secondary electron transfer leading to generation of a long lived charge separated state.[285] Among these, phenothiazine (PTZ), a hetero-anthracene chromophore containing two electron-rich heteroatoms—nitrogen and sulfur, have been in spotlight as it is endowed with remarkable structural, electrochemical and photophysical properties imparting strong electron donating ability and high propensity to form stable radical cations.[290] In addition, the nonplanar butterfly conformation in ground state imparts anti aggregation character making them useful candidates in dye sensitized solar cells[291–293] and organic light emitting diodes[292294] Phenothiazine based dye sensitized solar cells have shown increased solar conversion efficiency in the literature. Recently, Li and co-workers have designed double anchored phenothiazine sensitizers having a tetraphenylethylene moiety at the N-10 with various π-spacers reported a device efficiency of 9.79% using liquid redox electrolyte.[185]

Despite several reports on investigations of electron transfer dynamics of electron injection and charge recombination dynamics on organic and inorganic dye-sensitized $TiO_2$ nanoparticles.[295296] Role of relative distance, orientation, and the nature of the linkages connecting the secondary electron donor are scarce.

Phenothiazine appended porphyrins forming cyclic dimer have been used to form inclusion complexes with fullerenes.[297] Previously, aluminium porphyrin and fullerene based supramolecular triads have been employed to study the sequential charge separation in the axial direction.[289] Also, porphyrin functionalized with up to four phenothiazine moieties having utility in photodynamic therapy[298] and photonic devices[299] have been reported. In addition, porphyrins appended with up to three phenothiazine units having high photon-to-current conversion efficiency have been reported.[300–302] However, to the best of our knowledge, no results involving the synthesis of covalently-connected phenothiazine substituted acid porphyrins adsorbed on $TiO_2$ nanorods as acceptor and study of ultrafast interfacial sequential electron events with respect to linker size have been reported till date.

In the present work, we have designed $A_3B$ porphyrin sensitizers in which the three *meso*-positions are decorated with three phenothiazine moieties tethered to porphyrin core, and the other *meso*-position is functionalized with phenyl carboxylic acid which can play a dual role as acceptor and anchoring group (scheme 2.1). A series of phenothiazine-porphyrin systems in which phenothiazine tethered to porphyrin with different linkages such as phenyl, alkynyl, and phenoxyl alkyl linkages (Scheme 2.2) and carboxylic acid anchoring group to attach to the semiconductor nanoparticles such as $TiO_2$. The efficiency of primary and secondary photo-induced electron transfer w.r.t. linker sizes were investigated. Here, we report the effect of spacer (via direct, phenyl and phenyl acetylene linkage) connecting the hole shifting agent, phenothiazine (PTZ), on photoinduced charge stabilization in phenothiazine porphyrin conjugates. Here, phenothiazine entity acts as hole shifting agent. The synthesized moieties were characterized by optical absorption and emission. More importantly, here phenothiazine not only acts as a chromophore that can absorb light from 200 – 350 nm but also behaves as a secondary (sacrificial electron donor) or p-type material, and decreases the rate of charge recombination, which thereby, increases the lifetime of the charge separated state necessary

for the light capture. Using femtosecond transient absorption techniques, evidence for charge separation, and kinetics of charge separation and recombination were obtained. Details of these findings are summarized below.

## 6.2 Experimental

Synthesis of phenothiazine porphyrin compounds and $TiO_2$ nanorods is briefly described in Chapter 2. The structure of $TiO_2$ nanorods are characterized by transmission electron microscopy (TEM) and X-ray diffraction. UV-VIS absorption spectrum was recorded with JASCO V-530 UV/VIS spectrophotometer. Transient absorption spectrum was measured using femtosecond pump probe spectroscopy measurements. Second harmonic of 800 nm fundamental of mode locked Ti: Sapphire laser is used for the excitation of the samples. Pump fluence used for the transient absorption studies was 50 $\mu J/cm^2$. Probe region is maintained between 350-500 nm. The temporal resolution of the 550 nm excitation experiments were 300 femtoseconds.

## 6.3 Results and discussion

The synthesis of phenothiazine substituted acid porphyrins was initiated with the preparation of formyl functionalized phenothiazine, (**Scheme 2.1**). For this, PTZ was treated with 1-bromohexane in the presence of NaH and DMF to yield **2.1** which was further reacted with $POCl_3$ and DMF to yield **2.2**, aldehyde precursor. Also **2.1** was reacted with *N*-bromosuccinimide followed by Suzuki coupling reaction with 4-formylboronic acid and sonogashira coupling reaction to yield **2.4** and **2.5** respectively in good yields. All the NMR and mass data is given in the appendix after the last chapter. The synthesis of $A_3B$ Zn (II) phenothiazine porphyrins involved three steps. Firstly, $A_3B$ ester porphyrins were prepared by Adler Longo and Lindsey's procedure.[298,303] One pot reaction involved the condensation of aldehyde precursors (3 eq) **2.2**, **2.4**, **2.5**, and methyl 4-formyl benzoate (1 eq) with pyrrole (4

eq), in presence of mixed solvent system propionic acid, acetic acid and nitrobenzene upon reflux at 135°C. In the second step, $A_3B$ acid porphyrins were obtained $(PTZ)_3$-$H_2PCOOH$, $(PTZ\text{-}Ph)_3$-$H_2PCOOH$ and$(PTZ\text{-}PhAc)_3$-$H_2PCOOH$ by base hydrolysis of the ester precursors **(**$PTZ)_3$-$H_2PCOOMe$, $(PTZ\text{-}Ph)_3$-$H_2PCOOMe$ and $(PTZ\text{-}PhAc)_3$-$H_2PCOOMe$ in presence of KOH. Further to obtain $A_3B$ acid Zn (II) phenothiazine porphyrin dyes, metallation of the free base acid porphyrins was done upon treating with zinc acetate in methanol to yield the phenothiazine porphyrins $(PTZ)_3$-ZnPCOOH, $(PTZ\text{-}Ph)_3$-ZnPCOOH and $(PTZ\text{-}PhAc)_3$-ZnPCOOHin good yields (**Scheme 2.2**). All phenothiazine-porphyrin compounds were found to be soluble in most of the solvents such as $CHCl_3$ and DCM etc. indicating absence of aggregation within these macrocycles due to non-planar phenothiazine. This enabled us to perform the photophysical studies with greater ease. The phenothiazine porphyrin sensitizers were characterized using $^1H$ NMR, ESI-HRMS and various spectroscopic techniques and electrochemical methods. Figure 6.1 shows the different structural moieties on which the current studies have been performed. XRD pattern (shown in Figure 6.2b) of the synthesized $TiO_2$ NPs shows anatase phase and all the peaks matches with the literature confirming the pure crystalline phase of the particles.[181]

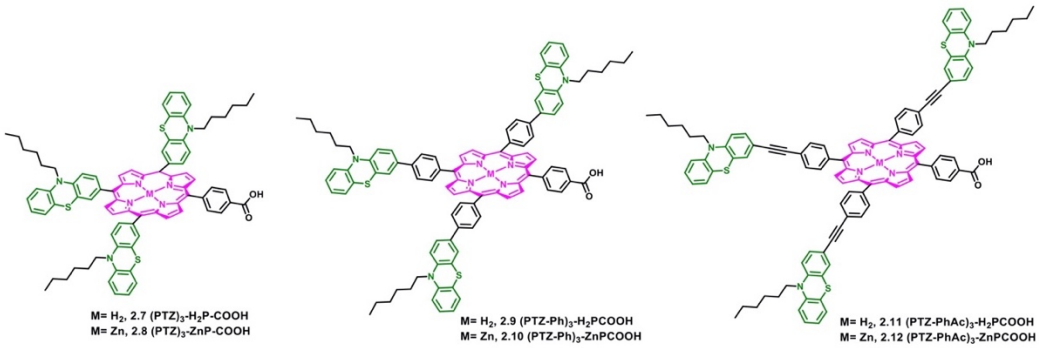


Figure 6.1. Schematic showing porphyrin moieties with different linkers used in the study. code names for easy representation are given underneath each compound.

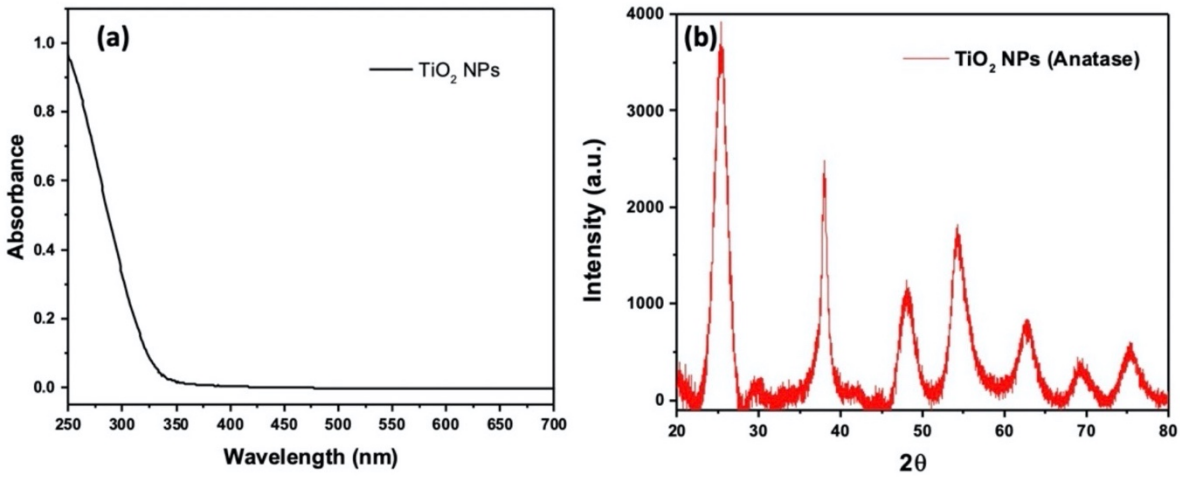


Figure 6.2. (a) Absorption spectrum of $TiO_2$ NRs in chloroform and (b) XRD pattern of the synthesized $TiO_2$ NRs.

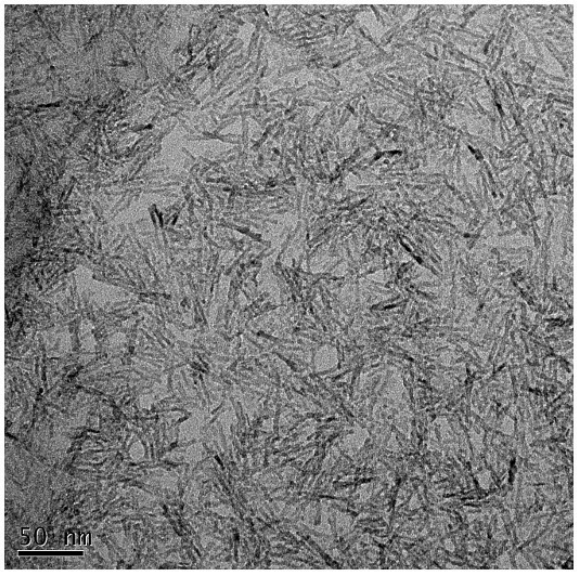


Figure 6.3. TEM image of the $TiO_2$ NRs with the average length of the rods around 12 nm.

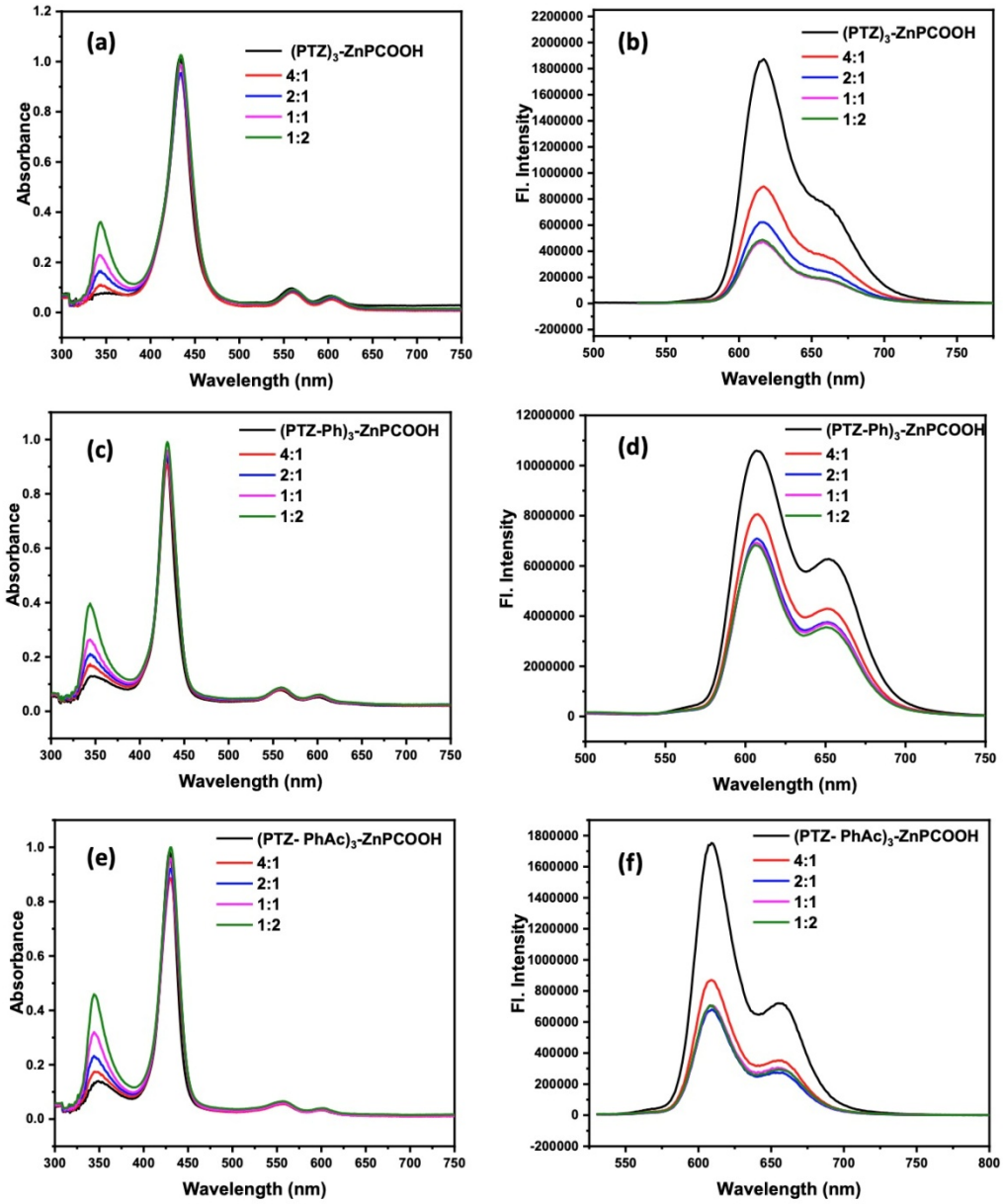


Figure 6.4. Absorption (a,c,e) and emission spectra (b,d,f) of $(PTZ)_3$-ZnPCOOH, $(PTZ\text{-}Ph)_3$-ZnPCOOH and $(PTZ\text{-}PhAc)_3$-ZnPCOOH moieties respectively with different dye to $TiO_2$ NR ratios.

Phenothiazine porphyrin with acid moieties are mixed with $TiO_2$ NRs and stirred for 10 minutes. Carboxylate having high affinity to the surface attaches to the $TiO_2$ NRs forming dye-NR conjugates. To observe the electron transfer from excited dye molecules to nanorod systems, fluorescence quenching experiments have been performed. Optical density of the soret band at 420 nm of porphyrins is fixed at 1. Figure 6.4 shows the Absorption (a,c,e) and emission spectra (b,d,f) of $(PTZ)_3$-ZnPCOOH, $(PTZ\text{-}Ph)_3$-ZnPCOOH and $(PTZ\text{-}PhAc)_3$-

ZnPCOOH moieties respectively with different dye to $TiO_2$ NR ratios. Approximate $TiO_2$ nanorod concentration is found out by drying the sample and by assuming them to be monodisperse cylindrical rods. Calculations were done using density and surface area of the nanorods. Dye to nanorod concentration varied from 4:1 to 1:2.

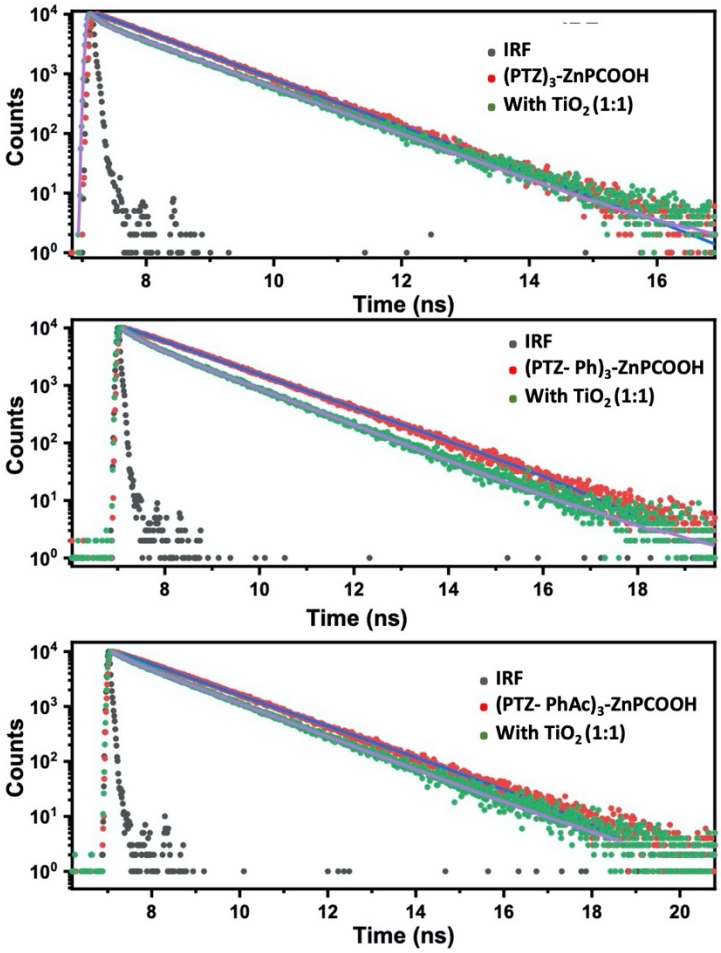


Figure 6.5. Comparison of the TCSPC data of porphyrin compounds and its dye:nanorod conjugate with 1:1 ratio of $(PTZ)_3$-ZnPCOOH (Top panel, Ex/Em- 420/616 nm), $(PTZ\text{-}Ph)_3$-ZnPCOOH (middle panel, Ex/Em- 420/607 nm), $(PTZ\text{-}PhAc)_3$-ZnPCOOH (bottom panel, Ex/Em- 420/609 nm).

The fluorescence quenching in the all four samples have shown gradual quenching and then saturating at 1:2 dye to NR concentration. To understand the nature of fluorescence quenching we have performed time resolved fluorescence quenching of the four porphyrin samples along with their NR conjugate at 1:1 ratio respectively by using time corelated single photon counting

(TCSPC) experiments (shown in Figure 6.5). TCSPC experiments were conducted with the excitation of soret band of the porphyrin molecules at 420 nm and the fluorescence decay was observed at first soret band maximum. $(PTZ)_3$-ZnPCOOH molecule shows a single exponential decay with a lifetime of 1.1 ns, whereas other two phenothiazine porphyrin molecules shows lifetime of 1.5 ns approximately. However, in the presence of $TiO_2$ NRs, conjugates shows a fast fluorescence decay component in the range of 96-354 ps (shown in Table 6.1). This fast component can be attributed to electron transfer from the singlet $S_1$ state of the porphyrins to the conduction band of $TiO_2$ NRs.

Table 6.1. Fit parameters for the decay of the direct connected dye and its NR conjugate at 1:1 ratio using TCSPC.

| **Ex/Em** | **Sample** | **$\tau_1$ (ps)** | **$a_1$** | **$\tau_2$ (ns)** | **$a_2$** | **Chi sq** |
|---|---|---|---|---|---|---|
| 420/616 nm | $(PTZ)_3$-ZnPCOOH | -- | -- | 1.09± 0.003 | 1 | 1.04 |
| | With NR | 96±9 | 0.08±0.02 | 1.11± 0.005 | 0.92±0.09 | 1.10 |
| 420/607 nm | $(PTZ\text{-}Ph)_3$-ZnPCOOH | -- | -- | 1.51± 0.005 | 1 | 1.2 |
| | With NR | 354±29 | 0.14±0.05 | 1.38± 0.007 | 0.86±0.07 | 1.10 |
| 420/609 nm | $(PTZ\text{-}PhAc)_3$-ZnPCOOH | -- | -- | 1.54± 0.005 | 1 | 1.2 |
| | With NR | 343±62 | 0.06±0.01 | 1.44± 0.009 | 0.94±0.09 | 1.16 |

In order to clearly understand the overall picture and various non radiative processes like charge transfer, intersystem crossing etc., transient absorption measurements have been performed on all the samples and their respective nanorod conjugates at 1:1 ratio. Excitation of the porphyrin samples with soret band peak maximum wavelength of 420 nm lead to the photobleaching of the samples very quickly due to the very high extinction coefficient. So we relied on Q-band excitation with 550 nm and observed the ground state bleach recovery

dynamics in the region of 350-500 nm. Transient absorption spectra shown in Figure 6.6 clearly indicates a strong bleach signal of the soret band at 420 nm immediately after excitation. In addition a weak photoinduced absorption signal is observed at the red and blue end of the bleach signal with peak maxima at 380 nm and 460 nm. The analysis of the decay profile (Figure 6.7) of the bleach signal at 420 nm of the dye samples suggests that relaxation dynamics has been best fitted with three exponentials with the time constants of 300-500 ps, 1300-1500 ps and a component greater than 7 ns. Considering the amplitude of the 1300-1500 ps component which falls in the range of quantum yield of the dye samples which is around 3%, this component can be attributed to radiative recombination. Persistence of the bleach recovery beyond 7 ns suggests that the transfer of excited electron in the $S_1$ band in the charge separated state to a long lived state such as a triplet state. The third component in the bleach recovery which is 300-500 ps can be attributed to non-radiative recombination channel. The analysis of the decay profiles of the dye-nanorod conjugates has shown an additional fast bleach recovery pathway. The fast recovery channel with the timescale of 4.4 ps, 25 ps , 68 ps is observed for$(PTZ)_3$-ZnPCOOH, $(PTZ\text{-}Ph)_3$-ZnPCOOH and $(PTZ\text{-}PhAc)_3$-ZnPCOOH respectively. This fast recovery can be attributed to the back electron transfer (BET) of the injected electrons in the $TiO_2$ nanorods to the $S_0$ state of the porphyrin dye. Decrease in the amplitude of the long component of 7 ns in the presence $TiO_2$ NRs as observed in Table 6.2 suggests that the fast electron transfer pathway competes with the electron transfer to the long lived state.

Analysis of the TCSPC data along with the transient absorption studies reveals the overall charge separation and charge relaxation dynamics of the dye-NR conjugates. BET timescales observed faster than the electron injection rate from the $S_1$ state to conduction band of $TiO_2$ suggests the presence of an additional fast electron injection from the $S_1$ state which is faster than our instrument response function of 300 fs. Overall charge injection and BET dynamics shows that $(PTZ\text{-}PhAc)_3$-ZnPCOOH compound shows promise as the best sensitizer

among the compounds examined with its faster electron injection and slower back electron transfer. The overall charge recombination dynamics in shown in Figure 6.8.

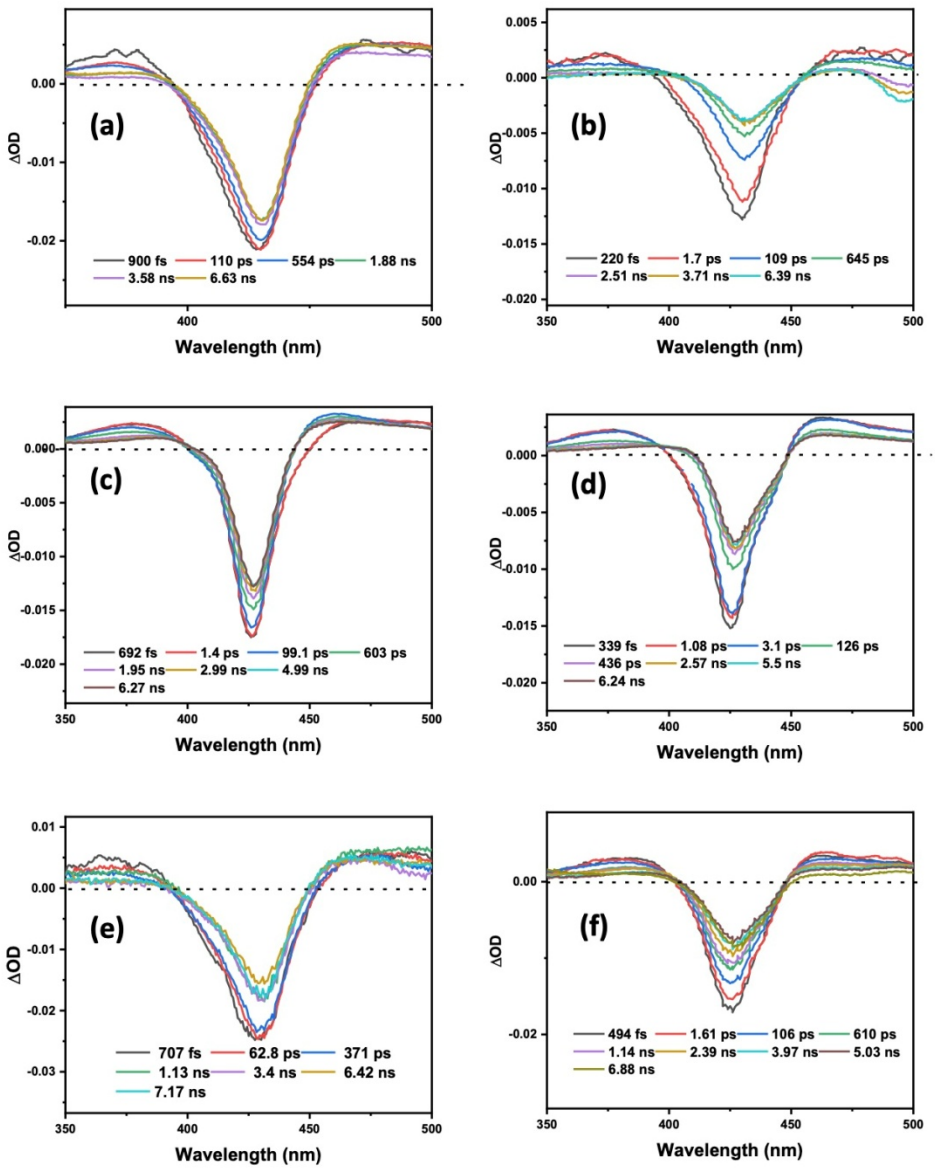


Figure 6.6. Transient absorption spectra at different probe delay of a) $(PTZ)_3$-ZnPCOOH, b) $(PTZ)_3$-ZnPCOOH/$TiO_2$, c) $(PTZ\text{-}Ph)_3$-ZnPCOOH, d) $(PTZ\text{-}Ph)_3$-ZnPCOOH/$TiO_2$ , e) $(PTZ\text{-}PhAc)_3$-ZnPCOOH, f) $(PTZ\text{-}PhAc)_3$-ZnPCOOH/$TiO_2$.

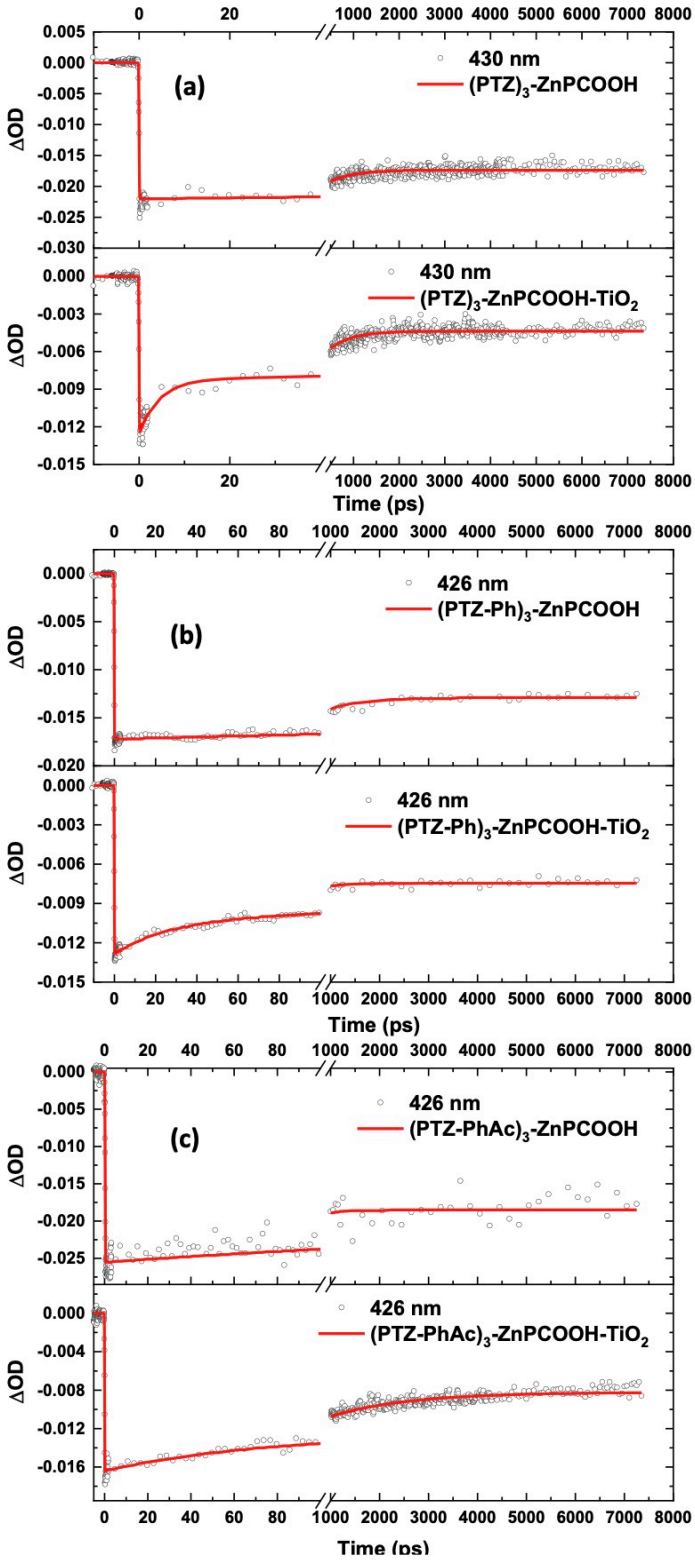


Figure 6.7. Comparison of the kinetic decay profiles of the bleach signal data of porphyrin compounds and its NR conjugate with 1:1 ratio of a) $(PTZ)_3$-ZnPCOOH, b) $(PTZ\text{-}Ph)_3$-ZnPCOOH and c) $(PTZ\text{-}PhAc)_3$-ZnPCOOH.

Table 6.2. Fit parameters for the kinetic decay profile of the ZnP dye and its NR conjugate at 1:1 ratio using pump probe spectroscopy.

| Pump fluence ($\mu J/cm^2$) | Sample | $\tau_1$ (ps) | $a_1$ | $\tau_2$ (ps) | $a_2$ | $\tau_3$ (ps) | $a_3$ | $\tau_4$ (ps) | $a_4$ |
|---|---|---|---|---|---|---|---|---|---|
| 50 | $(PTZ)_3$-ZnPCOOH | -- | -- | 520±30 | 0.13±0.01 | 1300±200 | 0.10±0.03 | >7ns | 0.77±0.03 |
| | With NR | 4.4±1.2 | 0.37±0.03 | 540±30 | 0.30±0.03 | 1330±110 | 0.02±0.01 | >7ns | 0.31±0.01 |
| | $(PTZ\text{-}Ph)_3$-ZnPCOOH | -- | -- | 710±30 | 0.21±0.02 | 1450±60 | 0.04±0.01 | >7ns | 0.75±0.02 |
| | With NR | 25.7±4 | 0.32±0.02 | 380±40 | 0.23±0.04 | 1360±60 | 0.10±0.02 | >7ns | 0.35±0.03 |
| | $(PTZ\text{-}PhAc)_3$-ZnPCOOH | -- | -- | 360±40 | 0.66±0.03 | 1580±80 | 0.04±0.02 | >7ns | 0.30±0.02 |
| | With NR | 68±10 | 0.19±0.02 | 300±30 | 0.02±0.01 | 1670±110 | 0.31±0.02 | >7ns | 0.48±0.03 |

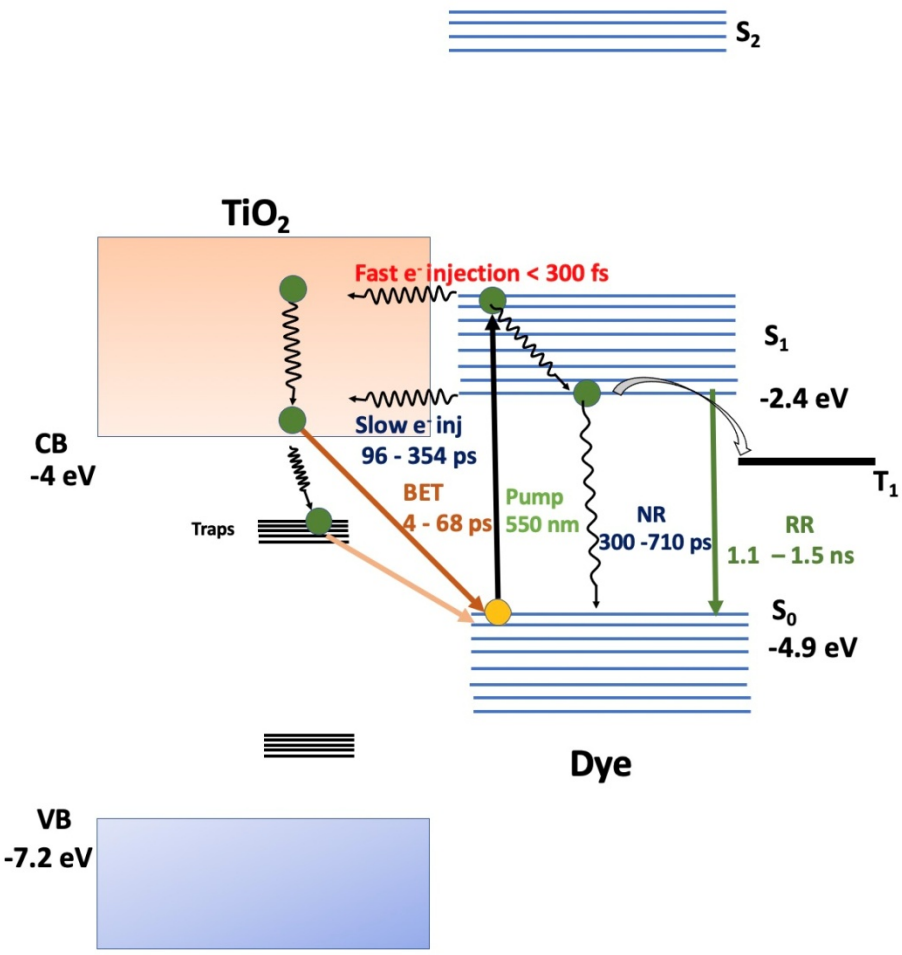


Figure 6.8. Schematic showing the charge separation and charge relaxation dynamics of dye-NR systems.

## 6.4 Conclusion

Successful binding of phenothiazine porphyrin dye moieties on the surface of $TiO_2$ nanorods has been demonstrated. Fluorescence quenching studies reveal that maximum quenching of the fluorescence occurs at 1:1 dye to nanorod ratio. TCSPC and transient absorption studies have been performed to understand the electron transfer and charge recombination dynamics from the $S_1$ state of the dye-NR systems. A two-step electron injection has been observed. An ultrafast (< 300 fs) hot electron injection from the higher vibrational levels of $S_1$ state to $TiO_2$ nanorods has been observed in addition to a slower electron injection in the range of 96-354 ps is observed. Bleach recovery of the dye-NR systems shows that a fast back electron transfer phenomena is also present in the time scales of 4-68 ps. This study shows that efficient charge separation before the charge recombination and other undesired pathways is evident in the studied phenothiazine porphyrin dye in the presence of semiconductor $TiO_2$ nanorods. In addition, tunability of electron injection and back electron transfer rates is observed with different spacers between porphyrin and phenothiazine moieties.

# 7 Conclusions and future directions

Ultrafast charge carrier relaxation dynamics in noble metal nanoparticles and quantum dots have been of immense interest to material scientists around the world due to their wide range of applications. While surface plasmon resonance of various metal nanoparticles and exciton dynamics in quantum dots are well studied, considerable interest has been generated to study the ultrafast dynamics in controlled metal nanoparticle assemblies, metal-semiconductor heterostructures and nanoparticle-dye conjugates. In the present thesis we try to focus on understanding of hot electron relaxation dynamics in these systems.

Third chapter focusses on hot electron relaxation dynamics in GNP dimers and trimers, prepared by self-assembly using a dithiol linker. Surface modification of MNPs with these linker molecules yields functional assemblies. Such MNP assemblies can also be prepared using DNA linkers, but interparticle distances are invariably significantly larger, and the nanoparticles significantly smaller in that case. With dithiol linkers, it is possible to obtain assemblies with small interparticle spacings and consequently, greater plasmon coupling. In the present study, dimers and trimers formed in the solution phase are further purified using gel electrophoresis. Understanding the electron relaxation dynamics in these systems can be exploited for optimizing the photochemical reactions and electron transfer reaction between metal semiconductor nanoparticles or molecular adsorbates. A plasmon coupled band in the extinction spectra of dimers and trimers is observed on the low energy side of the plasmon resonance resulting from longitudinal coupling of nanosphere assemblies. Traditional kinetic fits at the plasmon bleach maximum shows an enhanced electron-phonon coupling rate in trimers. Probing the kinetics at a chosen plasmon coupled maximum is difficult, due to significant overlap of plasmon bleach and excited state intraband excitation signals. This

disadvantage has been circumvented by employing global analysis. Hence, it has been established that electron-phonon and phonon-phonon coupling processes in dimers and trimers are faster than those in monomers . This is attributed to greater overlap of electron oscillation and phonon spectra in the regions of enhanced electric field known as hot spots in the assemblies. This shows that hot electron lifetime can be tuned in assembled nanoparticles which could potentially find application as saturable absorbers in optical switches and other optical devices.

Fourth chapter presents studies of electron transfer dynamics in cubic shaped PbS-Au heterostructures using transient absorption spectroscopy. We analyzed the electron transfer rates and charge relaxation dynamics from $1S_e$ and $1P_e$ states of conduction band from excited state absorption dynamics experiments from pump probe data. We followed the kinetic decay profiles of PbS and PbS-Au nanostructures. A fast 0.36 ps electron transfer component is observed from $1S_e$ level to gold and an ultrafast component faster than the instrument response function is observed from $1P_e$ level. This kind of ultrafast charge separation at the junction of the metal-semiconductor interface before Auger recombination and other relaxation channels is very crucial for the development of solar cells where multiple charge carriers created from the MEG can be extracted efficiently leading to overcome Shockley-Queisser limit.

Fifth chapter presents ultrafast charge relaxation dynamics in CZTS-Au nano heterostructures at different pump fluence energies. Broad absorbance is observed for CZTS nanostructures in the entire visible region. Pump probe data of the transient absorption spectroscopy shows photoinduced absorption in the entire probe region suggests the domination of excited state absorption over ground state bleach. Excited state dynamics of CZTS NRs reveal a very fast hot electron trapping process within 0.4 ps followed by 1 ps cold electron trapping and finally 40 ps component corresponding to the non-radiative recombination. Transient absorption

spectra in CZTS-Au nanostructures resulted in reduction of the optical density of the ESA suggesting an ultrafast charge transfer faster than the hot electron trapping process and within the instrument response function (200 fs). This ultrafast charge transfer process faster than the trapping process is crucial in optimizing the CZTS based nanostructures in photovoltaic applications.

In the final chapter we have designed a $A_3B$ porphyrin sensitizer in which the three meso-positions were decorated with three phenothiazine moieties tethered to porphyrin core, and the other meso-position is functionalized with phenyl carboxylic acid which can play a dual role as acceptor and anchoring group. A series of phenothiazine-porphyrin systems in which phenothiazine tethered to porphyrin with different linkages such as phenyl, alkynyl, and phenoxyl alkyl linkages and carboxylic acid anchoring group to attach to the semiconductor nanoparticles such as $TiO_2$ and the efficiency of photo-induced electron transfer and the solar energy conversion to electricity w.r.t. linker sizes were investigated. More importantly, Here phenothiazine not only acts as a chromophore that can absorb light from 200 – 350 nm but also behaves as a secondary (sacrificial electron donor) or p-type material, and decrease the rate of charge recombination, which thereby, increases the lifetime of the charge separated state necessary for the light capture. Fluorescence quenching studies reveal that maximum quenching of the fluorescence occurs at 1:1 dye to nanoparticle ratio. TCSPC and transient absorption studies have been performed to understand the electron transfer and charge recombination dynamics from the $S_1$ state of the dye-nanoparticle systems. A two-step electron injection has been observed. An ultrafast (< 300 fs) hot electron injection from the higher vibrational levels of $S_1$ state to $TiO_2$ nanorods has been observed in addition to a slower electron injection in the range of 96-354 ps is observed. Bleach recovery of the dye-nanoparticle systems shows that a fast back electron transfer phenomena is also present in the time scales of 4-68 ps. This study shows that efficient charge separation before the charge recombination

and other undesired pathways is evident in the studied phenothiazine porphyrin dye in the presence of semiconductor $TiO_2$ nanorods. In addition, tunability of electron injection and back electron transfer rates is observed with different spacers between porphyrin and phenothiazine moieties.

## 7.1 Future directions

To increase the stability of the separated dimers, silica coating on these dimers is employed using stober's method. Preliminary results (Figure 7.1) have shown a good silica encapsulation of dimers. The yield of separated silica coated dimers were found to be around 75%. Further studies to encapsulate trimers is underway. Silica coated gold nanoparticle assemblies would be more robust to perform ultrafast transient absorption studies. In addition, studying the ultrafast dynamics of single particles of the encapsulated assemblies would uncover the individual properties much better than ensemble studies.

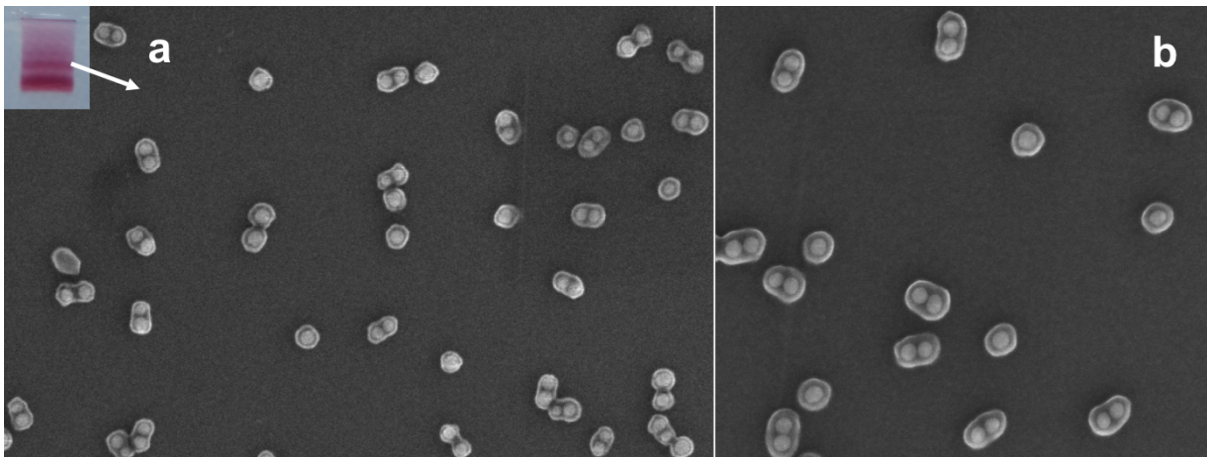


Figure 7.1. SEM images of (a,b) Silica coated gold nanodimers.

Photo conversion efficiency (PCE) of CZTS-Au, cubic PbS-Au, Dye-nanoparticle conjugates is still limited in our work due to several reasons such as limited state of the art facilities. Such studies would give us a complete picture in terms of application of these systems. Synthetic

modification of the surface of the synthesized CZTS rods and bare PbS to improve the quantum yield would be interesting as we observed a negligible photoluminescence from these samples. Starting with better quantum dots before growing metal structures on it would have huge effect in reducing the non-radiative channels thereby improving the better charge separation and PCE.

# Appendix

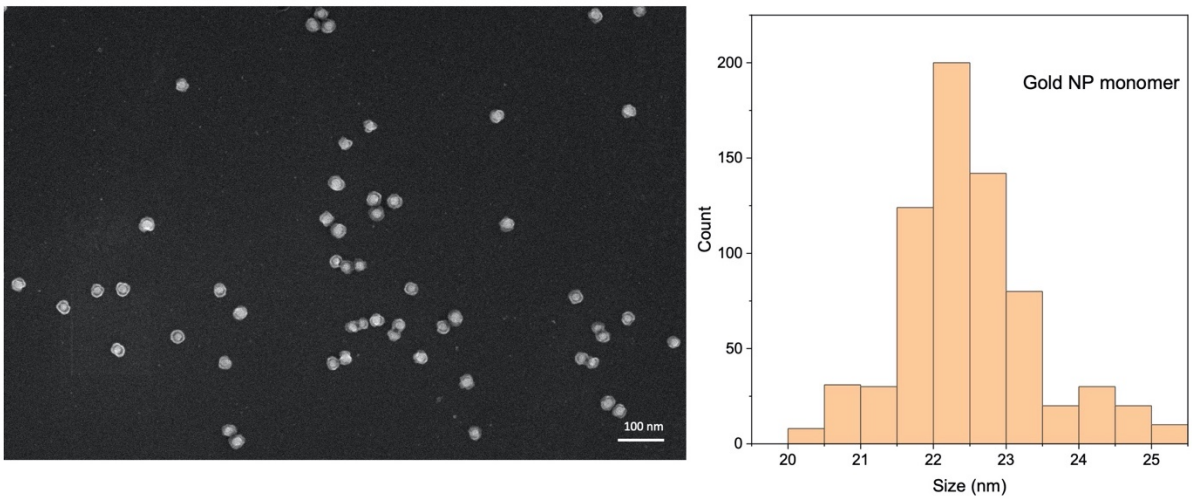


**Fig. A1**. SEM data of synthesized gold nanoparticle monomers in silica (left), Histogram of the size distribution analysis of gold monomer NPs (right) showing average size of 22 nm.

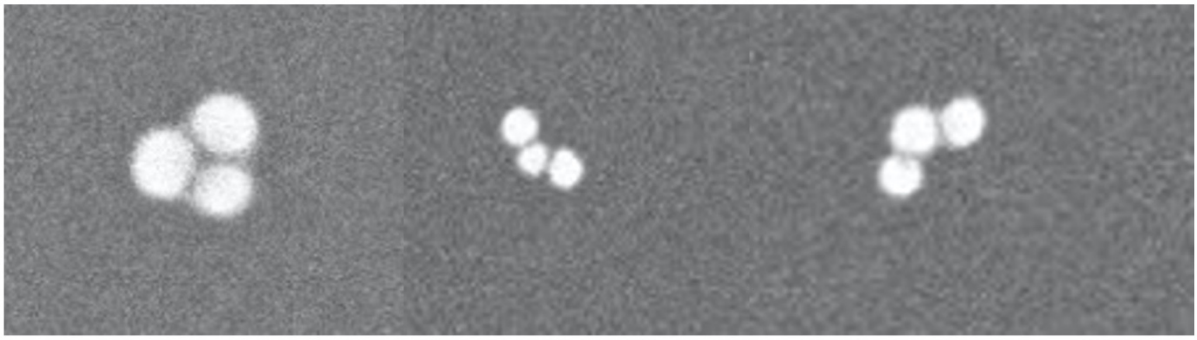

**Fig. A2**. SEM data of gold nanoparticle trimers of different orientations.

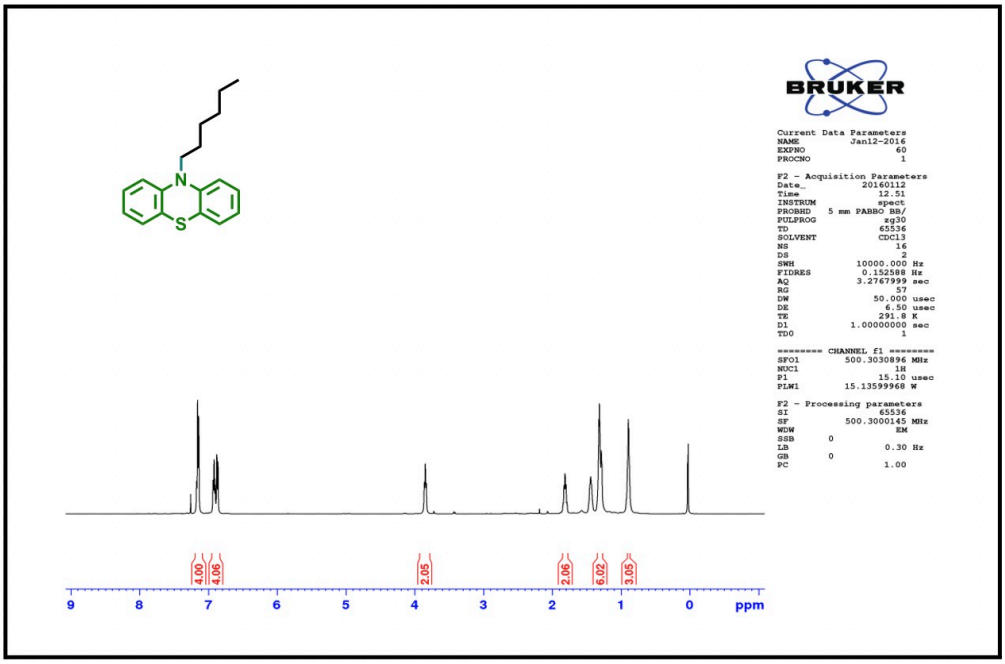


**Fig. A3.**[1]H NMR spectrum of 10-hexyl-10H-phenothiazine (**2.1**) in $CDCl_3$.

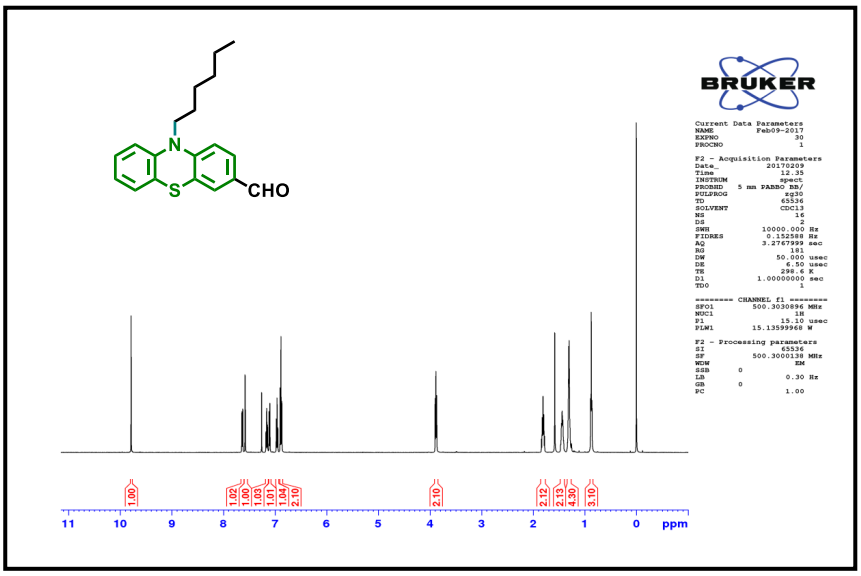


**Fig. A4.**[1]H NMR spectrum of 10-hexyl-10H-phenothiazine-3-carbaldehyde (**2.2**) in $CDCl_3$.

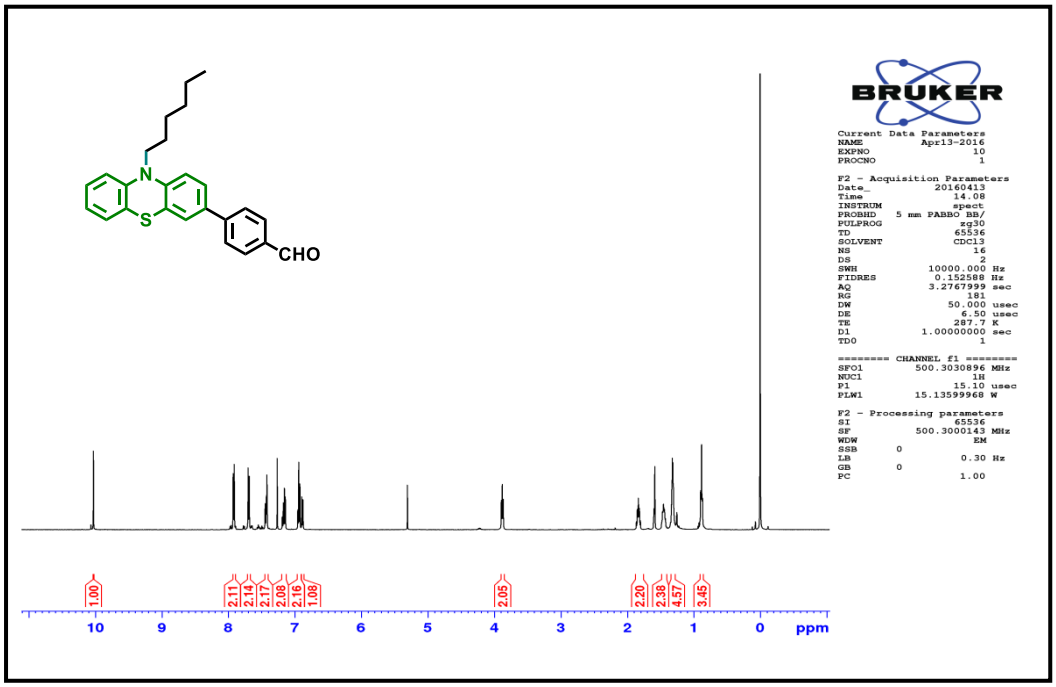


**Fig. A5.** $^{1}$H NMR spectrum of 4-(10-hexyl-10H-phenothiazin-3-yl)benzaldehyde (2.4) in $CDCl_3$

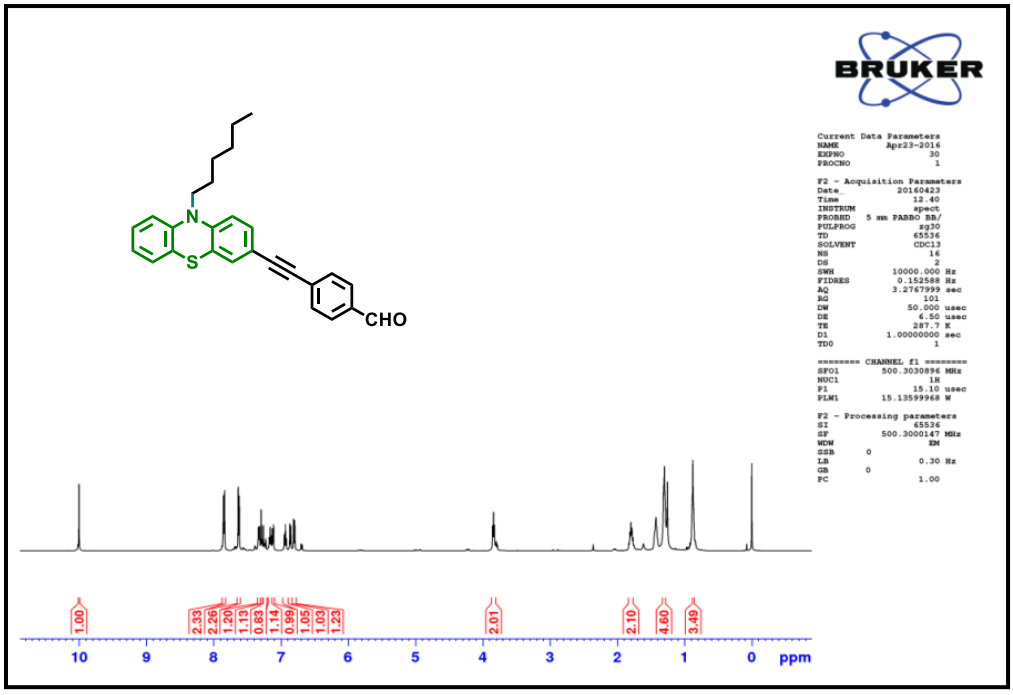


**Fig. A6.** $^{1}$H NMR spectrum of 4-((10-hexyl-10H-phenothiazin-3-yl)ethynyl)benzaldehyde (2.5) in $CDCl_3$.

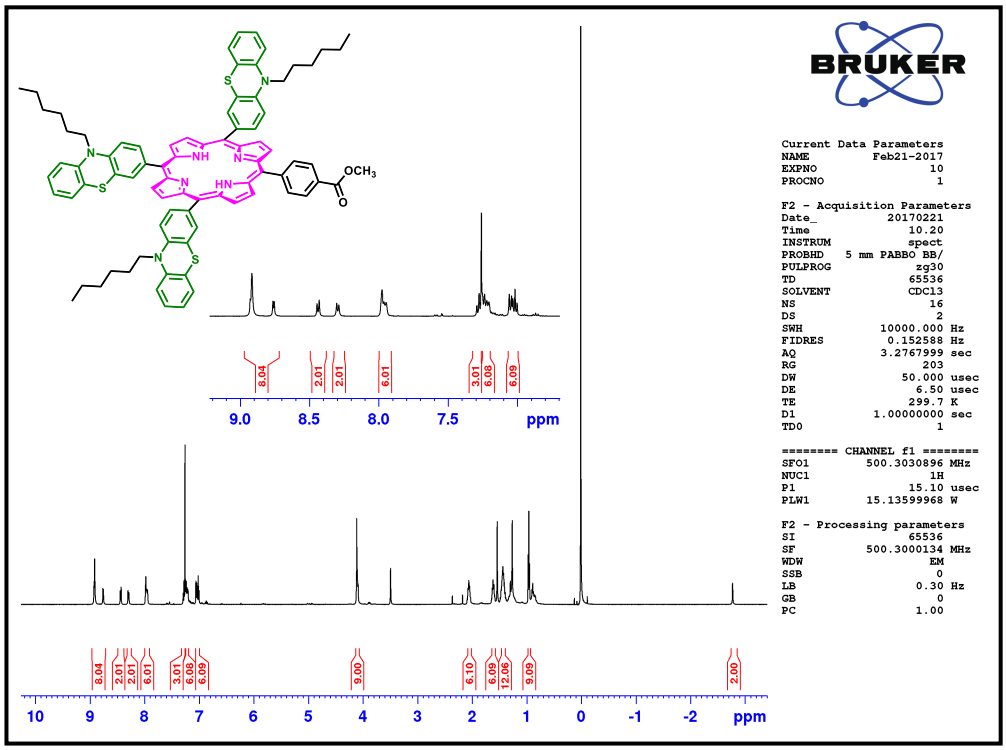


**Fig. A7.** $^{1}$H NMR spectrum of $H_2$-5-(p-methoxycarbonylphenyl)-10,15,20-tris(10-hexyl-10H-phenothiazin-3-yl)porphyrin $(PTZ)_3$-$H_2PCOOMe$, in $CDCl_3$

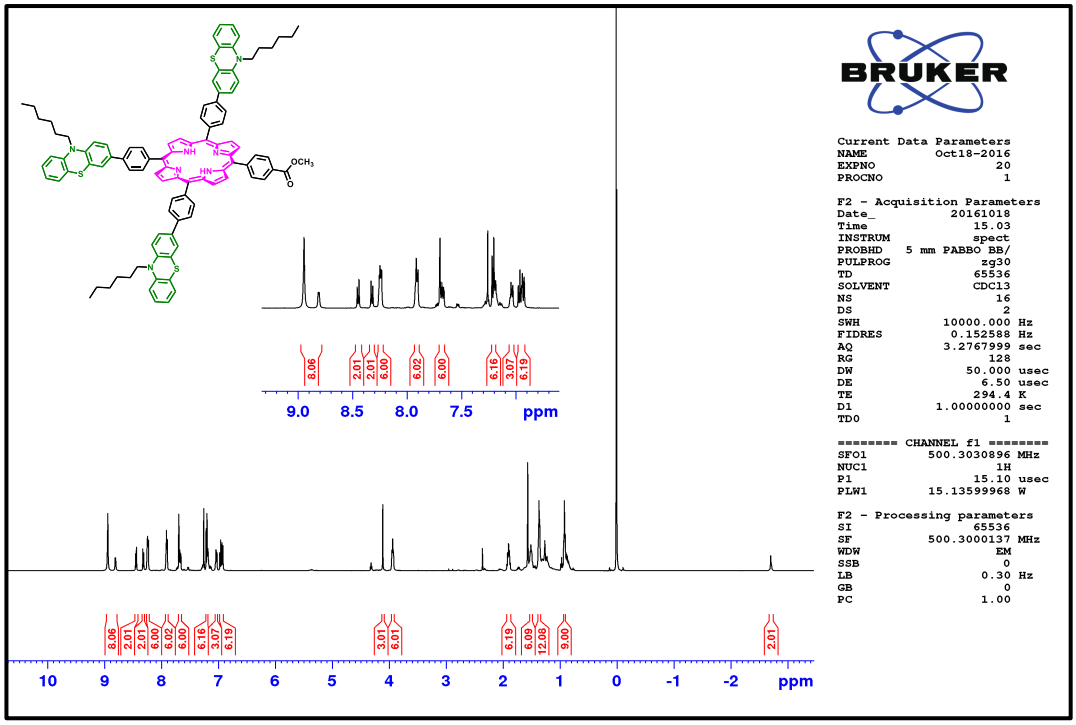


**Fig. A8.** $^{1}$H NMR spectrum of $H_2$-5-(p-methoxycarbonylphenyl)-10,15,20-tris(10-hexyl-10H-phenothiazin-3-yl) phenyl porphyrin (PTZ-Ph)$_3$-$H_2$PCOOMe in $CDCl_3$.

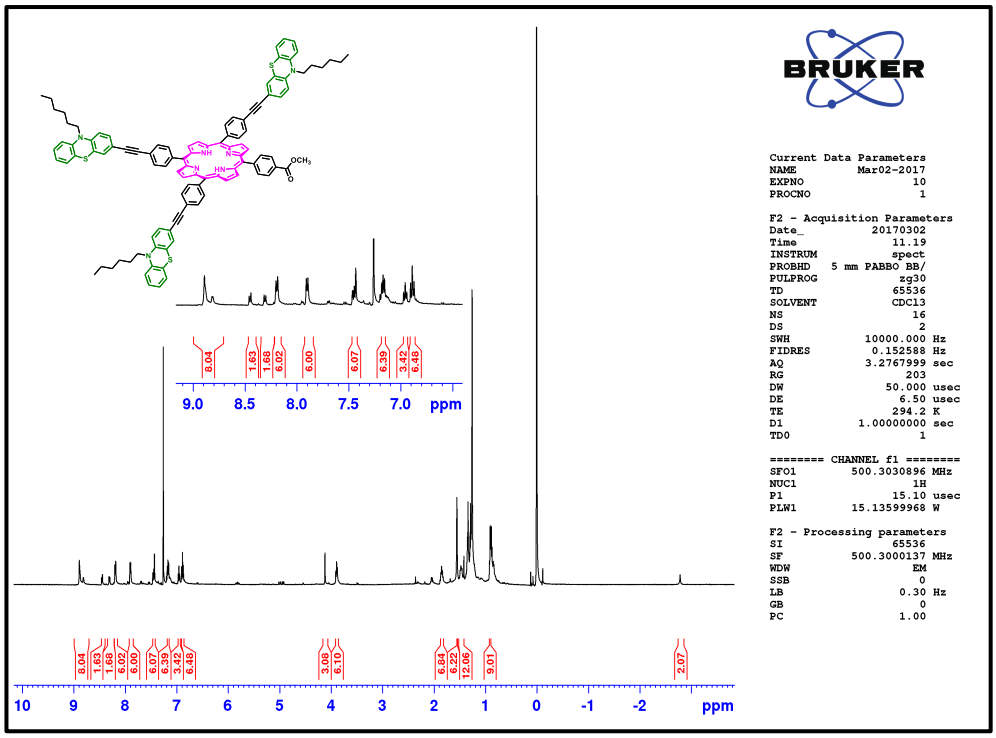


**Fig. A9.** $^{1}$H NMR spectrum of $H_2$-5-(p-methoxycarbonylphenyl)-10,15,20-tris(10-hexyl-10H-phenothiazin-3-yl)phenyl acetylene porphyrin (PTZ-PhAc)$_3$-$H_2$PCOOMe in $CDCl_3$.

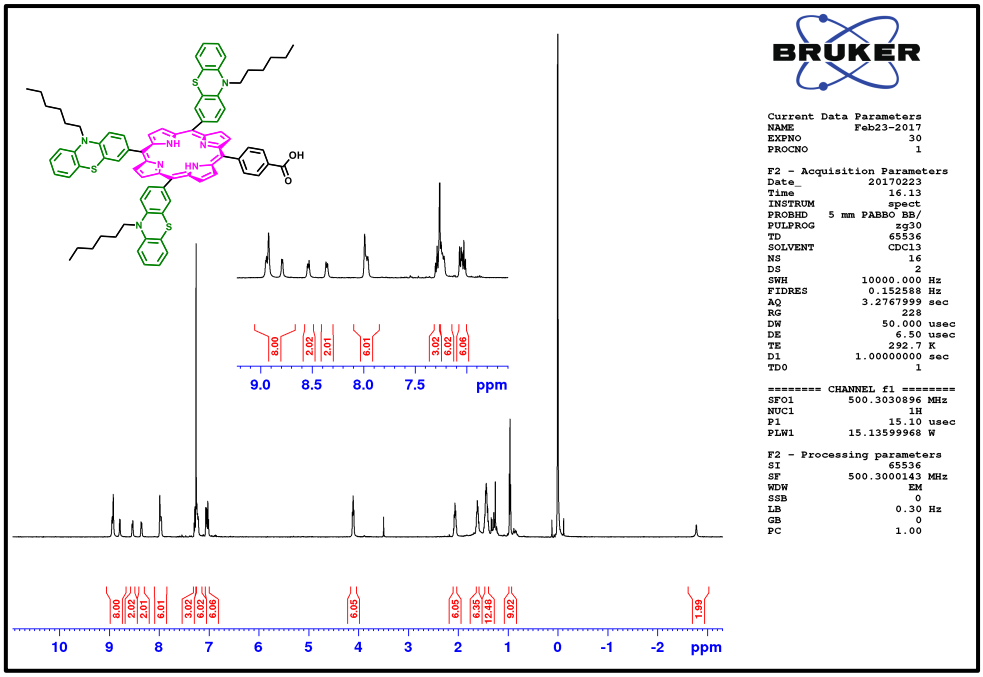


**Fig. A10.** $^{1}$H NMR spectrum of $H_2$-5-(4-Carboxyphenyl)-10,15,20-tris(10-hexyl-10H-phenothiazin-3-yl) porphyrin **(2.7)** $(PTZ)_3$-$H_2PCOOH$ ,in $CDCl_3$.

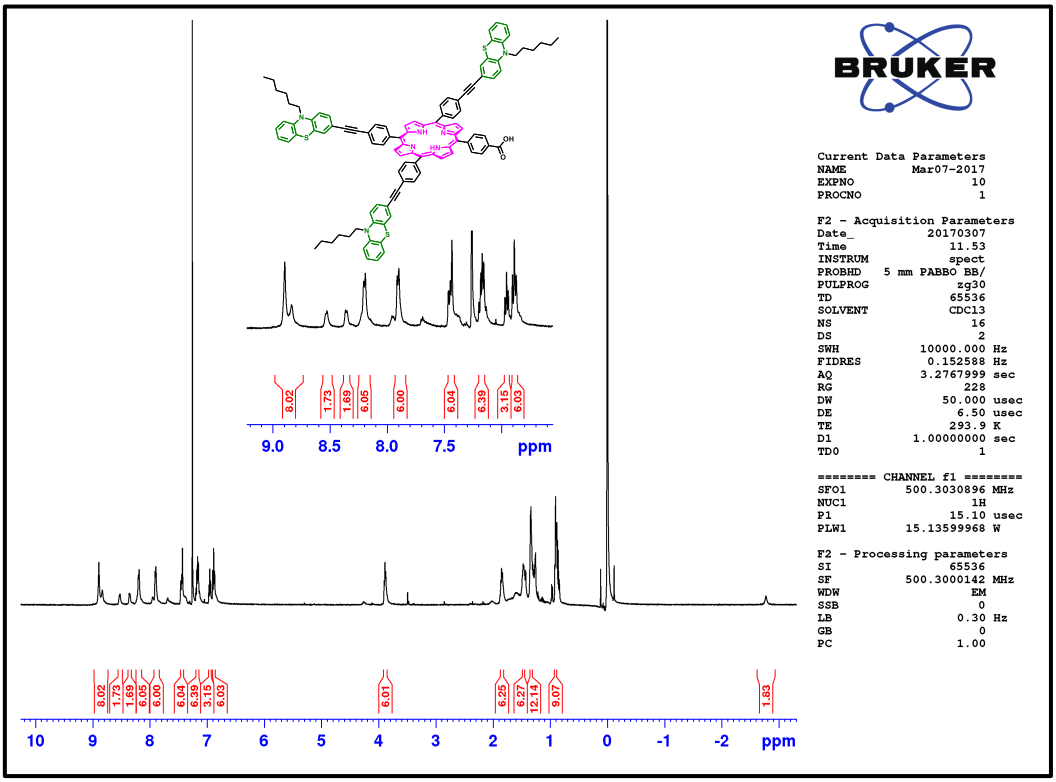


**Fig. A11.** $^{1}$H NMR spectrum of $H_2$-5-(4-Carboxyphenyl)-10,15,20-tris(10-hexyl-10H-phenothiazin-3-yl) phenyl acetylene porphyrin **(2.11)** $(PTZ\text{-}PhAc)_3$-$H_2PCOOH$ in $CDCl_3$.

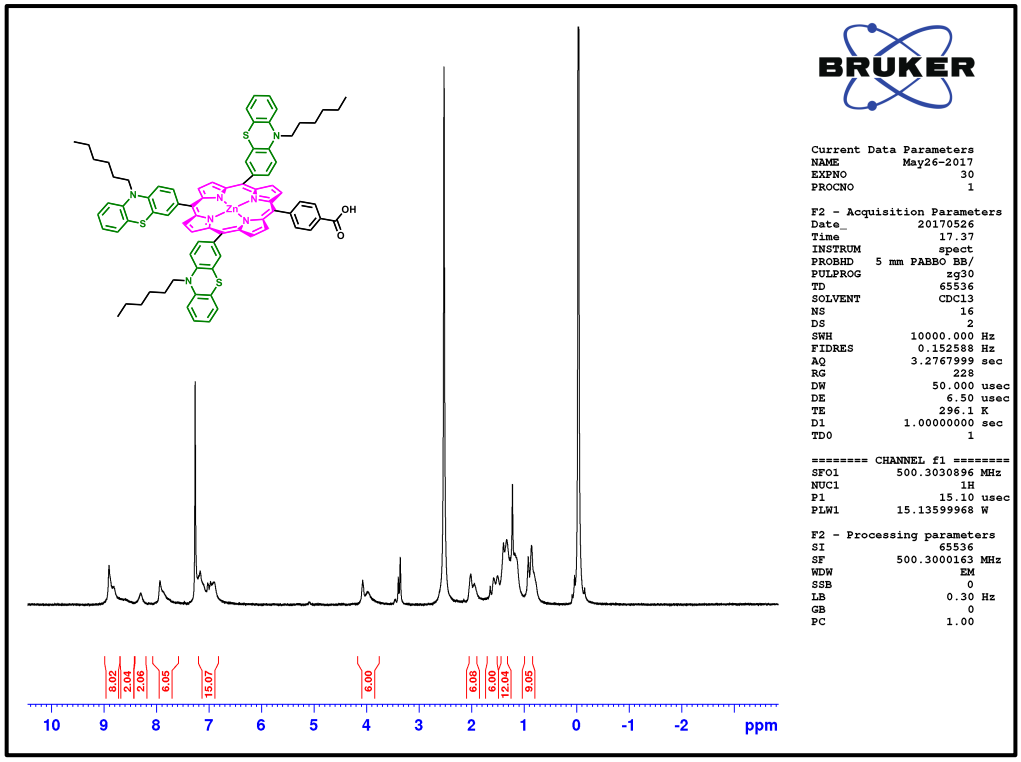


**Fig. A12.** [1]H NMR spectrum of 5-(4-Carboxyphenyl)-10,15,20-tris(10-hexyl-10H-phenothiazin-3-yl) porphyrinato zinc (II) **(2.8)** $(PTZ)_3$-ZnPCOOH,in $CDCl_3$.

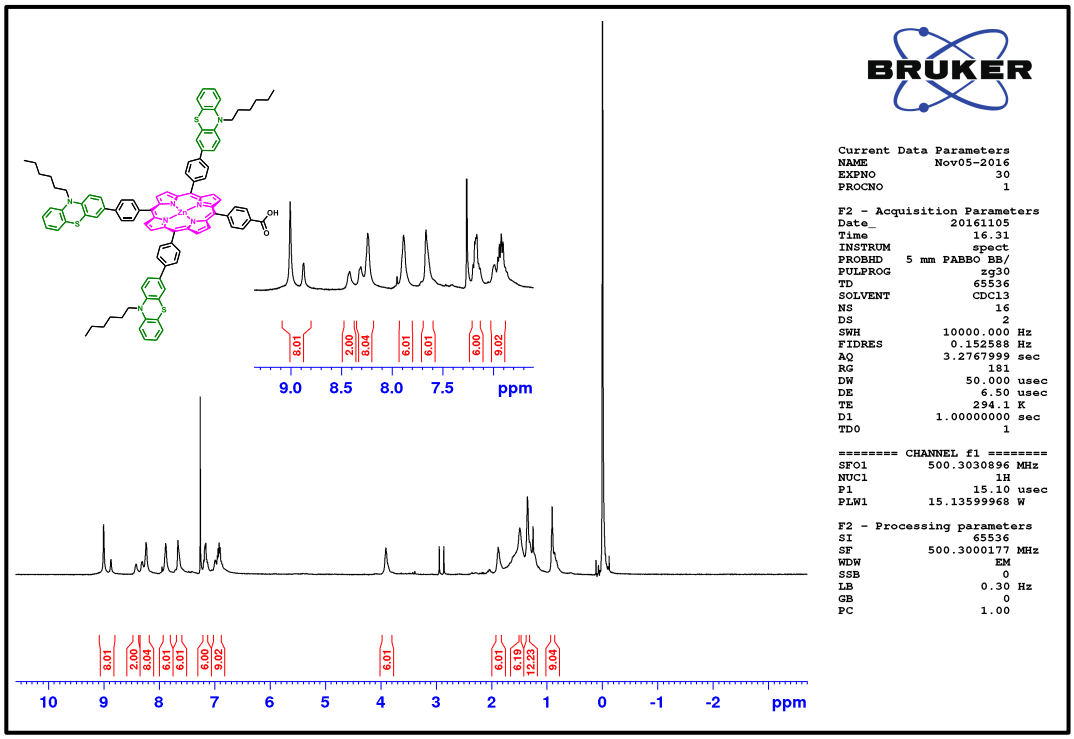


**Fig. A13 .** [1]H NMR spectrum of 5-(4-Carboxyphenyl)-10,15,20-tris(10-hexyl-10H-phenothiazin-3-yl) phenyl porphyrinato zinc (II) **(2.10)** $(PTZ\text{-}Ph)_3$-ZnPCOOH, in $CDCl_3$

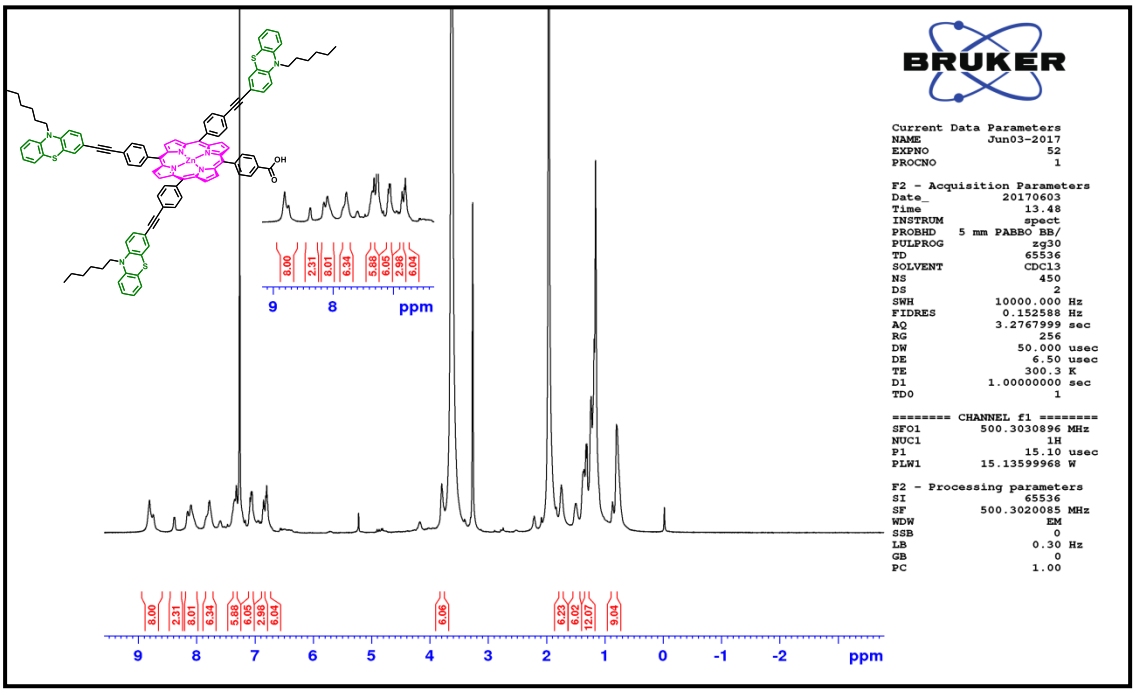


**Fig. A14 .** $^{1}$H NMR spectrum of 5-(4-Carboxyphenyl)-10,15,20-tris(10-hexyl-10H-phenothiazin-3-yl) phenyl porphyrinato zinc (II) **(2.12)** (PTZ-PhAc)$_3$-ZnPCOOH, in $CDCl_3$

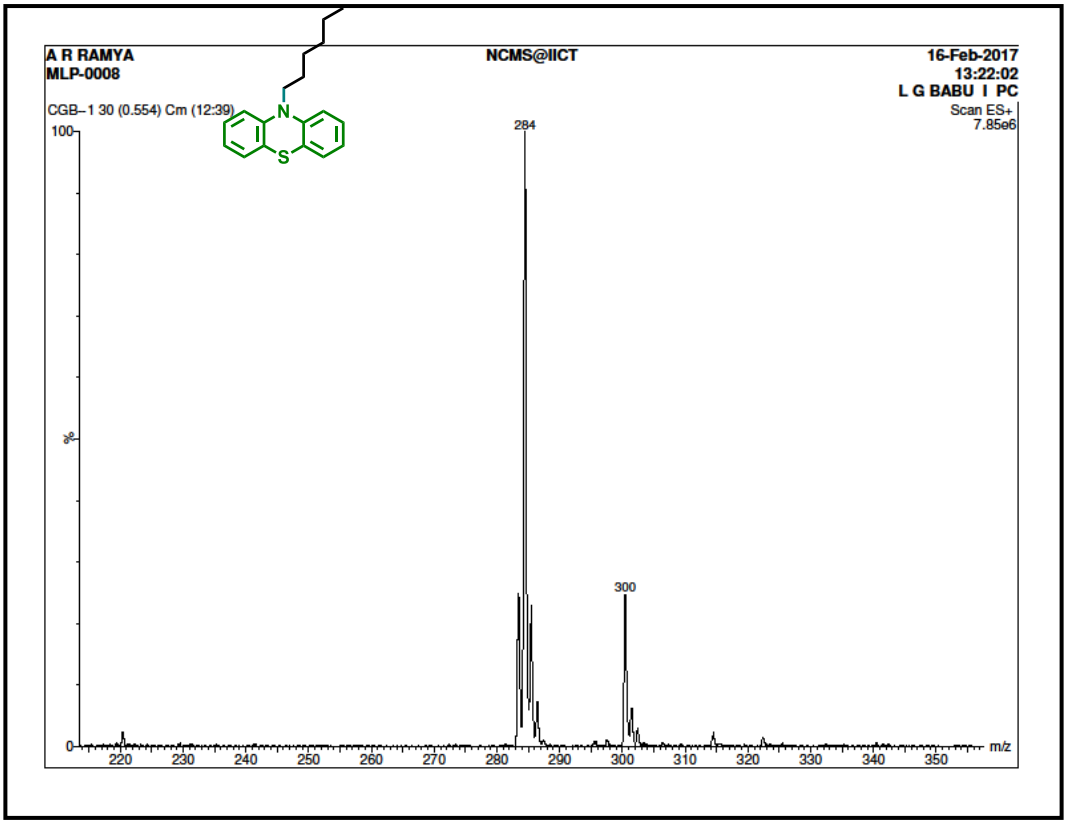


**Fig. A15.** HRMS (ESI+) spectrum of 10-hexyl-10H-phenothiazine (**2.1**) in $CHCl_3$**.**

.

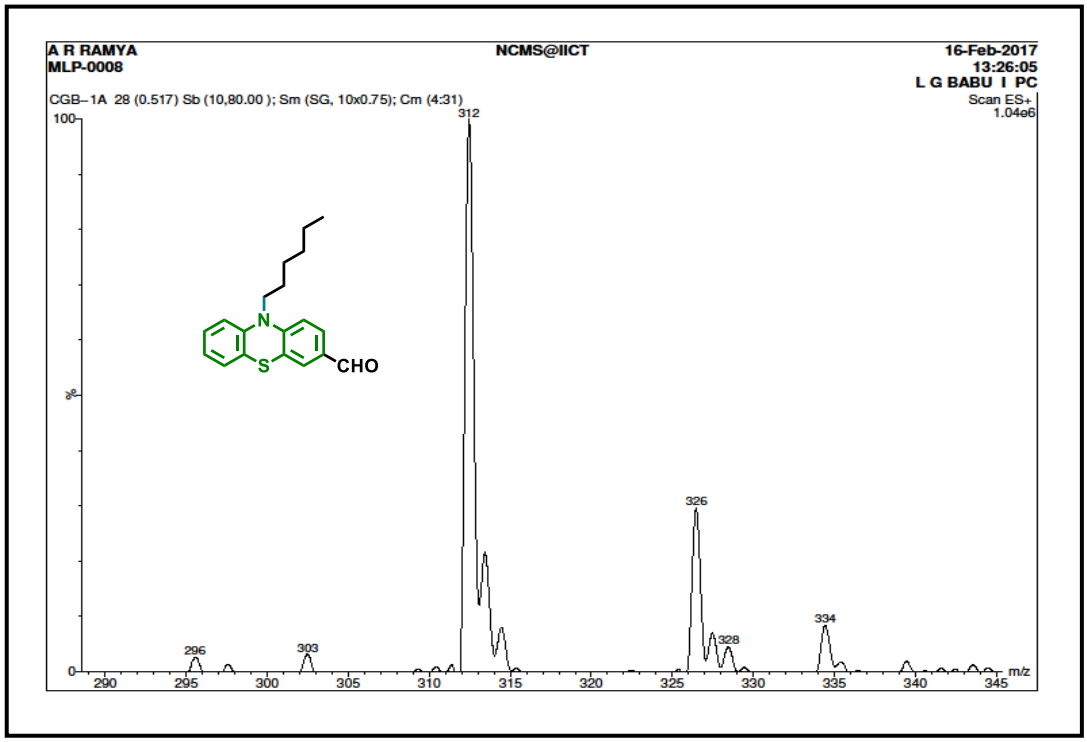


**Fig. A16**. HRMS (ESI+) spectrum of10-hexyl-10H-phenothiazine-3-carbaldehyde (**2.2**) in $CHCl_3$

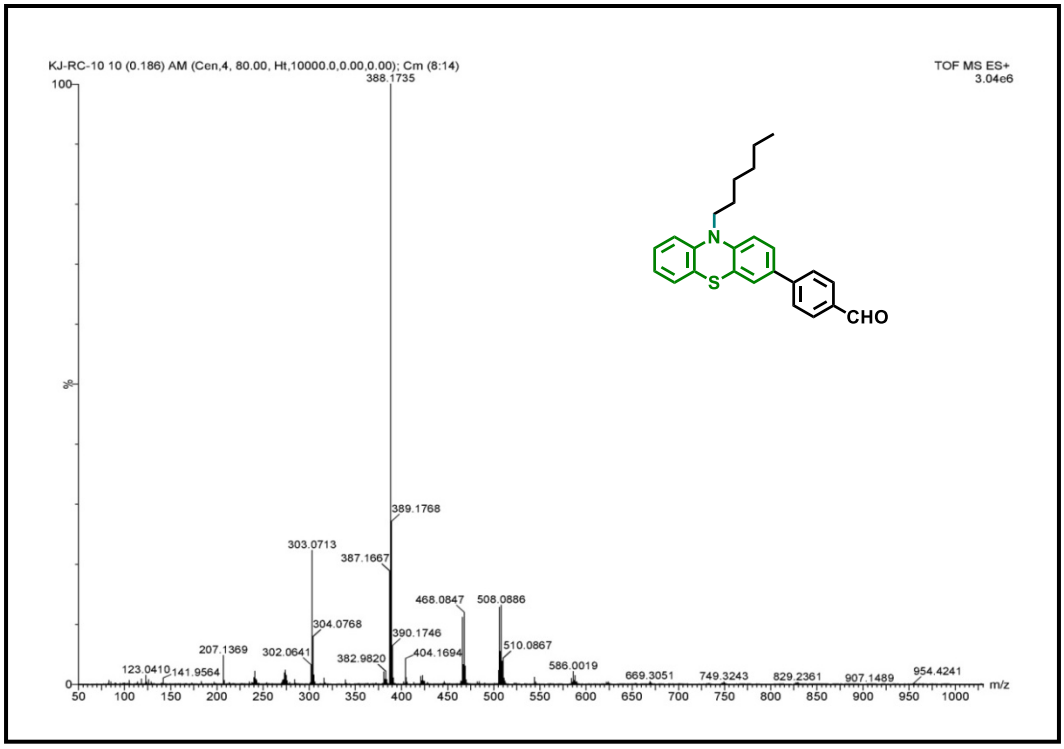


**Fig. A17.** HRMS (ESI+) spectrum of 4-(10-hexyl-10H-phenothiazin-3-yl)benzaldehyde (**2.4**) in $CHCl_3$.

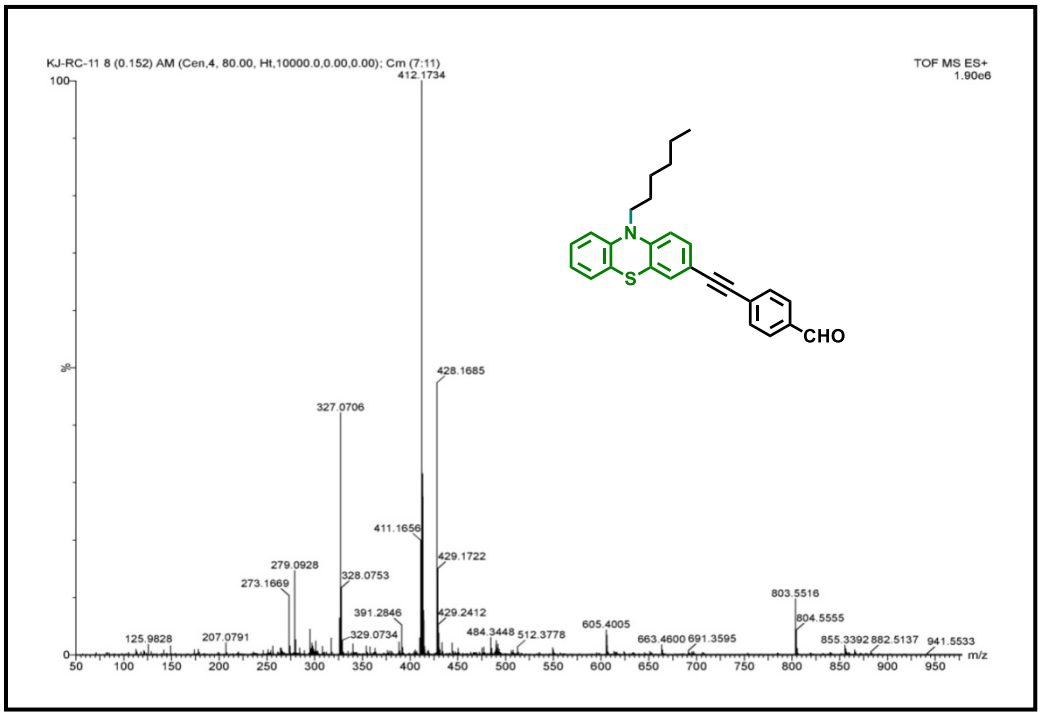


**Fig. A18.** HRMS (ESI+) spectrum of 4-((10-hexyl-10H-phenothiazin-3-yl)ethynyl)benzaldehyde (**2.5**) in $CHCl_3$.

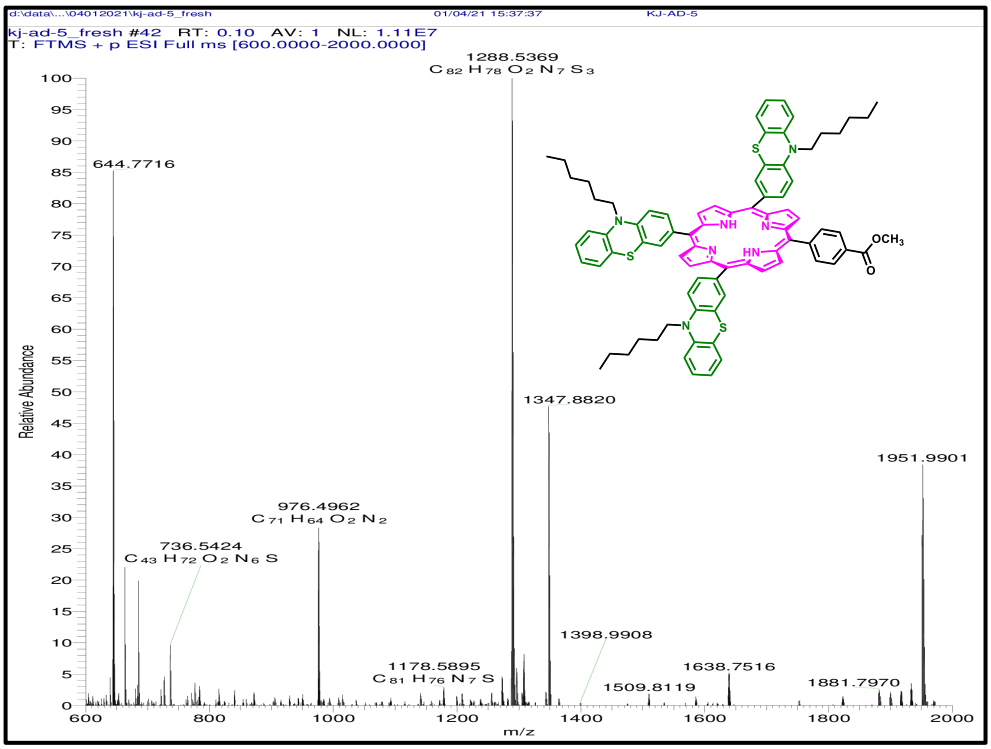


**Fig. A19.** HRMS (ESI+) spectrum of $H_2$-5-(p-methoxycarbonylphenyl)-10,15,20-tris(10-hexyl-10H-phenothiazin-3-yl)porphyrin (PTZ)$_3$-$H_2$PCOOMe, in $CHCl_3$

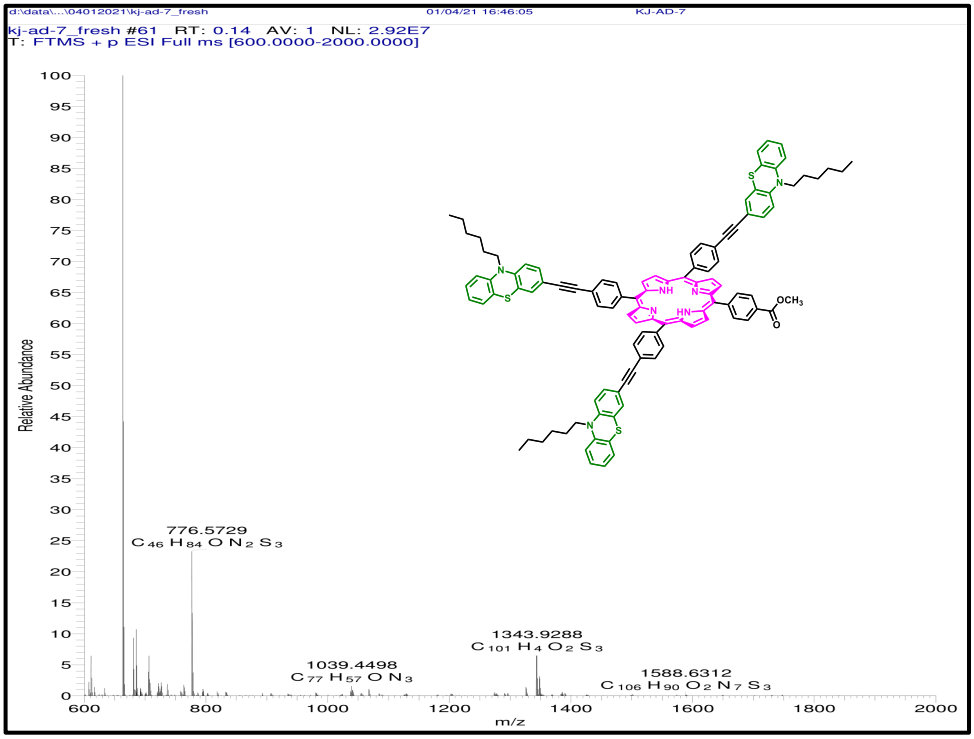


**Fig. A20.** HRMS (ESI+) spectrum of $H_2$-5-(p-methoxycarbonylphenyl)-10,15,20-tris(10-hexyl-10H-phenothiazin-3-yl)phenyl acetylene porphyrin (PTZ-PhAc)$_3$-$H_2$PCOOMe in $CHCl_3$.

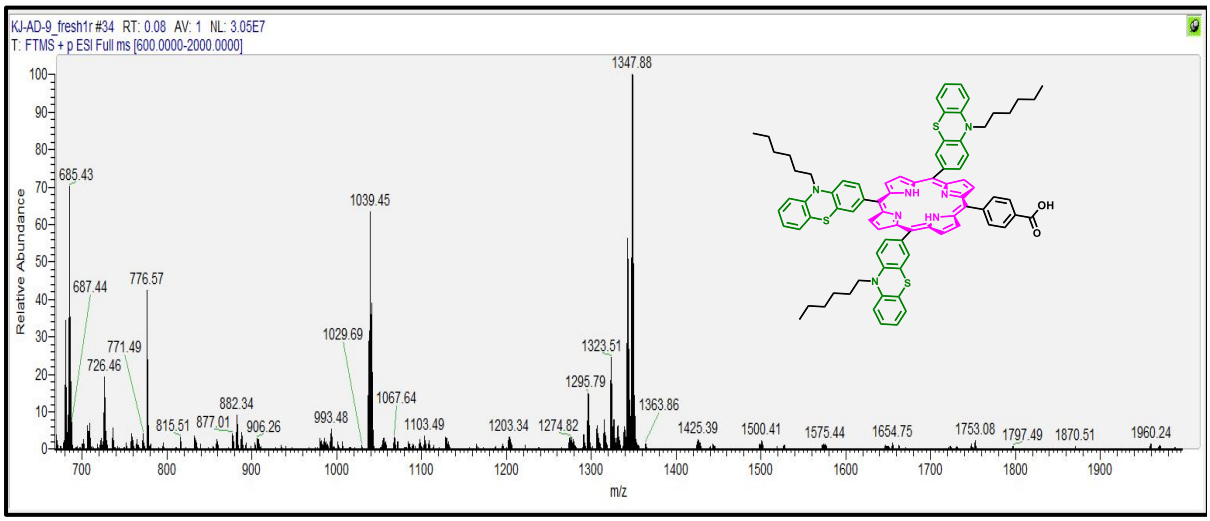


**Fig. A21.** HRMS (ESI+) spectrum of $H_2$-5-(4-Carboxyphenyl)-10,15,20-tris(10-hexyl-10H-phenothiazin-3-yl) porphyrin **(2.7)** (PTZ)$_3$-$H_2$PCOOH ,in $CHCl_3$.

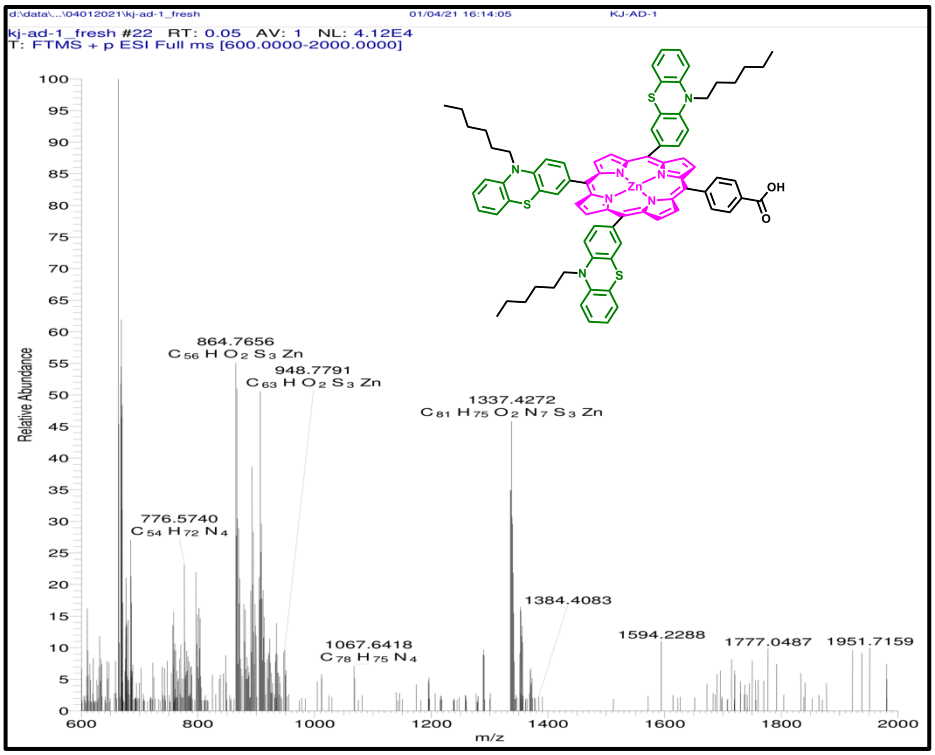


**Fig. A22.** HRMS (ESI+) spectrum of 5-(4-Carboxyphenyl)-10,15,20-tris(10-hexyl-10H-phenothiazin-3-yl) porphyrinato zinc (II) **(2.8)**$(PTZ)_3$-ZnPCOOH,in $CHCl_3$.

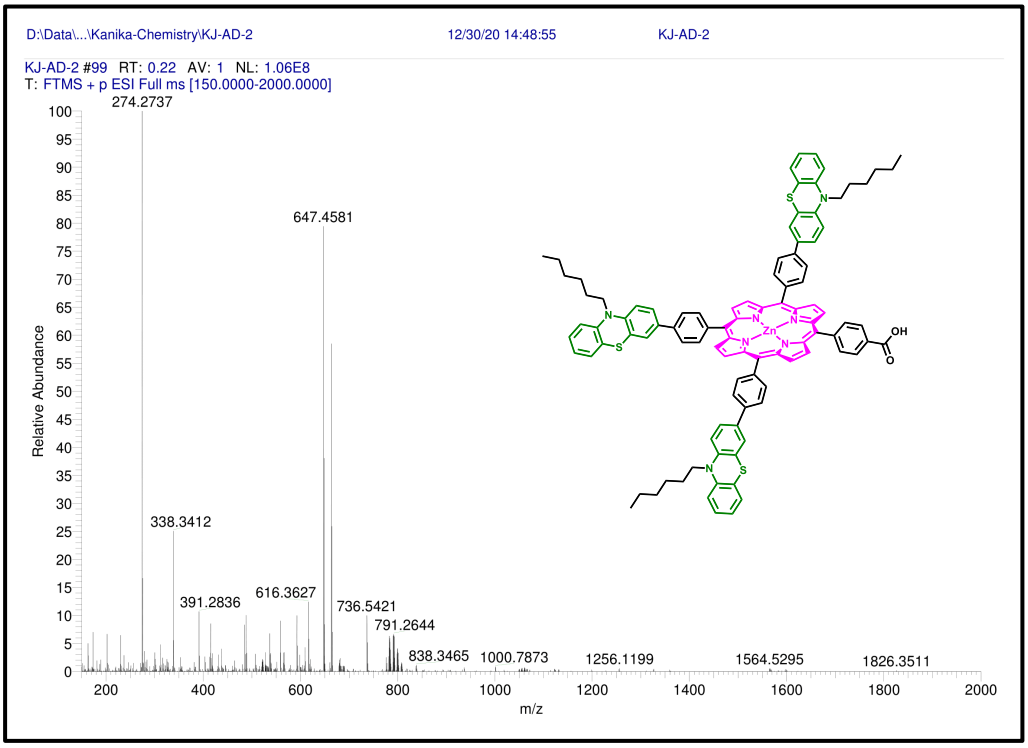


**Fig. A23.** HRMS (ESI+) spectrum of -(4-Carboxyphenyl)-10,15,20-tris(10-hexyl-10H-phenothiazin-3-yl) phenyl porphyrinato zinc (II) **(2.10)**$(PTZ\text{-}Ph)_3$-ZnPCOOH in $CHCl_3$.

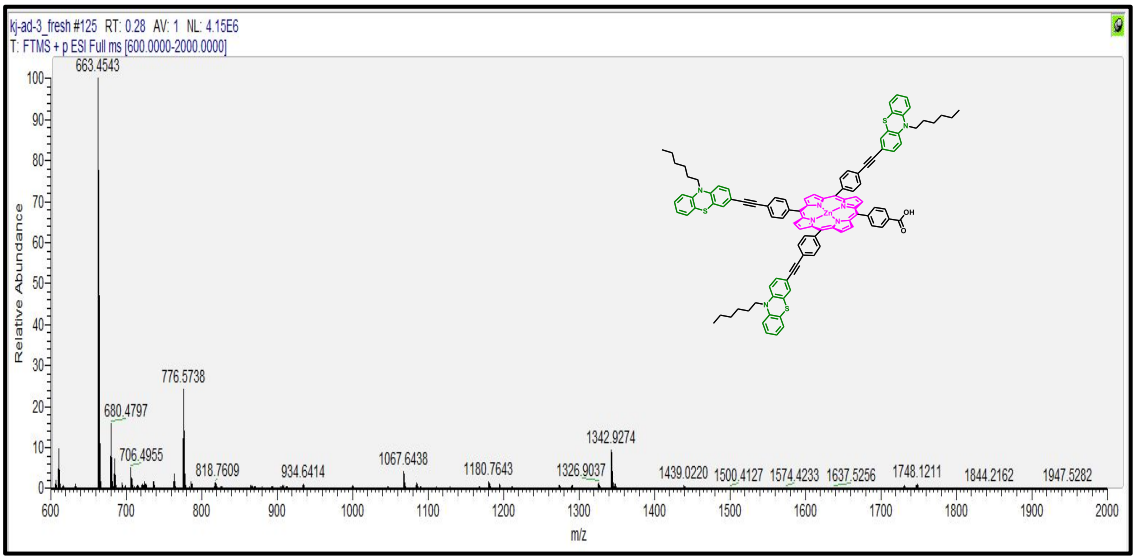


**Fig. A24.** HRMS (ESI+) spectrum of -(4-Carboxyphenyl)-10,15,20-tris(10-hexyl-10H-phenothiazin-3-yl) phenyl porphyrinato zinc (II) **(2.12)**(PTZ-PhAc)$_3$-ZnPCOOH in $CHCl_3$.

*(Note: NMR and mass data is recorded by Dr. Kanika Jain (credit))*

# 8 References


(1) Xia, Y.; Xiong, Y.; Lim, B.; Skrabalak, S. E. Shape-Controlled Synthesis of Metal Nanocrystals: Simple Chemistry Meets Complex Physics? *Angew. Chemie - Int. Ed.* **2009**, *48*, 60–103.

(2) Link, S.; El-Sayed, M. A. Optical Properties and Ultrafast Dynamics of Metallic Nanocrystals. *Annu. Rev. Phys. Chem.* **2003**, *54*, 331–366.

(3) Willets, K. A.; Van Duyne, R. P. Localized Surface Plasmon Resonance Spectroscopy and Sensing. *Annu. Rev. Phys. Chem.* **2007**, *58*, 267–297.

(4) Garcia, M. A. Surface Plasmons in Metallic Nanoparticles: Fundamentals and Applications. *Journal of Physics D: Applied Physics*. 2011, p 283001.

(5) Mooradian, A. Photoluminescence of Metals. *Phys. Rev. Lett.* **1969**, *22*, 185–187.

(6) Dynich, R. A.; Ponyavina, A. N. Effect of Metallic Nanoparticle Sizes on the Local Field near Their Surface. *J. Appl. Spectrosc.* **2008**, *75*, 832–838.

(7) Kelly, K. L.; Coronado, E.; Zhao, L. L.; Schatz, G. C. The Optical Properties of Metal Nanoparticles: The Influence of Size, Shape, and Dielectric Environment. *J. Phys. Chem. B* **2003**, *107*, 668–677.

(8) Mulvaney, P. Surface Plasmon Spectroscopy of Nanosized Metal Particles. *Langmuir* **1996**, *12*, 788–800.

(9) Huber, E.; Frost, M. *Light Scattering by Small Particles*; Dover: New York, 1998; Vol. 47.

(10) Müller, H. *Optical Properties of Metal Clusters*, vol 25.; Springer Series in Material Science, 1996; Vol. 194.

(11) Bohren, C. F. *Absorption and Scattering of Light by Small Particles*; Wiley-Interscience: New York, 1983.

(12) Rogalski, M. S.; Palmer, S. B. *Solid State Physics*; Holt, Rinehart & Winston: New York, 2014.

(13) Kittel, C.; Holcomb, D. F. *Introduction to Solid State Physics*; Wiley: Hoboken, NJ, 1967; Vol. 35.

(14) Kraus, W. A.; Schatz, G. C. Plasmon Resonance Broadening in Small Metal Particles. *J. Chem. Phys.* **1983**, *79*, 6130–6139.

(15) Genzel, L.; Martin, T. P.; Kreibig, U. Dielectric Function and Plasma Resonances of Small Metal Particles. *Zeitschrift für Phys. B Condens. Matter Quanta* **1975**, *21*, 339–346.

(16) Coronado, E. A.; Schatz, G. C. Surface Plasmon Broadening for Arbitrary Shape Nanoparticles: A Geometrical Probability Approach. *J. Chem. Phys.* **2003**, *119*, 3926–3934.

(17) Kreibig, U.; Genzel, L. Optical Absorption of Small Metallic Particles. *Surf. Sci.* **1985**, *156*,

678–700.

(18) Liu, M.; Guyot-Sionnest, P. Synthesis and Optical Characterization of Au/Ag Core/Shell Nanorods. *J. Phys. Chem. B* **2004**, *108*, 5882–5888.

(19) Johnson, P. B.; Christy, R. W. Optical Constants of the Noble Metals. *Phys. Rev. B* **1972**, *6*, 4370–4379.

(20) Alvarez, M. M.; Khoury, J. T.; Schaaff, T. G.; Shafigullin, M. N.; Vezmar, I.; Whetten, R. L. Optical Absorption Spectra of Nanocrystal Gold Molecules. *J. Phys. Chem. B* **1997**, *101*, 3706–3712.

(21) Ehrenreich, H.; Philipp, H. R. Optical Properties of Ag and Cu. *Phys. Rev.* **1962**, *128*, 1622–1629.

(22) Gans, R. Über Die Form Ultramikroskopischer Silberteilchen. *Ann. Phys.* **1915**, *352*, 270–284.

(23) Link, S.; Mohamed, M. B.; El-Sayed, M. A. Simulation of the Optical Absorption Spectra of Gold Nanorods as a Function of Their Aspect Ratio and the Effect of the Medium Dielectric Constant. *Journal of Physical Chemistry B*. 1999, pp 3073–3077.

(24) Prescott, S. W.; Mulvaney, P. Gold Nanorod Extinction Spectra. *J. Appl. Phys.* **2006**, *99*.

(25) Draine, B. T.; Flatau, P. J. Discrete-Dipole Approximation for Periodic Targets: Theory and Tests. *J. Opt. Soc. Am. A* **2008**, *25*, 2693.

(26) Draine, B. T.; Flatau, P. J. Discrete-Dipole Approximation For Scattering Calculations. *J. Opt. Soc. Am. A* **1994**, *11*, 1491.

(27) Jensen, T.; Kelly, L.; Lazarides, A.; Schatz, G. C. Electrodynamics of Noble Metal Nanoparticles and Nanoparticle Clusters. *J. Clust. Sci.* **1999**, *10*, 295–317.

(28) Hu, M.; Chen, J.; Li, Z. Y.; Au, L.; Hartland, G. V.; Li, X.; Marquez, M.; Xia, Y. Gold Nanostructures: Engineering Their Plasmonic Properties for Biomedical Applications. *Chem. Soc. Rev.* **2006**, *35*, 1084–1094.

(29) Eustis, S.; El-Sayed, M. A. Why Gold Nanoparticles Are More Precious than Pretty Gold: Noble Metal Surface Plasmon Resonance and Its Enhancement of the Radiative and Nonradiative Properties of Nanocrystals of Different Shapes. *Chem. Soc. Rev.* **2006**, *35*, 209–217.

(30) Hodak, J. H.; Henglein, A.; Hartland, G. V. Photophysics of Nanometer Sized Metal Particles: Electron-Phonon Coupling and Coherent Excitation of Breathing Vibrational Modes. *J. Phys. Chem. B* **2000**, *104*, 9954–9965.

(31) Link, S.; El-Sayed, M. A. Optical Properties and Ultrafast Dynamics of Metallic Nanocrystals. *Annu. Rev. Phys. Chem.* **2003**, *54*, 331–366.

(32) Dreaden, E. C.; Alkilany, A. M.; Huang, X.; Murphy, C. J.; El-Sayed, M. A. The Golden Age: Gold Nanoparticles for Biomedicine. *Chem. Soc. Rev.* **2012**, *41*, 2740–2779.

(33) Jain, P. K.; Eustis, S.; El-Sayed, M. A. Plasmon Coupling in Nanorod Assemblies: Optical Absorption, Discrete Dipole Approximation Simulation, and Exciton-Coupling Model. *J. Phys. Chem. B* **2006**, *110*, 18243–18253.

(34) Nordlander, P.; Oubre, C.; Prodan, E.; Li, K.; Stockman, M. I. Plasmon Hybridization in Nanoparticle Dimers. *Nano Lett.* **2004**, *4*, 899–903.

(35) Zuloaga, J.; Prodan, E.; Nordlander, P. Quantum Description of the Plasmon Resonances of a Nanoparticle Dimer. *Nano Lett.* **2009**, *9*, 887–891.

(36) Prodan, E.; Radloff, C.; Halas, N. J.; Nordlander, P. A Hybridization Model for the Plasmon Response of Complex Nanostructures. *Science (80-. ).* **2003**, *302*, 419–422.

(37) Oldenburg, S. J.; Averitt, R. D.; Westcott, S. L.; Halas, N. J. Nanoengineering of Optical Resonances. *Chem. Phys. Lett.* **1998**, *288*, 243–247.

(38) Aizpurua, J.; Bryant, G. W.; Richter, L. J.; García De Abajo, F. J.; Kelley, B. K.; Mallouk, T. Optical Properties of Coupled Metallic Nanorods for Field-Enhanced Spectroscopy. *Phys. Rev. B - Condens. Matter Mater. Phys.* **2005**, *71*.

(39) Yoon, J. H.; Selbach, F.; Langolf, L.; Schlücker, S. Ideal Dimers of Gold Nanospheres for Precision Plasmonics: Synthesis and Characterization at the Single-Particle Level for Identification of Higher Order Modes. *Small* **2018**, *14*, 1702754.

(40) Huang, J.; Zhang, L.; Chen, B.; Ji, N.; Chen, F.; Zhang, Y.; Zhang, Z. Nanocomposites of Size-Controlled Gold Nanoparticles and Graphene Oxide: Formation and Applications in SERS and Catalysis. *Nanoscale* **2010**, *2*, 2733–2738.

(41) Song, J.; Zhou, J.; Duan, H. Self-Assembled Plasmonic Vesicles of SERS-Encoded Amphiphilic Gold Nanoparticles for Cancer Cell Targeting and Traceable Intracellular Drug Delivery. *J. Am. Chem. Soc.* **2012**, *134*, 13458–13469.

(42) Xie, W.; Walkenfort, B.; Schlücker, S. Label-Free SERS Monitoring of Chemical Reactions Catalyzed by Small Gold Nanoparticles Using 3D Plasmonic Superstructures. *J. Am. Chem. Soc.* **2013**, *135*, 1657–1660.

(43) Ueno, K.; Juodkazis, S.; Mizeikis, V.; Sasaki, K.; Misawa, H. Clusters of Closely Spaced Gold Nanoparticles as a Source of Two-Photon Photoluminescence at Visible Wavelengths. *Adv. Mater.* **2008**, *20*, 26–30.

(44) Jung, Y.; Chen, H.; Tong, L.; Cheng, J. X. Imaging Gold Nanorods by Plasmon-Resonance-Enhanced Four Wave Mixing. *J. Phys. Chem. C* **2009**, *113*, 2657–2663.

(45) Danckwerts, M.; Novotny, L. Optical Frequency Mixing at Coupled Gold Nanoparticles. *Phys. Rev. Lett.* **2007**, *98*, 026104.

(46) Liu, X. Colloidal Plasmonic Nanoparticles for Ultrafast Optical Switching and Laser Pulse Generation. *Frontiers in Materials*. 2018.

(47) Hartland, G. V. Optical Studies of Dynamics in Noble Metal Nanostructures. *Chemical Reviews*. 2011, pp 3858–3887.

(48) Ganeev, R. A.; Tugushev, R. I.; Usmanov, T. Application of the Nonlinear Optical Properties of Platinum Nanoparticles for the Mode Locking of Nd:Glass Laser. *Appl. Phys. B Lasers Opt.* **2009**, *94*, 647–651.

(49) Voisin, C.; Fatti, N. Del; Christofilos, D.; Vallee, F. Ultrafast Electron Dynamics and Optical

Nonlinearities in Metal Nanoparticles. *J. Phys. Chem. B* **2001**, *105*, 2264–2280.

(50) Sun, C. K.; Vallée, F.; Acioli, L. H.; Ippen, E. P.; Fujimoto, J. G. Femtosecond-Tunable Measurement of Electron Thermalization in Gold. *Phys. Rev. B* **1994**, *50*, 15337–15348.

(51) Del Fatti, N.; Voisin, C.; Achermann, M.; Tzortzakis, S.; Christofilos, D.; Vallée, F. Nonequilibrium Electron Dynamics in Noble Metals. *Phys. Rev. B - Condens. Matter Mater. Phys.* **2000**, *61*, 16956–16966.

(52) Fann, W. S.; Storz, R.; Tom, H. W. K.; Bokor, J. Direct Measurement of Nonequilibrium Electron-Energy Distributions in Subpicosecond Laser-Heated Gold Films. *Phys. Rev. Lett.* **1992**, *68*, 2834–2837.

(53) Fann, W. S.; Storz, R.; Tom, H. W. K.; Bokor, J. Electron Thermalization in Gold. *Phys. Rev. B* **1992**, *46*, 13592–13595.

(54) Link, S.; Burda, C.; Mohamed, M.; Nikoobakht, B.; El-Sayed, M. Femtosecond Transient-Absorption Dynamics of Colloidal Gold Nanorods: Shape Independence of the Electron-Phonon Relaxation Time. *Phys. Rev. B - Condens. Matter Mater. Phys.* **2000**, *61*, 6086–6090.

(55) Link, S.; El-Sayed, M. A. Spectral Properties and Relaxation Dynamics of Surface Plasmon Electronic Oscillations in Gold and Silver Nanodots and Nanorods. *J. Phys. Chem. B* **1999**, *103*, 8410–8426.

(56) Eesley, G. L. Observation of Nonequilibrium Electron Heating in Copper. *Phys. Rev. Lett.* **1983**, *51*, 2140–2143.

(57) Brorson, S. D.; Fujimoto, J. G.; Ippen, E. P. Femtosecond Electronic Heat-Transport Dynamics in Thin Gold Films. *Phys. Rev. Lett.* **1987**, *59*, 1962–1965.

(58) Hohlfeld, J.; Wellershoff, S. S.; Güdde, J.; Conrad, U.; Jähnke, V.; Matthias, E. Electron and Lattice Dynamics Following Optical Excitation of Metals. *Chem. Phys.* **2000**, *251*, 237–258.

(59) Zhang, J. Z. Ultrafast Studies of Electron Dynamics in Semiconductor and Metal Colloidal Nanoparticles: Effects of Size and Surface. *Acc. Chem. Res.* **1997**, *30*, 423–429.

(60) Feldstein, M. J.; Keating, C. D.; Liau, Y. H.; Natan, M. J.; Scherer, N. F. Electronic Relaxation Dynamics in Coupled Metal Nanoparticles. *J. Am. Chem. Soc.* **1997**, *119*, 6638–6647.

(61) Arbouet, A.; Voisin, C.; Christofilos, D.; Langot, P.; Fatti, N. Del; Vallée, F.; Lermé, J.; Celep, G.; Cottancin, E.; Gaudry, M.; et al. Electron-Phonon Scattering in Metal Clusters. *Phys. Rev. Lett.* **2003**, *90*, 4.

(62) Hodak, J. H.; Martini, I.; Hartland, G. V. Spectroscopy and Dynamics of Nanometer-Sized Noble Metal Particles. *J. Phys. Chem. B* **1998**, *102*, 6958–6967.

(63) Chang, S. S.; Shih, C. W.; Chen, C. D.; Lai, W. C.; Wang, C. R. C. The Shape Transition of Gold Nanorods. *Langmuir* **1999**, *15*, 701–709.

(64) Link, S.; Burda, C.; Mohamed, M. B.; Nikoobakht, B.; El-Sayed, M. A. Laser Photothermal Melting and Fragmentation of Gold Nanorods: Energy and Laser Pulse-Width Dependence. *J. Phys. Chem. A*. 1999, pp 1165–1170.

(65) Link, S.; Burda, C.; Nikoobakht, B.; El-Sayed, M. A. Laser-Induced Shape Changes of Colloidal Gold Nanorods Using Femtosecond and Nanosecond Laser Pulses. *J. Phys. Chem. B* **2000**, *104*, 6152–6163.

(66) Kamat, P. V.; Flumiani, M.; Hartland, G. V. Picosecond Dynamics of Silver Nanoclusters. Photoejection of Electrons and Fragmentation. *J. Phys. Chem. B* **1998**, *102*, 3123–3128.

(67) Takami, A.; Kurita, H.; Koda, S. Laser-Induced Size Reduction of Noble Metal Particles. *J. Phys. Chem. B* **1999**, *103*, 1226–1232.

(68) Mafuné, F.; Kohno, J. Y.; Takeda, Y.; Kondow, T.; Sawabe, H. Formation and Size Control of Silver Nanoparticles by Laser Ablation in Aqueous Solution. *J. Phys. Chem. B* **2000**, *104*, 9111–9117.

(69) Hu, M.; Wang, X.; Hartland, G. V.; Mulvaney, P.; Juste, J. P.; Sader, J. E. Vibrational Response of Nanorods to Ultrafast Laser Induced Heating: Theoretical and Experimental Analysis. *J. Am. Chem. Soc.* **2003**, *125*, 14925–14933.

(70) Nisoli, M.; De Silvestri, S.; Cavalleri, A.; Malvezzi, A. Coherent Acoustic Oscillations in Metallic Nanoparticles Generated with Femtosecond Optical Pulses. *Phys. Rev. B - Condens. Matter Mater. Phys.* **1997**, *55*, R13424–R13427.

(71) Hodak, J. H.; Martini, I.; Hartland, G. V. Observation of Acoustic Quantum Beats in Nanometer Sized Au Particles. *J. Chem. Phys.* **1998**, *108*, 9210–9213.

(72) Del Fatti, N.; Voisin, C.; Chevy, F.; Vallée, F.; Flytzanis, C. Coherent Acoustic Mode Oscillation and Damping in Silver Nanoparticles. *J. Chem. Phys.* **1999**, *110*, 11484–11487.

(73) Hodak, J. H.; Henglein, A.; Hartland, G. V. Size Dependent Properties of Au Particles: Coherent Excitation and Dephasing of Acoustic Vibrational Modes. *J. Chem. Phys.* **1999**, *111*, 8613–8621.

(74) Poirier, E. J.; Poirier, D. R. *Conduction of Heat in Solids*; Clarendon Press: Oxford, 2016.

(75) Plech, A.; Kotaidis, V.; Grésillon, S.; Dahmen, C.; Von Plessen, G. Laser-Induced Heating and Melting of Gold Nanoparticles Studied by Time-Resolved x-Ray Scattering. *Phys. Rev. B - Condens. Matter Mater. Phys.* **2004**, *70*, 1–7.

(76) Perrin, B. Investigation of Short-Time Heat Transfer Effects by an Optical Pump-Probe Method. *Top. Appl. Phys.* **2006**, *107*, 333–359.

(77) Juvé, V.; Scardamaglia, M.; Maioli, P.; Crut, A.; Merabia, S.; Joly, L.; Del Fatti, N.; Vallée, F. Cooling Dynamics and Thermal Interface Resistance of Glass-Embedded Metal Nanoparticles. *Phys. Rev. B* **2009**, *80*, 195406.

(78) Hodak, J. H.; Martini, I.; Hartland, G. V. Spectroscopy and Dynamics of Nanometer-Sized Noble Metal Particles. *J. Phys. Chem. B* **1998**, *102*, 6958–6967.

(79) Shahbazyan, T. V.; Perakis, I. E.; Bigot, J. Y. Size-Dependent Surface Plasmon Dynamics in Metal Nanoparticles. *Phys. Rev. Lett.* **1998**, *81*, 3120–3123.

(80) Stella, A.; Nisoli, M.; De Silvestri, S.; Svelto, O. Size Effects in the Ultrafast Electronic Dynamics of Metallic Tin Nanoparticles. *Phys. Rev. B - Condens. Matter Mater. Phys.* **1996**,

*53*, 15497–15500.

(81) Nisoli, M.; Stagira, S.; De Silvestri, S.; Stella, A.; Tognini, P.; Cheyssac, P.; Kofman, R. Ultrafast Electronic Dynamics in Solid and Liquid Gallium Nanoparticles. *Phys. Rev. Lett.* **1997**, *78*, 3575–3578.

(82) Belotskii, E. D.; Tomchuk, P. M. Electron-Phonon Interaction and Hot Electrons in Small Metal Islands. *Surf. Sci.* **1990**, *239*, 143–155.

(83) Hodak, J.; Martini, I.; Hartland, G. V. Ultrafast Study of Electron-Phonon Coupling in Colloidal Gold Particles. *Chem. Phys. Lett.* **1998**, *284*, 135–141.

(84) Hodak, J. H.; Henglein, A.; Hartland, G. V. Electron-Phonon Coupling Dynamics in Very Small (between 2 and 8 Nm Diameter) Au Nanoparticles. *J. Chem. Phys.* **2000**, *112*, 5942–5947.

(85) Tokizaki, T.; Nakamura, A.; Kaneko, S.; Uchida, K.; Omi, S.; Tanji, H.; Asahara, Y. Subpicosecond Time Response of Third-Order Optical Nonlinearity of Small Copper Particles in Glass. *Appl. Phys. Lett.* **1994**, *65*, 941–943.

(86) Voisin, C.; Christofilos, D.; Del Fatti, N.; Vallée, F.; Prével, B.; Cottancin, E.; Lermé, J.; Pellarin, M.; Broyer, M. Size-Dependent Electron-Electron Interactions in Metal Nanoparticles. *Phys. Rev. Lett.* **2000**, *85*, 2200–2203.

(87) Voisin, C.; Christofilos, D.; Loukakos, P. A.; Del Fatti, N.; Vallée, F.; Lermé, J.; Gaudry, M.; Cottancin, E.; Pellarin, M.; Broyer, M. Ultrafast Electron-Electron Scattering and Energy Exchanges in Noble-Metal Nanoparticles. *Phys. Rev. B - Condens. Matter Mater. Phys.* **2004**, *69*, 1–13.

(88) Knappenberger, K. L.; Schwartzberg, A. M.; Dowgiallo, A. M.; Lowman, C. A. Electronic Relaxation Dynamics in Isolated and Aggregated Hollow Gold Nanospheres. *J. Am. Chem. Soc.* **2009**, *131*, 13892–13893.

(89) Enüstün, B. V.; Turkevich, J. Coagulation of Colloidal Gold. *J. Am. Chem. Soc.* **1963**, *85*, 3317–3328.

(90) Gunnarsson, L.; Rindzevicius, T.; Prikulis, J.; Kasemo, B.; Käll, M.; Zou, S.; Schatz, G. C. Confined Plasmons in Nanofabricated Single Silver Particle Pairs: Experimental Observations of Strong Interparticle Interactions. *J. Phys. Chem. B* **2005**, *109*, 1079–1087.

(91) Lassiter, J. B.; Aizpurua, J.; Hernandez, L. I.; Brandl, D. W.; Romero, I.; Lal, S.; Hafner, J. H.; Nordlander, P.; Hales, N. R. Close Encounters between Two Nanoshells. *Nano Lett.* **2008**, *8*, 1212–1218.

(92) Lee, S. J.; Morrill, A. R.; Moskovits, M. Hot Spots in Silver Nanowire Bundles for Surface-Enhanced Raman Spectroscopy. *J. Am. Chem. Soc.* **2006**, *128*, 2200–2201.

(93) Bosnick, K. A.; Jiang, J.; Brus, L. E. Fluctuations and Local Symmetry in Single-Molecule Rhodamine 6G Raman Scattering on Silver Nanocrystal Aggregates. *J. Phys. Chem. B* **2002**, *106*, 8096–8099.

(94) Jain, P. K.; Qian, W.; El-Sayed, M. A. Ultrafast Electron Relaxation Dynamics in Coupled Metal Nanoparticles in Aggregates. *J. Phys. Chem. B* **2006**, *110*, 136–142.

(95) Ramakrishna, G.; Varnavski, O.; Kim, J.; Lee, D.; Goodson, T. Quantum-Sized Gold Clusters as Efficient Two-Photon Absorbers. *J. Am. Chem. Soc.* **2008**, *130*, 5032–5033.

(96) Rogach, A. L. *Semiconductor Nanocrystal Quantum Dots Synthesis, Assembly, Spectroscopy and Applications*; Springer Wien New York, 2008.

(97) Bawendi, M. G.; Steigerwald, M. L.; Brus, L. E. The Quantum Mechanics of Larger Semiconductor Clusters ("Quantum Dots"). *Annu. Rev. Phys. Chem.* **1990**, *41*, 477–496.

(98) Alivisatos, A. P. Perspectives on the Physical Chemistry of Semiconductor Nanocrystals. *J. Phys. Chem.* 1996, pp 13226–13239.

(99) Efros, A. L.; Nesbitt, D. J. Origin and Control of Blinking in Quantum Dots. *Nature Nanotechnology*. 2016, pp 661–671.

(100) Brus, L. E. Electron-Electron and Electron-Hole Interactions in Small Semiconductor Crystallites: The Size Dependence of the Lowest Excited Electronic State. *J. Chem. Phys.* **1984**, *80*, 4403–4409.

(101) Ekimov, A. I.; Efros, A. L.; Onushchenko, A. A. Quantum Size Effect in Semiconductor Microcrystals. *Solid State Commun.* **1985**, *56*, 921–924.

(102) Michalet, X.; Pinaud, F. F.; Bentolila, L. A.; Tsay, J. M.; Doose, S.; Li, J. J.; Sundaresan, G.; Wu, A. M.; Gambhir, S. S.; Weiss, S. Quantum Dots for Live Cells, in Vivo Imaging, and Diagnostics. *Science*. 2005, pp 538–544.

(103) Alivisatos, A. P.; Gu, W.; Larabell, C. Quantum Dots as Cellular Probes. *Annual Review of Biomedical Engineering*. 2005, pp 55–76.

(104) Algar, W. R.; Susumu, K.; Delehanty, J. B.; Medintz, I. L. Semiconductor Quantum Dots in Bioanalysis: Crossing the Valley of Death. *Anal. Chem.* **2011**, *83*, 8826–8837.

(105) Dresselhaus, M. S.; Chen, G.; Tang, M. Y.; Yang, R.; Lee, H.; Wang, D.; Ren, Z.; Fleurial, J. P.; Gogna, P. New Directions for Low-Dimensional Thermoelectric Materials. *Adv. Mater.* **2007**, *19*, 1043–1053.

(106) Cao, A.; Liu, Z.; Chu, S.; Wu, M.; Ye, Z.; Cai, Z.; Chang, Y.; Wang, S.; Gong, Q.; Liu, Y. A Facile One-Step Method to Produce Craphene-CdS Quantum Dot Nanocomposites as Promising Optoelectronic Materials. *Adv. Mater.* **2010**, *22*, 103–106.

(107) Nozik, A. J. Quantum Dot Solar Cells. In *Physica E: Low-Dimensional Systems and Nanostructures*; 2002; Vol. 14, pp 115–120.

(108) Klimov, V. I. Mechanisms for Photogeneration and Recombination of Multiexcitons in Semiconductor Nanocrystals: Implications for Lasing and Solar Energy Conversion. *J. Phys. Chem. B* **2006**, *110*, 16827–16845.

(109) Semonin, O. E.; Luther, J. M.; Choi, S.; Chen, H. Y.; Gao, J.; Nozik, A. J.; Beard, M. C. Peak External Photocurrent Quantum Efficiency Exceeding 100% via MEG in a Quantum Dot Solar Cell. *Science (80-. ).* **2011**, *334*, 1530–1533.

(110) Bomm, J.; Büchtemann, A.; Chatten, A. J.; Bose, R.; Farrell, D. J.; Chan, N. L. A.; Xiao, Y.; Slooff, L. H.; Meyer, T.; Meyer, A.; et al. Fabrication and Full Characterization of State-of-the-

Art Quantum Dot Luminescent Solar Concentrators. *Sol. Energy Mater. Sol. Cells* **2011**, *95*, 2087–2094.

(111) Colvin, V. L.; Schlamp, M. C.; Alivisatos, A. P. Light-Emitting Diodes Made from Cadmium Selenide Nanocrystals and a Semiconducting Polymer. *Nature* **1994**, *370*, 354–357.

(112) Mattoussi, H.; Radzilowski, L. H.; Dabbousi, B. O.; Thomas, E. L.; Bawendi, M. G.; Rubner, M. F. Electroluminescence from Heterostructures of Poly(Phenylene Vinylene) and Inorganic CdSe Nanocrystals. *J. Appl. Phys.* **1998**, *83*, 7965–7974.

(113) Anikeeva, P. O.; Halpert, J. E.; Bawendi, M. G.; Bulović, V. Quantum Dot Light-Emitting Devices with Electroluminescence Tunable over the Entire Visible Spectrum. *Nano Lett.* **2009**, *9*, 2532–2536.

(114) Banfi, G. P.; Degiorgio, V.; Ricard, D. *Nonlinear Optical Properties of Semiconductor Nanocrystals*; Cambridge University Press, Cambridge, 1998; Vol. 47.

(115) Ekimov, A. I. *Optical Properties of Semiconductor Quantum Dots in Glass Matrix*; Springer, Berlin, 1991; Vol. 1991.

(116) Neamen, D. *An Introduction to Semiconductor Devices*; McGraw-Hill Education, 2005.

(117) Kittel, C.; Holcomb, D. F. *Introduction to Solid State Physics*, 8th ed.; John Wiley & Sons, Inc, 1967; Vol. 35.

(118) Kita, T.; Harada, Y.; Asahi, S. *Fundamentals of Semiconductors*, 1st ed.; Springer-Verlag, Berlin, 2019.

(119) Rogalski, M. S.; Palmer, S. B. *Solid State Physics*, supplement.; Academic Press, New York, 2014.

(120) Van Zeghbroeck, B. *Principles of Semiconductor Devices - [Book Review]*; colorado university, 2008; Vol. 22.

(121) Murray, C. B.; Norris, D. J.; Bawendi, M. G. Synthesis and Characterization of Nearly Monodisperse CdE (E = S, Se, Te) Semiconductor Nanocrystallites. *J. Am. Chem. Soc.* **1993**, *115*, 8706–8715.

(122) Rossetti, R.; Nakahara, S.; Brus, L. E. Quantum Size Effects in the Redox Potentials, Resonance Raman Spectra, and Electronic Spectra of CdS Crystallites in Aqueous Solution. *J. Chem. Phys.* **1983**, *79*, 1086–1088.

(123) Takagahara, T.; Takeda, K. Theory of the Quantum Confinement Effect on Excitons in Quantum Dots of Indirect-Gap Materials. *Phys. Rev. B* **1992**, *46*, 15578–15581.

(124) Wilson, W. L.; Szajowski, P. F.; Brus, L. E. Quantum Confinement in Size-Selected, Surface-Oxidized Silicon Nanocrystals. *Science (80-. ).* **1993**, *262*, 1242–1244.

(125) Nirmal, M.; Brus, L. Luminescence Photophysics in Semiconductor Nanocrystals. *Accounts of Chemical Research*. 1999, pp 407–414.

(126) Efros, A. L.; Efros, A. L. Interband Absorption of Light in a Semiconductor Sphere. *Sov. physics. Semicond.* **1982**, *16*, 772–775.

(127) Brus, L. E. A Simple Model for the Ionization Potential, Electron Affinity, and Aqueous Redox Potentials of Small Semiconductor Crystallites. *J. Chem. Phys.* **1983**, *79*, 5566–5571.

(128) Steigerwald, M. L.; Brus, L. E. Semiconductor Crystallites: A Class of Large Molecules. *Acc. Chem. Res.* **1990**, *23*, 183–188.

(129) Takagahara, T. Effects of Dielectric Confinement and Electron-Hole Exchange Interaction on Excitonic States in Semiconductor Quantum Dots. *Phys. Rev. B* **1993**, *47*, 4569–4584.

(130) Ekimov, A. I.; Kudryavtsev, I. A.; Efros, A. L.; Yazeva, T. V.; Hache, F.; Schanne-Klein, M. C.; Rodina, A. V.; Ricard, D.; Flytzanis, C. Absorption and Intensity-Dependent Photoluminescence Measurements on CdSe Quantum Dots: Assignment of the First Electronic Transitions. *J. Opt. Soc. Am. B* **1993**, *10*, 100.

(131) Alivisatos, A. P. Semiconductor Clusters, Nanocrystals, and Quantum Dots. *Science (80-. ).* **1996**, *271*, 933–937.

(132) Boles, M. A.; Ling, D.; Hyeon, T.; Talapin, D. V. The Surface Science of Nanocrystals. *Nature Materials*. 2016, pp 141–153.

(133) Hines, D. A.; Kamat, P. V. Recent Advances in Quantum Dot Surface Chemistry. *ACS Applied Materials and Interfaces*. 2014, pp 3041–3057.

(134) Kilina, S.; Ivanov, S.; Tretiak, S. Effect of Surface Ligands on Optical and Electronic Spectra of Semiconductor Nanoclusters. *J. Am. Chem. Soc.* **2009**, *131*, 7717–7726.

(135) Kilina, S. V.; Tamukong, P. K.; Kilin, D. S. Surface Chemistry of Semiconducting Quantum Dots: Theoretical Perspectives. *Acc. Chem. Res.* **2016**, *49*, 2127–2135.

(136) Murray, C. B. Synthesis and Characterization of II-VI Quantum Dots and Their Assembly into 3D Quantum Dot Superlattices, MIT, Cambridge, MA, 1995.

(137) Derfus, A. M.; Chan, W. C. W.; Bhatia, S. N. Probing the Cytotoxicity of Semiconductor Quantum Dots. *Nano Lett.* **2004**, *4*, 11–18.

(138) Herz, L. M. Charge-Carrier Dynamics in Organic-Inorganic Metal Halide Perovskites. *Annu. Rev. Phys. Chem.* **2016**, *67*, 65–89.

(139) Jacoboni, C.; Canali, C.; Ottaviani, G.; Alberigi Quaranta, A. A Review of Some Charge Transport Properties of Silicon. *Solid State Electron.* **1977**, *20*, 77–89.

(140) Hewa-Kasakarage, N. N.; El-Khoury, P. Z.; Tarnovsky, A. N.; Kirsanova, M.; Nemitz, I.; Nemchinov, A.; Zamkov, M. Ultrafast Carrier Dynamics in Type II ZnSe/CdS/ZnSe Nanobarbells. *ACS Nano* **2010**, *4*, 1837–1844.

(141) Nozik, A. J. Spectroscopy and Hot Electron Relaxation Dynamics in Semiconductor Quantum Wells and Quantum Dots. *Annu. Rev. Phys. Chem.* **2001**, *52*, 193–231.

(142) Pelant, I.; Valenta, J. *Luminescence Spectroscopy of Semiconductors*; Oxford University Press: Oxford, 2012; Vol. 9780199588336.

(143) Knupfer, M. Exciton Binding Energies in Organic Semiconductors. *Appl. Phys. A Mater. Sci. Process.* **2003**, *77*, 623–626.

(144) Shockley, W.; Queisser, H. J. Detailed Balance Limit of Efficiency of P-n Junction Solar Cells. *J. Appl. Phys.* **1961**, *32*, 510–519.

(145) Price, M. B.; Butkus, J.; Jellicoe, T. C.; Sadhanala, A.; Briane, A.; Halpert, J. E.; Broch, K.; Hodgkiss, J. M.; Friend, R. H.; Deschler, F. Hot-Carrier Cooling and Photoinduced Refractive Index Changes in Organic-Inorganic Lead Halide Perovskites. *Nat. Commun.* **2015**, *6*.

(146) Conibeer, G. J.; König, D.; Green, M. A.; Guillemoles, J. F. Slowing of Carrier Cooling in Hot Carrier Solar Cells. *Thin Solid Films* **2008**, *516*, 6948–6953.

(147) Byrnes, S. J. F. *Basic Theory and Phenomenology of Polarons*; Department of Physics, University of California at Berkeley, Berkeley, CA, 2008.

(148) Auger, P. Secondary β-Rays Produced in a Gas by X-Rays. *Comptes Rendus Acad. Sci. Paris* **1923**, *177*, 169.

(149) Pietryga, J. M.; Park, Y. S.; Lim, J.; Fidler, A. F.; Bae, W. K.; Brovelli, S.; Klimov, V. I. Spectroscopic and Device Aspects of Nanocrystal Quantum Dots. *Chemical Reviews*. 2016, pp 10513–10622.

(150) Klimov, V. I. Spectral and Dynamical Properties of Multiexcitons in Semiconductor Nanocrystals. *Annu. Rev. Phys. Chem.* **2007**, *58*, 635–673.

(151) Kambhampati, P. Unraveling the Structure and Dynamics of Excitons in Semiconductor Quantum Dots. *Acc. Chem. Res.* **2011**, *44*, 1–13.

(152) Schaller, R. D.; Pietryga, J. M.; Goupalov, S. V.; Petruska, M. A.; Ivanov, S. A.; Klimov, V. I. Breaking the Phonon Bottleneck in Semiconductor Nanocrystals via Multiphonon Emission Induced by Intrinsic Nonadiabatic Interactions. *Phys. Rev. Lett.* **2005**, *95*.

(153) Klimov, V.; Mikhailovsky, A.; McBranch, D.; Leatherdale, C.; Bawendi, M. Mechanisms for Intraband Energy Relaxation in Semiconductor Quantum Dots: The Role of Electron-Hole Interactions. *Phys. Rev. B - Condens. Matter Mater. Phys.* **2000**, *61*, R13349–R13352.

(154) Klimov, V. I.; Schwarz, C. J.; Mc Branch, D. W.; Leatherdale, C. A.; Bawendi, M. G. Ultrafast Dynamics of Inter- and Intraband Transitions in Semiconductor Nanocrystals: Implications for Quantum-Dot Lasers. *Phys. Rev. B - Condens. Matter Mater. Phys.* **1999**, *60*, R2177–R2180.

(155) Kambhampati, P. Hot Exciton Relaxation Dynamics in Semiconductor Quantum Dots: Radiationless Transitions on the Nanoscale. *J. Phys. Chem. C* **2011**, *115*, 22089–22109.

(156) Efros, A. L.; Kharchenko, V. A.; Rosen, M. Breaking the Phonon Bottleneck in Nanometer Quantum Dots: Role of Auger-like Processes. *Solid State Commun.* **1995**, *93*, 281–284.

(157) Pandey, A.; Guyot-Sionnest, P. Slow Electron Cooling in Colloidal Quantum Dots. *Science (80-. ).* **2008**, *322*, 929–932.

(158) Fuhr, A. S.; Yun, H. J.; Makarov, N. S.; Li, H.; McDaniel, H.; Klimov, V. I. Light Emission Mechanisms in CuInS2 Quantum Dots Evaluated by Spectral Electrochemistry. *ACS Photonics* **2017**, *4*, 2425–2435.

(159) Banin, U.; Ben-Shahar, Y.; Vinokurov, K. Hybrid Semiconductor-Metal Nanoparticles: From Architecture to Function. *Chemistry of Materials*. 2014, pp 97–110.

(160) Costi, R.; Saunders, A. E.; Banin, U. Colloidal Hybrid Nanostructures: A New Type of Functional Materials. *Angewandte Chemie - International Edition*. 2010, pp 4878–4897.

(161) Mokari, T.; Rothenberg, E.; Popov, I.; Costi, R.; Banin, U. Selective Growth of Metal Tips onto Semiconductor Quantum Rods and Tetrapods. *Science (80-. ).* **2004**, *304*, 1787–1790.

(162) Patra, B. K.; Khilari, S.; Bera, A.; Mehetor, S. K.; Pradhan, N.; Pradhan, N. Chemically Filled and Au-Coupled BiSbS3 Nanorod Heterostructures for Photoelectrocatalysis. *Chem. Mater.* **2017**, *29*, 1116–1126.

(163) Dutta, A.; Samantara, A. K.; Adhikari, S. Das; Jena, B. K.; Pradhan, N. Au Nanowire-Striped Cu3P Platelet Photoelectrocatalysts. *J. Phys. Chem. Lett.* **2016**, *7*, 1077–1082.

(164) Patra, B. K.; Khilari, S.; Pradhan, D.; Pradhan, N. Hybrid Dot?Disk Au-Cuins2 Nanostructures as Active Photocathode for Efficient Evolution of Hydrogen from Water. *Chem. Mater.* **2016**, *28*, 4358–4366.

(165) Dutta, S. K.; Mehetor, S. K.; Pradhan, N. Metal Semiconductor Heterostructures for Photocatalytic Conversion of Light Energy. *J. Phys. Chem. Lett.* **2015**, *6*, 936–944.

(166) Patra, B. K.; Guria, A. K.; Dutta, A.; Shit, A.; Pradhan, N. Au-SnS Hetero Nanostructures: Size of Au Matters. *Chem. Mater.* **2014**, *26*, 7194–7200.

(167) Dana, J.; Maity, P.; Ghosh, H. N. Hot-Electron Transfer from the Semiconductor Domain to the Metal Domain in CdSe@CdS{Au} Nano-Heterostructures. *Nanoscale* **2017**, *9*, 9723–9731.

(168) Dana, J.; Debnath, T.; Maity, P.; Ghosh, H. N. Enhanced Charge Separation in an Epitaxial Metal-Semiconductor Nanohybrid Material Anchored with an Organic Molecule. *J. Phys. Chem. C* **2015**, *119*, 22181–22189.

(169) Lambright, S.; Butaeva, E.; Razgoniaeva, N.; Hopkins, T.; Smith, B.; Perera, D.; Corbin, J.; Khon, E.; Thomas, R.; Moroz, P.; et al. Enhanced Lifetime of Excitons in Nonepitaxial Au/CdS Core/Shell Nanocrystals. *ACS Nano* **2014**, *8*, 352–361.

(170) Wu, K.; Zhu, H.; Lian, T. Ultrafast Exciton Dynamics and Light-Driven H2 Evolution in Colloidal Semiconductor Nanorods and Pt-Tipped Nanorods. *Acc. Chem. Res.* **2015**, *48*, 851–859.

(171) Nakibli, Y.; Mazal, Y.; Dubi, Y.; Wächtler, M.; Amirav, L. Size Matters: Cocatalyst Size Effect on Charge Transfer and Photocatalytic Activity. *Nano Lett.* **2018**, *18*, 357–364.

(172) Wächtler, M.; Kalisman, P.; Amirav, L. Charge-Transfer Dynamics in Nanorod Photocatalysts with Bimetallic Metal Tips. *J. Phys. Chem. C* **2016**, *120*, 24491–24497.

(173) Lu, X.; Dandapat, A.; Huang, Y.; Zhang, L.; Rong, Y.; Dai, L.; Sasson, Y.; Zhang, J.; Chen, T. Tris Base Assisted Synthesis of Monodispersed Citrate-Capped Gold Nanospheres with Tunable Size. *RSC Adv.* **2016**, *6*, 60916–60921.

(174) Bidault, S.; Polman, A. Water-Based Assembly and Purification of Plasmon-Coupled Gold Nanoparticle Dimers and Trimers. *Int. J. Opt.* **2012**, *2012*.

(175) Bidault, S.; García De Abajo, F. J.; Polman, A. Plasmon-Based Nanolenses Assembled on a Well-Defined DNA Template. *J. Am. Chem. Soc.* **2008**, *130*, 2750–2751.

(176) Zanchet, D.; Micheel, C. M.; Parak, W. J.; Gerion, D.; Alivisatos, A. P. Electrophoretic Isolation of Discrete Au Nanocrystal/DNA Conjugates. *Nano Lett.* **2001**, *1*, 32–35.

(177) Yang, J.; Elim, H. I.; Zhang, Q. B.; Lee, J. Y.; Ji, W. Rational Synthesis, Self-Assembly, and Optical Properties of PbS-Au Heterogeneous Nanostructures via Preferential Deposition. *J. Am. Chem. Soc.* **2006**, *128*, 11921–11926.

(178) Anchal Yadav, A. F. Synthesis and Characterization of Complete Gold Shelling of PbS Nanostructures. *Under Prep.* **2021**.

(179) Shavel, A.; Cadavid, D.; Ibáñez, M.; Carrete, A.; Cabot, A. Continuous Production of Cu 2ZnSnS 4 Nanocrystals in a Flow Reactor. *J. Am. Chem. Soc.* **2012**, *134*, 1438–1441.

(180) Anchal Yadav, A. F. Synthesis and Characterization of CZTS-Au and CZTS-Ag Heterostructures. *Prep.* **2021**.

(181) Cozzoli, P. D.; Kornowski, A.; Weller, H. Low-Temperature Synthesis of Soluble and Processable Organic-Capped Anatase TiO2 Nanorods. *J. Am. Chem. Soc.* **2003**, *125*, 14539–14548.

(182) Liu, Y.; Li, J.; Cao, H.; Qu, B.; Chen, Z.; Gong, Q.; Xu, S.; Cao, S. Conjugated Polymers Containing Phenothiazine Moieties in the Main Chain. *Polym. Adv. Technol.* **2006**, *17*, 468–473.

(183) Duvva, N.; Sudhakar, K.; Badgurjar, D.; Chitta, R.; Giribabu, L. Spacer Controlled Photo-Induced Intramolecular Electron Transfer in a Series of Phenothiazine-Boron Dipyrromethene Donor-Acceptor Dyads. *J. Photochem. Photobiol. A Chem.* **2015**, *312*, 8–19.

(184) Sailer, M.; Franz, A. W.; Müller, T. J. J. Synthesis and Electronic Properties of Monodisperse Oligophenothiazines. *Chem. - A Eur. J.* **2008**, *14*, 2602–2614.

(185) Jain, K.; Duvva, N.; Badgurjar, D.; Giribabu, L.; Chitta, R. Synthesis and Spectroscopic Studies of Axially Bound Tetra(Phenothiazinyl)/Tetra(Bis(4′-Tert-Butylbiphenyl-4-Yl)Aniline)-Zinc(II)Porphyrin-Fullero[C60 and C70]Pyrrolidine Donor-Acceptor Triads. *Inorg. Chem. Commun.* **2016**, *66*, 5–10.

(186) Imahori, H.; Hayashi, S.; Umeyama, T.; Eu, S.; Oguro, A.; Kang, S.; Matano, Y.; Shishido, T.; Ngamsinlapasathian, S.; Yoshikawa, S. Comparison of Electrode Structures and Photovoltaic Properties of Porphyrin-Sensitized Solar Cells with TiO2 and Nb, Ge, Zr-Added TiO2 Composite Electrodes. *Langmuir* **2006**, *22*, 11405–11411.

(187) Franz, A. W.; Zhou, Z.; Turdean, R.; Wagener, A.; Sarkar, B.; Hartmann, M.; Ernst, S.; Thiel, W. R.; Müller, T. J. J. Carbamate-Linked (Oligo)Phenothiazines in Mesoporous Silica by Post-Synthetic Grafting: Fluorescent Redox-Active Hybrid Materials. *European J. Org. Chem.* **2009**, No. 23, 3895–3905.

(188) Arlt, J.; Tyndall, D.; Rae, B. R.; Li, D. D. U.; Richardson, J. A.; Henderson, R. K. A Study of Pile-up in Integrated Time-Correlated Single Photon Counting Systems. *Rev. Sci. Instrum.* **2013**, *84*.

(189) O'Connor, D. V.; Phillips, D. *Time-Correlated Single Photon Counting*; Academic press, 2008.

(190) Lakowicz, J. R. *Principles of Fluorescence Spectroscopy*, 3rd ed.; Springer: New York, 2006.

(191) Sewall, S. L.; Cooney, R. R.; Anderson, K. E. H.; Dias, E. A.; Sagar, D. M.; Kambhampati, P. State-Resolved Studies of Biexcitons and Surface Trapping Dynamics in Semiconductor Quantum Dots. *J. Chem. Phys.* **2008**, *129*.

(192) Wheeler, D. A.; Zhang, J. Z. Exciton Dynamics in Semiconductor Nanocrystals. *Advanced Materials*. 2013, pp 2878–2896.

(193) Tvrdy, K.; Frantsuzov, P. A.; Kamat, P. V. Photoinduced Electron Transfer from Semiconductor Quantum Dots to Metal Oxide Nanoparticles. *Proc. Natl. Acad. Sci. U. S. A.* **2011**, *108*, 29–34.

(194) Rabouw, F. T.; de Mello Donega, C. Excited-State Dynamics in Colloidal Semiconductor Nanocrystals. *Top Curr Chem*. 2016.

(195) Manjavacas, A.; Liu, J. G.; Kulkarni, V.; Nordlander, P. Plasmon-Induced Hot Carriers in Metallic Nanoparticles. *ACS Nano* **2014**, *8*, 7630–7638.

(196) Aruda, K. O.; Tagliazucchi, M.; Sweeney, C. M.; Hannah, D. C.; Schatz, G. C.; Weiss, E. A. Identification of Parameters through Which Surface Chemistry Determines the Lifetimes of Hot Electrons in Small Au Nanoparticles. *Proc. Natl. Acad. Sci. U. S. A.* **2013**, *110*, 4212–4217.

(197) Bigot, J. Y.; Halté, V.; Merle, J. C.; Daunois, A. Electron Dynamics in Metallic Nanoparticles. *Chem. Phys.* **2000**, *251*, 181–203.

(198) Harutyunyan, H.; Martinson, A. B. F.; Rosenmann, D.; Khorashad, L. K.; Besteiro, L. V.; Govorov, A. O.; Wiederrecht, G. P. Anomalous Ultrafast Dynamics of Hot Plasmonic Electrons in Nanostructures with Hot Spots. *Nat. Nanotechnol.* **2015**, *10*, 770–774.

(199) Kelly, K. L.; Coronado, E.; Zhao, L. L.; Schatz, G. C. The Optical Properties of Metal Nanoparticles: The Influence of Size, Shape, and Dielectric Environment. *J. Phys. Chem. B* **2003**, *107*, 668–677.

(200) Shabaninezhad, M.; Abuhagr, A.; Sakthivel, N. A.; Kumara, C.; Dass, A.; Kwak, K.; Pyo, K.; Lee, D.; Ramakrishna, G. Ultrafast Electron Dynamics in Thiolate-Protected Plasmonic Gold Clusters: Size and Ligand Effect. *J. Phys. Chem. C* **2019**, *123*, 13344–13353.

(201) Schumacher, L.; Jose, J.; Janoschka, D.; Dreher, P.; Davis, T. J.; Ligges, M.; Li, R.; Mo, M.; Park, S.; Shen, X.; et al. Precision Plasmonics with Monomers and Dimers of Spherical Gold Nanoparticles: Nonequilibrium Dynamics at the Time and Space Limits. *J. Phys. Chem. C* **2019**, *123*, 13181–13191.

(202) Savage, K. J.; Hawkeye, M. M.; Esteban, R.; Borisov, A. G.; Aizpurua, J.; Baumberg, J. J. Revealing the Quantum Regime in Tunnelling Plasmonics. *Nature* **2012**, *491*, 574–577.

(203) Kühler, P.; Roller, E. M.; Schreiber, R.; Liedl, T.; Lohmüller, T.; Feldmann, J. Plasmonic DNA-Origami Nanoantennas for Surface-Enhanced Raman Spectroscopy. *Nano Lett.* **2014**, *14*, 2914–2919.

(204) Cha, H.; Yoon, J. H.; Yoon, S. Probing Quantum Plasmon Coupling Using Gold Nanoparticle Dimers with Tunable Interparticle Distances down to the Subnanometer Range. *ACS Nano* **2014**, *8*, 8554–8563.

(205) Storhoff, J. J.; Lazarides, A. A.; Mucic, R. C.; Mirkin, C. A.; Letsinger, R. L.; Schatz, G. C. What Controls the Optical Properties of DNA-Linked Gold Nanoparticle Assemblies? *J. Am.*

*Chem. Soc.* **2000**, *122*, 4640–4650.

(206) Daniel, M. C.; Astruc, D. Gold Nanoparticles: Assembly, Supramolecular Chemistry, Quantum-Size-Related Properties, and Applications Toward Biology, Catalysis, and Nanotechnology. *Chemical Reviews*. 2004, pp 293–346.

(207) Grzelczak, M.; Vermant, J.; Furst, E. M.; Liz-Marzán, L. M. Directed Self-Assembly of Nanoparticles. *ACS Nano*. 2010, pp 3591–3605.

(208) Cortés, E. Activating Plasmonic Chemistry: Plasmonic Photocatalysts Can Reduce Activation Barriers and Unlock Reaction Pathways. *Science (80-. ).* **2018**, *362*, 28–29.

(209) Clavero, C. Plasmon-Induced Hot-Electron Generation at Nanoparticle/Metal-Oxide Interfaces for Photovoltaic and Photocatalytic Devices. *Nat. Photonics* **2014**, *8*, 95–103.

(210) Linic, S.; Aslam, U.; Boerigter, C.; Morabito, M. Photochemical Transformations on Plasmonic Metal Nanoparticles. *Nat. Mat.* 2015, pp 567–576.

(211) Cortés, E.; Xie, W.; Cambiasso, J.; Jermyn, A. S.; Sundararaman, R.; Narang, P.; Schlücker, S.; Maier, S. A. Plasmonic Hot Electron Transport Drives Nano-Localized Chemistry. *Nat. Commun.* **2017**, *8*.

(212) Mondal, N.; De, A.; Samanta, A. Biexciton Generation and Dissociation Dynamics in Formamidinium- and Chloride-Doped Cesium Lead Iodide Perovskite Nanocrystals. *J. Phys. Chem. Lett.* **2018**, *9*, 3673–3679.

(213) Shibu Joseph, S. T.; Ipe, B. I.; Pramod, P.; George Thomas, K. Gold Nanorods to Nanochains: Mechanistic Investigations on Their Longitudinal Assembly Using α,ω-Alkanedithiols and Interplasmon Coupling. *J. Phys. Chem. B* **2006**, *110*, 150–157.

(214) Lermusiaux, L.; Sereda, A.; Portier, B.; Larquet, E.; Bidault, S. Reversible Switching of the Interparticle Distance in DNA-Templated Gold Nanoparticle Dimers. *ACS Nano* **2012**, *6*, 10992–10998.

(215) Pal, S. K.; Chatterjee, H.; Ghosh, S. K. Manipulating the Confinement of Electromagnetic Field in Size-Specific Gold Nanoparticles Dimers and Trimers. *RSC Adv.* **2019**, *9*, 42145–42154.

(216) Inouye, H.; Tanaka, K.; Tanahashi, I. Ultrafast Dynamics of Nonequilibrium Electrons in a Gold Nanoparticle System. *Phys. Rev. B - Condens. Matter Mater. Phys.* **1998**, *57*, 11334–11340.

(217) Vdović, S.; Wang, Y.; Li, B.; Qiu, M.; Wang, X.; Guo, Q.; Xia, A. Excited State Dynamics of β-Carotene Studied by Means of Transient Absorption Spectroscopy and Multivariate Curve Resolution Alternating Least-Squares Analysis. *Phys. Chem. Chem. Phys.* **2013**, *15*, 20026–20036.

(218) Fedorovich, R. D.; Naumovets, A. G.; Tomchuk, P. M. Electronic Properties of Island Thin Films Caused by Surface Scattering of Electrons. *Prog. Surf. Sci.* **1993**, *42*, 189–200.

(219) Kamat, P. V.; Tvrdy, K.; Baker, D. R.; Radich, J. G. Beyond Photovoltaics: Semiconductor Nanoarchitectures for Liquid-Junction Solar Cells. *Chem. Rev.* **2010**, *110*, 6664–6688.

(220) Sargent, E. H. Colloidal Quantum Dot Solar Cells. *Nature Photonics*. 2012, pp 133–135.

(221) Konstantatos, G.; Howard, I.; Fischer, A.; Hoogland, S.; Clifford, J.; Klem, E.; Levina, L.; Sargent, E. H. Ultrasensitive Solution-Cast Quantum Dot Photodetectors. *Nature* **2006**, *442*, 180–183.

(222) Konstantatos, G.; Badioli, M.; Gaudreau, L.; Osmond, J.; Bernechea, M.; De Arquer, F. P. G.; Gatti, F.; Koppens, F. H. L. Hybrid Graphenêquantum Dot Phototransistors with Ultrahigh Gain. *Nat. Nanotechnol.* **2012**, *7*, 363–368.

(223) Sun, L.; Choi, J. J.; Stachnik, D.; Bartnik, A. C.; Hyun, B. R.; Malliaras, G. G.; Hanrath, T.; Wise, F. W. Bright Infrared Quantum-Dot Light-Emitting Diodes through Inter-Dot Spacing Control. *Nat. Nanotechnol.* **2012**, *7*, 369–373.

(224) Dai, X.; Zhang, Z.; Jin, Y.; Niu, Y.; Cao, H.; Liang, X.; Chen, L.; Wang, J.; Peng, X. Solution-Processed, High-Performance Light-Emitting Diodes Based on Quantum Dots. *Nature* **2014**, *515*, 96–99.

(225) Han, Z.; Qiu, F.; Eisenberg, R.; Holland, P. L.; Krauss, T. D. Robust Photogeneration of H2in Water Using Semiconductor Nanocrystals and a Nickel Catalyst. *Science (80-. ).* **2012**, *338*, 1321–1324.

(226) Brown, K. A.; Dayal, S.; Ai, X.; Rumbles, G.; King, P. W. Controlled Assembly of Hydrogenase-CdTe Nanocrystal Hybrids for Solar Hydrogen Production. *J. Am. Chem. Soc.* **2010**, *132*, 9672–9680.

(227) Schaller, R. D.; Klimov, V. I. High Efficiency Carrier Multiplication in PbSe Nanocrystals: Implications for Solar Energy Conversion. *Phys. Rev. Lett.* **2004**, *92*.

(228) Mcguire, J. A.; Joo, J.; Pietryga, J. M.; Schaller, R. D.; Klimov, V. I. New Aspects of Carrier Multiplication in Semiconductor Nanocrystals. *Acc. Chem. Res.* **2008**, *41*, 1810–1819.

(229) Minbiao, J.; Sungnam, P.; Connor, S. T.; Mokari, T.; Yi, C.; Gaffney, K. J. Efficient Multiple Exciton Generation Observed in Colloidal PbSe Quantum Dots with Temporally and Spectrally Resolved Intraband Excitation. *Nano Lett.* **2009**, *9*, 1217–1222.

(230) Wang, S.; Khafizov, M.; Tu, X.; Zheng, M.; Krauss, T. D. Multiple Exciton Generation in Single-Walled Carbon Nanotubes. *Nano Lett.* **2010**, *10*, 2381–2386.

(231) Baer, R.; Rabani, E. Can Impact Excitation Explain Efficient Carrier Multiplication in Carbon Nanotube Photodiodes? *Nano Lett.* **2010**, *10*, 3277–3282.

(232) Sagarzazu, G.; Inoue, K.; Saruyama, M.; Sakamoto, M.; Teranishi, T.; Masuo, S.; Tamai, N. Ultrafast Dynamics and Single Particle Spectroscopy of Au-CdSe Nanorods. *Phys. Chem. Chem. Phys.* **2013**, *15*, 2141–2152.

(233) Menagen, G.; Macdonald, J. E.; Shemesh, Y.; Popov, I.; Banin, U. Au Growth on Semiconductor Nanorods: Photoinduced versus Thermal Growth Mechanisms. *J. Am. Chem. Soc.* **2009**, *131*, 17406–17411.

(234) Wu, K.; Zhu, H.; Liu, Z.; Rodríguez-Córdoba, W.; Lian, T. Ultrafast Charge Separation and Long-Lived Charge Separated State in Photocatalytic CdS-Pt Nanorod Heterostructures. *J. Am. Chem. Soc.* **2012**, *134*, 10337–10340.

(235) Mongin, D.; Shaviv, E.; Maioli, P.; Crut, A.; Banin, U.; Del Fatti, N.; Vallée, F. Ultrafast

Photoinduced Charge Separation in Metal-Semiconductor Nanohybrids. *ACS Nano* **2012**, *6*, 7034–7043.

(236) Costi, R.; Saunders, A. E.; Elmalem, E.; Salant, A.; Banin, U. Visible Light-Induced Charge Retention and Photocatalysis with Hybrid CdSe-Au Nanodumbbells. *Nano Lett.* **2008**, *8*, 637–641.

(237) Yang, T. T.; Chen, W. T.; Hsu, Y. J.; Wei, K. H.; Lin, T. Y.; Lin, T. W. Interfacial Charge Carrier Dynamics in Core-Shell Au-CdS Nanocrystals. *J. Phys. Chem. C* **2010**, *114*, 11414–11420.

(238) Bang, J. U.; Lee, S. J.; Jang, J. S.; Choi, W.; Song, H. Geometric Effect of Single or Double Metal-Tipped CdSe Nanorods on Photocatalytic H2 Generation. *J. Phys. Chem. Lett.* **2012**, *3*, 3781–3785.

(239) Kim, S. M.; Lee, S. J.; Kim, S. H.; Kwon, S.; Yee, K. J.; Song, H.; Somorjai, G. A.; Park, J. Y. Hot Carrier-Driven Catalytic Reactions on Pt-CdSe-Pt Nanodumbbells and Pt/GaN under Light Irradiation. *Nano Lett.* **2013**, *13*, 1352–1358.

(240) Saunders, A. E.; Popov, I.; Banin, U. Synthesis of Hybrid CdS-Au Colloidal Nanostructures. *J. Phys. Chem. B* **2006**, *110*, 25421–25429.

(241) Yu, P.; Wen, X.; Lee, Y. C.; Lee, W. C.; Kang, C. C.; Tang, J. Photoinduced Ultrafast Charge Separation in Plexcitonic CdSe/Au and CdSe/Pt Nanorods. *J. Phys. Chem. Lett.* **2013**, *4*, 3596–3601.

(242) Mokari, T.; Sztrum, C. G.; Salant, A.; Rabani, E.; Banin, U. Formation of Asymmetric One-Sided Metal-Tipped Semiconductor Nanocrystal Dots and Rods. *Nat. Mater.* **2005**, *4*, 855–863.

(243) Lee, J. S.; Shevchenko, E. V.; Talapin, D. V. Au-PbS Core-Shell Nanocrystals: Plasmonic Absorption Enhancement and Electrical Doping via Intra-Particle Charge Transfer. *J. Am. Chem. Soc.* **2008**, *130*, 9673–9675.

(244) Ellingson, R. J.; Beard, M. C.; Johnson, J. C.; Yu, P.; Micic, O. I.; Nozik, A. J.; Shabaev, A.; Efros, A. L. Highly Efficient Multiple Exciton Generation in Colloidal PbSe and PbS Quantum Dots. *Nano Lett.* **2005**, *5*, 865–871.

(245) Gesuele, F.; Sfeir, M. Y.; Koh, W. K.; Murray, C. B.; Heinz, T. F.; Wong, C. W. Ultrafast Supercontinuum Spectroscopy of Carrier Multiplication and Biexcitonic Effects in Excited States of PbS Quantum Dots. *Nano Lett.* **2012**, *12*, 2658–2664.

(246) El-Ballouli, A. O.; Alarousu, E.; Usman, A.; Pan, J.; Bakr, O. M.; Mohammed, O. F. Real-Time Observation of Ultrafast Intraband Relaxation and Exciton Multiplication in PbS Quantum Dots. *ACS Photonics* **2014**, *1*, 285–292.

(247) Okuhata, T.; Kobayashi, Y.; Nonoguchi, Y.; Kawai, T.; Tamai, N. Ultrafast Carrier Transfer and Hot Carrier Dynamics in PbS-Au Hybrid Nanostructures. *J. Phys. Chem. C* **2015**, *119*, 2113–2120.

(248) Moreels, I.; Lambert, K.; Smeets, D.; De Muynck, D.; Nollet, T.; Martins, J. C.; Vanhaecke, F.; Vantomme, A.; Delerue, C.; Allan, G.; et al. Size-Dependent Optical Properties of Colloidal PbS Quantum Dots. *ACS Nano* **2009**, *3*, 3023–3030.

(249) Debellis, D.; Gigli, G.; Ten Brinck, S.; Infante, I.; Giansante, C. Quantum-Confined and Enhanced Optical Absorption of Colloidal PbS Quantum Dots at Wavelengths with Expected Bulk Behavior. *Nano Lett.* **2017**, *17*, 1248–1254.

(250) Cademartiri, L.; Montanari, E.; Calestani, G.; Migliori, A.; Guagliardi, A.; Ozin, G. A. Size-Dependent Extinction Coefficients of PbS Quantum Dots. *J. Am. Chem. Soc.* **2006**, *128*, 10337–10346.

(251) Leatherdale, C. A.; Bawendi, M. G. Electron and Hole Relaxation Pathways in Semiconductor Quantum Dots. *Phys. Rev. B - Condens. Matter Mater. Phys.* **1999**, *60*, 13740–13749.

(252) Zhang, Y.; Wu, G.; Liu, F.; Ding, C.; Zou, Z.; Shen, Q. Photoexcited Carrier Dynamics in Colloidal Quantum Dot Solar Cells: Insights into Individual Quantum Dots, Quantum Dot Solid Films and Devices. *Chem. Soc. Rev.* 2020, pp 49–84.

(253) Nozik, A. J. Multiple Exciton Generation in Semiconductor Quantum Dots. *Chem. Phys. Lett.* **2008**, *457*, 3–11.

(254) Cozzoli, P. D.; Pellegrino, T.; Manna, L. Synthesis, Properties and Perspectives of Hybrid Nanocrystal Structures. *Chem. Soc. Rev.* **2006**, *35*, 1195–1208.

(255) Alvarado, S. R.; Guo, Y.; Ruberu, T. P. A.; Tavasoli, E.; Vela, J. Inorganic Chemistry Solutions to Semiconductor Nanocrystal Problems. *Coordination Chemistry Reviews*. 2014, pp 182–196.

(256) Buck, M. R.; Schaak, R. E. Emerging Strategies for the Total Synthesis of Inorganic Nanostructures. *Angewandte Chemie - International Edition*. 2013, pp 6154–6178.

(257) Ha, J. W.; Ruberu, T. P. A.; Han, R.; Dong, B.; Vela, J.; Fang, N. Super-Resolution Mapping of Photogenerated Electron and Hole Separation in Single Metal-Semiconductor Nanocatalysts. *J. Am. Chem. Soc.* **2014**, *136*, 1398–1408.

(258) Wu, K.; Rodríguez-Córdoba, W. E.; Yang, Y.; Lian, T. Plasmon-Induced Hot Electron Transfer from the Au Tip to CdS Rod in CdS-Au Nanoheterostructures. *Nano Lett.* **2013**, *13*, 5255–5263.

(259) Manna, G.; Bose, R.; Pradhan, N. Photocatalytic Au-Bi2S3 Heteronanostructures. *Angew. Chemie - Int. Ed.* **2014**, *53*, 6743–6746.

(260) Luo, X.; Xin, W.; Yang, C.; Yao, D.; Liu, Y.; Zhang, H.; Zhang, K.; Yang, B. Au-Edged CuZnSe2 Heterostructured Nanosheets with Enhanced Electrochemical Performance. *Small* **2015**, *11*, 3583–3590.

(261) Buck, M. R.; Bondi, J. F.; Schaak, R. E. A Total-Synthesis Framework for the Construction of High-Order Colloidal Hybrid Nanoparticles. *Nat. Chem.* **2012**, *4*, 37–44.

(262) Zhao, Q.; Ji, M.; Qian, H.; Dai, B.; Weng, L.; Gui, J.; Zhang, J.; Ouyang, M.; Zhu, H. Controlling Structural Symmetry of a Hybrid Nanostructure and Its Effect on Efficient Photocatalytic Hydrogen Evolution. *Adv. Mater.* **2014**, *26*, 1387–1392.

(263) Shin, B.; Gunawan, O.; Zhu, Y.; Bojarczuk, N. A.; Chey, S. J.; Guha, S. Thin Film Solar Cell with 8.4% Power Conversion Efficiency Using an Earth-Abundant Cu2ZnSnS4 Absorber. *Prog. Photovoltaics Res. Appl.* **2013**, *21*, 72–76.

(264) Repins, I.; Beall, C.; Vora, N.; Dehart, C.; Kuciauskas, D.; Dippo, P.; To, B.; Mann, J.; Hsu, W.

C.; Goodrich, A.; et al. Co-Evaporated Cu 2ZnSnSe 4 Films and Devices. *Sol. Energy Mater. Sol. Cells* **2012**, *101*, 154–159.

(265) Guo, Q.; Ford, G. M.; Yang, W. C.; Walker, B. C.; Stach, E. A.; Hillhouse, H. W.; Agrawal, R. Fabrication of 7.2% Efficient CZTSSe Solar Cells Using CZTS Nanocrystals. *J. Am. Chem. Soc.* **2010**, *132*, 17384–17386.

(266) Wang, W.; Winkler, M. T.; Gunawan, O.; Gokmen, T.; Todorov, T. K.; Zhu, Y.; Mitzi, D. B. Device Characteristics of CZTSSe Thin-Film Solar Cells with 12.6% Efficiency. *Adv. Energy Mater.* **2014**, *4*.

(267) Katagiri, H.; Saitoh, K.; Washio, T.; Shinohara, H.; Kurumadani, T.; Miyajima, S. Development of Thin Film Solar Cell Based on Cu2ZnSnS4 Thin Films. *Sol. Energy Mater. Sol. Cells* **2001**, *65*, 141–148.

(268) Katagiri, H. Cu2ZnSnS4 Thin Film Solar Cells. In *Thin Solid Films*; 2005; Vol. 480–481, pp 426–432.

(269) Yu, X.; Shavel, A.; An, X.; Luo, Z.; Ibáñez, M.; Cabot, A. Cu2ZnSnS4-Pt and Cu2ZnSnS4-Au Heterostructured Nanoparticles for Photocatalytic Water Splitting and Pollutant Degradation. *J. Am. Chem. Soc.* **2014**, *136*, 9236–9239.

(270) Kaur, K.; Kumar, N.; Kumar, M. Strategic Review of Interface Carrier Recombination in Earth Abundant Cu-Zn-Sn-S-Se Solar Cells: Current Challenges and Future Prospects. *Journal of Materials Chemistry A*. 2017, pp 3069–3090.

(271) Pundsack, T. J.; Chernomordik, B. D.; Béland, A. E.; Aydil, E. S.; Blank, D. A. Excited-State Dynamics in CZTS Nanocrystals. *J. Phys. Chem. Lett.* **2013**, *4*, 2711–2714.

(272) Kaur, A.; Goswami, T.; Babu, K. J.; Ghorai, N.; Kaur, G.; Shukla, A.; Rondiya, S. R.; Ghosh, H. N. Probing Ultrafast Charge Separation in CZTS/CdS Heterojunctions through Femtosecond Transient Absorption Spectroscopy. *J. Phys. Chem. C* **2020**, *124*, 19476–19483.

(273) Khare, A.; Wills, A. W.; Ammerman, L. M.; Norris, D. J.; Aydil, E. S. Size Control and Quantum Confinement in Cu2ZnSnS4 Nanocrystals. *Chem. Commun.* **2011**, *47*, 11721–11723.

(274) D'souza, F.; Ito, O. Photosensitized Electron Transfer Processes of Nanocarbons Applicable to Solar Cells. *Chem. Soc. Rev.* **2012**, *41*, 86–96.

(275) Whang, D. R.; Apaydin, D. H. Artificial Photosynthesis: Learning from Nature. *ChemPhotoChem*. 2018, pp 148–160.

(276) Grätzel, M. Dye-Sensitized Solar Cells. *Journal of Photochemistry and Photobiology C: Photochemistry Reviews*. 2003, pp 145–153.

(277) Li, G.; Sproviero, E. M.; McNamara, W. R.; Snoeberger, R. C.; Crabtree, R. H.; Brudvig, G. W.; Batista, V. S. Reversible Visible-Light Photooxidation of an Oxomanganese Water-Oxidation Catalyst Covalently Anchored to TiO2 Nanoparticles. *J. Phys. Chem. B* **2010**, *114*, 14214–14222.

(278) Wenger, B.; Grätzel, M.; Moser, J. E. Rationale for Kinetic Heterogeneity of Ultrafast Light-Induced Electron Transfer from Ru(II) Complex Sensitizers to Nanocrystalline TiO2. *J. Am. Chem. Soc.* **2005**, *127*, 12150–12151.

(279) Huss, A. S.; Bierbaum, A.; Chitta, R.; Ceckanowicz, D. J.; Mann, K. R.; Gladfelter, W. L.; Blank, D. A. Tuning Electron Transfer Rates via Systematic Shifts in the Acceptor State Density Using Size-Selected ZnO Colloids. *J. Am. Chem. Soc.* **2010**, *132*, 13963–13965.

(280) Bairu, S. G.; Mghanga, E.; Hasan, J.; Kola, S.; Rao, V. J.; Bhanuprakash, K.; Giribabu, L.; Wiederrecht, G. P.; Da Silva, R.; Rego, L. G. C.; et al. Ultrafast Interfacial Charge-Transfer Dynamics in a Donor-π-Acceptor Chromophore Sensitized TiO2 Nanocomposite. *J. Phys. Chem. C* **2013**, *117*, 4824–4835.

(281) Kc, C. B.; Lim, G. N.; Zandler, M. E.; D'Souza, F. Synthesis and Photoinduced Electron Transfer Studies of a Tri(Phenothiazine)-Subphthalocyanine-Fullerene Pentad. *Org. Lett.* **2013**, *15*, 4612–4615.

(282) Lim, G. N.; Maligaspe, E.; Zandler, M. E.; D'Souza, F. A Supramolecular Tetrad Featuring Covalently Linked Ferrocene-Zinc Porphyrin-BODIPY Coordinated to Fullerene: A Charge Stabilizing, Photosynthetic Antenna-Reaction Center Mimic. *Chem. - A Eur. J.* **2014**, *20*, 17089–17099.

(283) Kc, C. B.; Lim, G. N.; D'Souza, F. Multi-Modular, Tris(Triphenylamine) Zinc Porphyrin-Zinc Phthalocyanine-Fullerene Conjugate as a Broadband Capturing, Charge Stabilizing, Photosynthetic "antenna-Reaction Center" Mimic. *Nanoscale* **2015**, *7*, 6813–6826.

(284) Wijesinghe, C. A.; El-Khouly, M. E.; Zandler, M. E.; Fukuzumi, S.; D'Souza, F. A Charge-Stabilizing, Multimodular, Ferrocene-Bis(Triphenylamine)-Zinc- Porphyrin-Fullerene Polyad. *Chem. - A Eur. J.* **2013**, *19*, 9629–9638.

(285) Lee, S. H.; Larsen, A. G.; Ohkubo, K.; Cai, Z. L.; Reimers, J. R.; Fukuzumi, S.; Crossley, M. J. Long-Lived Long-Distance Photochemically Induced Spin-Polarized Charge Separation in β,B′-Pyrrolic Fused Ferrocene-Porphyrin-Fullerene Systems. *Chem. Sci.* **2012**, *3*, 257–269.

(286) Melomedov, J.; Ochsmann, J. R.; Meister, M.; Laquai, F.; Heinze, K. Tuning Reductive and Oxidative Photoinduced Electron Transfer in Amide-Linked Anthraquinone-Porphyrin-Ferrocene Architectures. *Eur. J. Inorg. Chem.* **2014**, No. 11, 1984–2001.

(287) Fukuzumi, S.; Ohkubo, K.; Suenobu, T. Long-Lived Charge Separation and Applications in Artificial Photosynthesis. *Acc. Chem. Res.* **2014**, *47*, 1455–1464.

(288) Poddutoori, P. K.; Lim, G. N.; Sandanayaka, A. S. D.; Karr, P. A.; Ito, O.; D'Souza, F.; Pilkington, M.; Van Der Est, A. Axially Assembled Photosynthetic Reaction Center Mimics Composed of Tetrathiafulvalene, Aluminum(Iii) Porphyrin and Fullerene Entities. *Nanoscale* **2015**, *7*, 12151–12165.

(289) Poddutoori, P. K.; Sandanayaka, A. S. D.; Zarrabi, N.; Hasobe, T.; Ito, O.; Van Der Est, A. Sequential Charge Separation in Two Axially Linked Phenothiazine- Aluminum(III) Porphyrin-Fullerene Triads. *J. Phys. Chem. A* **2011**, *115*, 709–717.

(290) Kamimura, T.; Ohkubo, K.; Kawashima, Y.; Ozako, S.; Sakaguchi, K. I.; Fukuzumi, S.; Tani, F. Long-Lived Photoinduced Charge Separation in Inclusion Complexes Composed of a Phenothiazine-Bridged Cyclic Porphyrin Dimer and Fullerenes. *J. Phys. Chem. C* **2015**, *119*, 25634–25650.

(291) Lu, Y.; Song, H.; Li, X.; Ågren, H.; Liu, Q.; Zhang, J.; Zhang, X.; Xie, Y. Multiply Wrapped Porphyrin Dyes with a Phenothiazine Donor: A High Efficiency of 11.7% Achieved through a

Synergetic Coadsorption and Cosensitization Approach. *ACS Appl. Mater. Interfaces* **2019**, *11*, 5046–5054.

(292) Ren, Z.; Nobuyasu, R. S.; Dias, F. B.; Monkman, A. P.; Yan, S.; Bryce, M. R. Pendant Homopolymer and Copolymers as Solution-Processable Thermally Activated Delayed Fluorescence Materials for Organic Light-Emitting Diodes. *Macromolecules* **2016**, *49*, 5452–5460.

(293) Iqbal, Z.; Wu, W. Q.; Huang, Z. S.; Wang, L.; Kuang, D. Bin; Meier, H.; Cao, D. Trilateral π-Conjugation Extensions of Phenothiazine-Based Dyes Enhance the Photovoltaic Performance of the Dye-Sensitized Solar Cells. *Dye. Pigment.* **2016**, *124*, 63–71.

(294) Kumar, S.; Singh, M.; Jou, J. H.; Ghosh, S. Trend Breaking Substitution Pattern of Phenothiazine with Acceptors as a Rational Design Platform for Blue Emitters. *J. Mater. Chem. C* **2016**, *4*, 6769–6777.

(295) Wang, L.; Wang, H. Y.; Fang, H. H.; Weng, H.; Yang, Z. Y.; Gao, B. R.; Chen, Q. D.; Han, W.; Sun, H. B. Universal Electron Injection Dynamics at Nanointerfaces in Dye-Sensitized Solar Cells. *Adv. Funct. Mater.* **2012**, *22*, 2783–2791.

(296) Ardo, S.; Sun, Y.; Staniszewski, A.; Castellano, F. N.; Meyer, G. J. Stark Effects after Excited-State Interfacial Electron Transfer at Sensitized TiO2 Nanocrystallites. *J. Am. Chem. Soc.* **2010**, *132*, 6696–6709.

(297) Sakaguchi, K. I.; Kamimura, T.; Uno, H.; Mori, S.; Ozako, S.; Nobukuni, H.; Ishida, M.; Tani, F. Phenothiazine-Bridged Cyclic Porphyrin Dimers as High-Affinity Hosts for Fullerenes and Linear Array of C60 in Self-Assembled Porphyrin Nanotube. *J. Org. Chem.* **2014**, *79*, 2980–2992.

(298) Gal, E.; Brem, B.; Pereţeanu, I.; Găină, L.; Lovasz, T.; Perde-Schrepler, M.; Silaghi-Dumitrescu, L.; Cristea, C.; Silaghi-Dumitrescu, L. Novel Meso-Phenothiazinylporphyrin Dyes: Synthesis, Optical, Electrochemical Properties and PDT Assay. *Dye. Pigment.* **2013**, *99*, 144–153.

(299) Qiu, X.; Lu, R.; Zhou, H.; Zhang, X.; Xu, T.; Liu, X.; Zhao, Y. Synthesis of Phenothiazine-Functionalized Porphyrins with High Fluorescent Quantum Yields. *Tetrahedron Lett.* **2008**, *49*, 7446–7449.

(300) Prakash, K.; Alsaleh, A. Z.; Neeraj; Rathi, P.; Sharma, A.; Sankar, M.; D'Souza, F. Synthesis, Spectral, Electrochemical and Photovoltaic Studies of A3B Porphyrinic Dyes Having Peripheral Donors. *ChemPhysChem* **2019**, *20*, 2627–2634.

(301) Duvva, N.; Eom, Y. K.; Reddy, G.; Schanze, K. S.; Giribabu, L. Bulky Phenanthroimidazole-Phenothiazine D-?-A Based Organic Sensitizers for Application in Efficient Dye-Sensitized Solar Cells. *ACS Appl. Energy Mater.* **2020**, *3*, 6758–6767.

(302) Krishna, N. V.; Krishna, J. V. S.; Singh, S. P.; Giribabu, L.; Han, L.; Bedja, I.; Gupta, R. K.; Islam, A. Donor-π-Acceptor Based Stable Porphyrin Sensitizers for Dye-Sensitized Solar Cells: Effect of π-Conjugated Spacers. *J. Phys. Chem. C* **2017**, *121*, 6464–6477.

(303) Lindsey, J. S.; Schreiman, I. C.; Hsu, H. C.; Kearney, P. C.; Marguerettaz, A. M. Revisited: Synthesis of Tetraphenylporphyrins. *J. Org. Chem.* **1987**, *52*, 827–836.